TEM CHARACTERISATION OF HEAVY-ION IRRADIATION DAMAGE IN Fe-Cr ALLOYS

SEN XU

WORCESTER COLLEGE

Thesis submitted for the degree of
Doctor of Philosophy

Michaelmas term 2009

Abstract:

Heavy-ion radiation damage in pure Fe and Fe-Cr binary alloys has been studied in this work using Transmission Electron Microscopy (TEM).

*Specimens were irradiated in bulk with 2 MeV Fe^{+} ions with irradiation temperatures ranging from 300-600^{o}C. Several irradiation doses were achieved at each temperature up to a maximum dose of 3x10^{19} ions m^{-2} (about 7 displacements per atom: **dpa**). A TEM specimen preparation technique has been developed to access the peak of the buried damage region. In most cases, the damage took the form of dislocation loops. The sizes of the loops were a function of both irradiation dose and temperature with maximum loop sizes up to about 100nm at 7 dpa.*

*Loops with Burgers vectors of type **b** = a<100> and **b** = a/2<111> were both observed in all specimens. In pure Fe, the proportion of the a<100> loops increased significantly at high temperatures (500^{o}C). This trend is not so clear in Fe-Cr alloys. Several loop nature determinations using inside-outside technique suggest that all the large loops are interstitial type. The vacancies are believed to exist either as small dislocation loops (<5nm) or sub-microscopic voids.*

Acknowledgements

First and foremost, I am heartily thankful to my supervisor Dr. Mike Jenkins for his supervision. This thesis would not have been possible without his encouragement, guidance and patience from the initial to the final. One simply could not wish for a better or friendlier supervisor.

I would like to sincerely thank Prof. Sergei Dudarev of Culham and Prof. Steve Roberts of Oxford University for their guidance at various stages in the work; and to thank Culham Centre of Fusion Energy (UKAEA) for funding this research.

I would like to show my gratitude to all past and present member of the group, especially to Drs: Zhongwen Yao, Vanessa de Castro, Armando Giannattasio and Sergio Lozano-Perez for their great mentorship in the lab and at the microscopes. Some of Zhongwen's in-situ thin-foil results were used in this thesis to complement the discussion section of this thesis and served as a useful comparison to the bulk experiments. The EELS results presented in this thesis were acquired and processed by Vanessa de Castro.

Special thanks to all the others who have provided assistance to make this work possible. I am particularly grateful to:

Dr. Nianhua Peng from Surrey Ion Beam Centre for all his help on the irradiation.

Dr. Mark Kirk and Dr. Bernie Kestel from Argonne National Laboratory for their help with notoriously difficult specimen preparations.

Prof. John Titchmarsh for his guidance during teaching sessions.

Steve Lett, Bob Lloyd, Richard Cripps, Ron Doole, Clive Downing, Laurie Walton and Pete for their help and assistant in the experiments.

And to all my friends and family who accompanied me during my study.

Finally, I would like to thank my parents for making this possible. **谢谢爸爸妈妈！**

Sen Xu

Worcester College, Oxford

List of Publications:

‘TEM characterisation of heavy-ion irradiation damage in Fe-Cr alloys’ S. Xu, Z. Yao & M. L. Jenkins, Journal of Nuclear Materials, Volume 386-388, 2009, page 161-164.

‘Preparation of TEM samples of Ferritic alloys’ Z. Yao, S. Xu, M. A. Kirk & M. L. Jenkins, Journal of Electron Microscopy, Volume 57, Number 3, 2008, Pages 91-94.

‘In situ transmission electron microscopy and ion irradiation of ferritic materials’ M. A. Kirk, P. M. Baldo, A. C. Y. Liu, E. A. Ryan, and R. C. Birtcher, Z. Yao, S. Xu, M. Jenkins, D. Kaoumi, A. Motta, Microscopy and Research Techniques, Volume 72 Issue 3, 2009, page 182 -186.

Table of content

Introduction:

We live in an age where global demand for energy grows rapidly day by day, where hydrocarbon supplies diminish, and the use of fossil fuels poses serious environmental concerns. The need to find new energy sources is becoming increasingly important for mankind. This thesis is part of a large international collaboration, making efforts to develop a new energy source using nuclear fusion.

Nuclear fusion is the process that powers the Sun. Plasma physics research has achieved controlled deuterium-tritium reactions using magnetic confinement and a commercial fusion power plant has been proven feasible. A number of fusion power plant designs have been put forward, for example, the international community proposes to construct ITER at Cadarache in France, a deuterium-tritium experimental fusion reactor based on the successful JET project carried out at Culham[1].

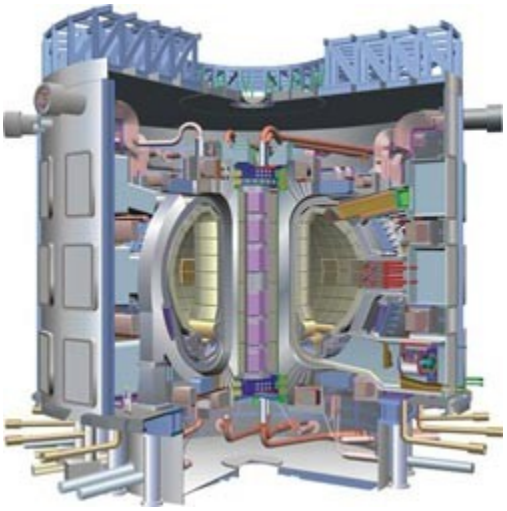

Fig.0 The ITER device based on the tokamak concept [2]

Fusion energy has many advantages: it is efficient, renewable and the absence of fissile materials eliminates the possibility of serious accidents and problems of long-term waste disposal. Fusion also has the major advantage of being environmentally friendly, as it produces no CO_2 or SO_2. Despite all its advantages, structural materials for the first wall or blanket component of future commercial reactors will have to be carefully chosen, since the materials will be operating in conditions of high-flux irradiation with fast-neutrons (with energies up to 14MeV), temperatures up to 600^{o}C and high stresses up to 300MPa [2, 3]

One of the major environmental problems induced by high-energy neutron irradiation is the activation of the materials, i.e. unstable isotopes are produced, which decay over long periods of time and cause the material to be radioactive. Therefore, it is preferable to use ‘reduced-activation’ materials, the elemental constitution of which are carefully chosen to eliminate the possibility of producing long-life radioactive components. With ‘reduced-activation’ materials, radioactivity should reduce to safe levels within 100 years [4].

High energy neutron irradiation can also cause damage in materials by producing helium and hydrogen via transmutation and by displacing atoms from their lattice site and producing ‘displacement damage’. As a consequence the mechanical properties of the material may be severely degraded by effects such as void swelling and embrittlement [5]. It is doubtful if any existing material can withstand the conditions in a fusion reactor

economically. It is necessary, therefore, to develop new structural materials if commercial fusion reactors are to be realised [6].

Ferritic-martensitic steels such as Eurofer 97 are the furthest in development of the three major classes of candidate structural materials for fusion applications [7]. Such steels, which are based on Fe-9Cr with alloying additions of W, V and Ta (all low-activation elements), have the advantages of low activation, good swelling resistance and adequate mechanical properties [8, 9]. Model Fe-Cr alloys, as the basis of these steels, are now the subject of several multi-scale modelling programs in the UK, Europe and the United States. It is known that alloys of containing 9% Cr have the lowest increase in DBTT under irradiation, and the Cr content in Fe-Cr alloys is known to have a pronounced effect in void-swelling[7, 10, 11].

In the present fusion project at Oxford, it is intended to combine modelling and experimental approaches to give a better fundamental understanding of the deformation behaviour of bcc metals including vanadium, tungsten, iron, and Fe-Cr binaries up to 12% Cr and of the steels themselves. The modelling project will combine *ab initio* modelling, development of novel inter-atomic potentials, molecular dynamics, kinetic Monte-Carlo methods and dislocation dynamics. The experiments will yield data on the structure and properties of nano-scale defects generated in materials in damage cascades, plastic flow and fracture behaviour of the materials. Experimental data will test the predictions made by advanced computer models.

This thesis focused on the evolution of microstructure damage in bulk iron and Fe-Cr binary alloys. Specimens were irradiated with Fe^{+} ions to simulate the knock-on effect of neutron irradiation. The irradiations were carried out in the University of Surrey Ion Beam Facility, with incident ion energy up to 2MeV and doses up to $3x10^{19}$ ions m^{-2} (~7dpa).

Chapter 1: Literature Review

1.1 Radiation damage effects

The fusion reaction produces fast neutrons of energy up to 14MeV. Structural materials for the first wall or blanket component in the reactor will be exposed to such energetic neutrons irradiation to doses as high as 100dpa. Materials under such irradiation will suffer deleterious effects that will seriously degrade their mechanical properties[5].

The five major radiation damage effects which degrade mechanical properties are[12]:

1. Low temperature radiation hardening and embrittlement, which occur mostly at doses above 0.1dpa and temperatures up to $0.35T_M$, where T_M is the melting temperature;

2. Phase instabilities caused by radiation induced segregation and precipitation, at damage levels above 10dpa at temperatures between 0.3 to $0.6T_M$;

3. Irradiation creep, which occurs for doses > 10dpa at about 0.45 T_M, and can permanently deform the material;

4. Volumetric void-swelling which causes dimensional instability for doses >10dpa at temperatures from 0.3 to 0.6T_M;

5. High temperature He embrittlement of grain boundaries, which happens particularly for doses >10dpa and temperatures > 0.5T_M.

Fusion reactors will only be operated safely and economically if the materials used in the reactor are able to withstand or avoid such effects and have reasonable service lifetime.

1.2. Candidate structural materials for fusion reactors

There are many factors which must be taken into account in determining and developing materials for fusion structure applications. First, the material needs to have the mechanical, chemical and physical properties which ensure that basic safety concerns are met. In addition, it is preferable to use low-activation (reduced-activation) materials for structure components, so that in such materials, radioactivity would reduce to safe levels within 100 years. The safety and environmental advantages of low-activation materials have been discussed by Cook and Bloom[4, 13].

In 1991, Piet et al. [14] evaluated all elements in the periodic table with respect to their safety, waste disposal and recycling potential as structural material in fusion reactors. The ferritic/martensitic steels and vanadium alloys

were identified as potential low-activation fusion structural alloys, and graphite and silicon carbide as possible low activation structural ceramics.

Over the last decade, candidate materials have been restricted to 8-9%Cr ferritic/martensitic steels, V-Cr-Ti alloys and silicon carbide composites [4, 6, 7, 15-17]. We now discuss each of these classes of materials briefly.

1.2.1 SiC composites

Silicon carbide composites (SiC fiber-reinforced SiC matrix composites such as Nicalon^{TM}) are of interest in fusion applications not only due to their low activation properties, but also due to their good mechanical strength at very high temperature (up to 1000^{o}C). Research on the strength, thermal conductivity and dimensional stability under irradiation of SiC composites has been carried out for the last few decades. Although new generations of composites have higher strength in the unirradiated condition and smaller reduction in strength under irradiation, some fundamental questions still need to be addressed.

Swelling in monolithic SiC has been studied by Snead, et al.[18]. It is known that point defect swelling occur in SiC at low temperature, which saturates at relatively low damage levels. The total amount of point-defect swelling decreases with increasing temperature. At higher temperature (typically above 1000^{o}C), void swelling occurs. Such swelling increases with damage level and

is not likely to saturate (refer to **Fig.1.2.1**). Because irradiation damage causes volumetric swelling and reduction in strength in monolithic SiC, the strength of the composite structure will be largely reduced by radiation damage. It was found by Hasegawa et al. using He implantation, that the strength of a SiC composite decreases dramatically in the presence of He [19]. The other critical issue need to be solved is the relatively low thermal conductivity of SiC composites which will be further reduced by irradiation [4, 6].

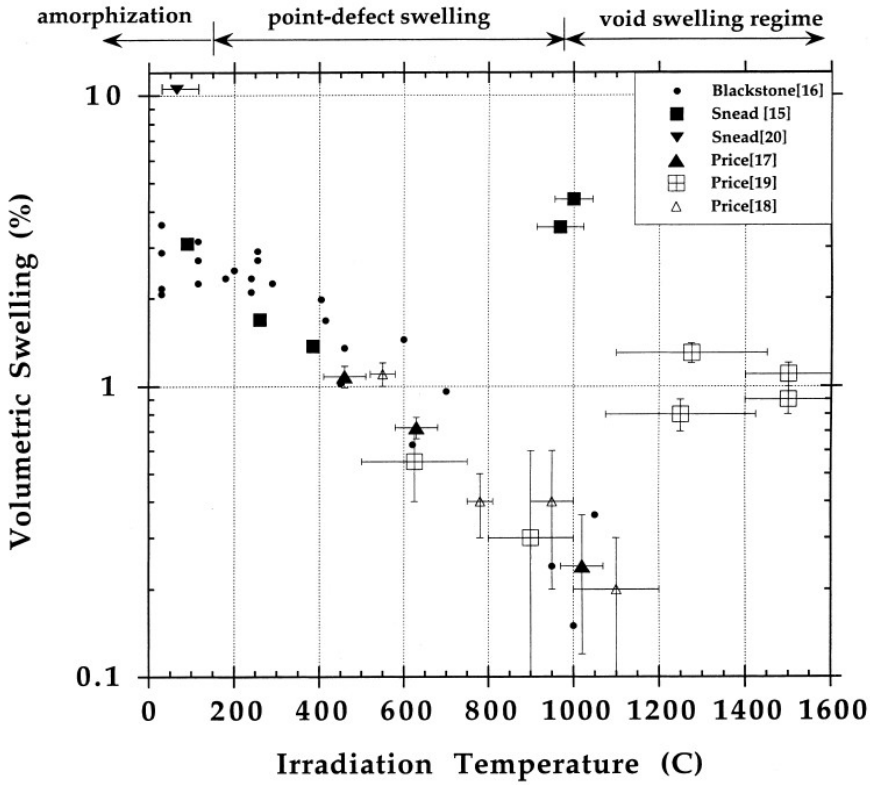

Fig.1.2.1 Void Swelling in SiC. [19]

1.2.2 Vanadium alloys

Vanadium alloys have the advantages of relatively high thermal conductivity and low thermal expansion. As a result, they possess a high heat flux capability which makes them attractive candidates for fusion reactor blanket structural applications. Work has been done to understand and develop vanadium alloys which have acceptable radiation damage resistance. It was found that irradiation causes a significant upward shift in the ductile to brittle transition temperature (DBTT) under irradiation at temperatures higher than 450^{o}C. For example, under irradiation to 4dpa, V-4Cr-4Ti alloy became unreliable at below 400^{o}C due to an increase in the DBTT, which causes significant hardening and possible fracture. Helium embrittlement is also a major concern for vanadium alloys exposed to irradiation. Under fast neutron bombardment, α-particles are produced inside the alloys which will nucleate and grow to helium bubbles at grain boundaries; as a result, the tensile ductility is lost. Apart from helium embrittlement, interstitial elements present in vanadium alloys such as oxygen, carbon, and nitrogen can also cause loss of ductility. Depending on the amount and distribution of these interstitial elements, cleavage and/or grain boundary fracture could occur. Therefore reducing the number of interstitial elements in vanadium alloys could improve their mechanical properties [4, 6].

1.2.3 Ferritic/Martensitic steels

Ferritic/Martensitic (F/M) steels (BCC low carbon steels such as Eurofer 97, F82H) are the most developed within the three classes of candidate material for fusion applications. This class of steels which are based on Fe-Cr have the advantages of low activation, good swelling resistance and adequate mechanical properties. It has been found that F/M steels generally exhibit very low swelling over the entire temperature range [10, 20][1]. At temperatures range below 400^{o}C, irradiation causes hardening which saturates at about 10dpa. Softening can occur at irradiation temperatures of 500^{o}C and above.

In the early stage of development, research explored alloys having Cr in the range 2-12%, using W as a replacement for Mo; V and/or Ta was used as the carbide forming elements and Fe-Cr alloys with V as the sole strengthening element [21]. From the initial research results, the focus of attention was narrowed to alloys containing 8-9%Cr, 1-2% W; where V and Ta act as carbide forming elements. Rieth et al. [22, 23] tested several steels under neutron irradiation at low temperature (250-400^{o}C), to study the effect of irradiation hardening (**Fig.1.2.3**). All low activation steels examined exhibited lower DBTT than Cr-Mo steels. F82H and ORNL (9Cr-2W-VTa) performed best in the respect of low temperature hardening.

[1] Void swelling in ferritic materials is described more fully in section 1.4.4.

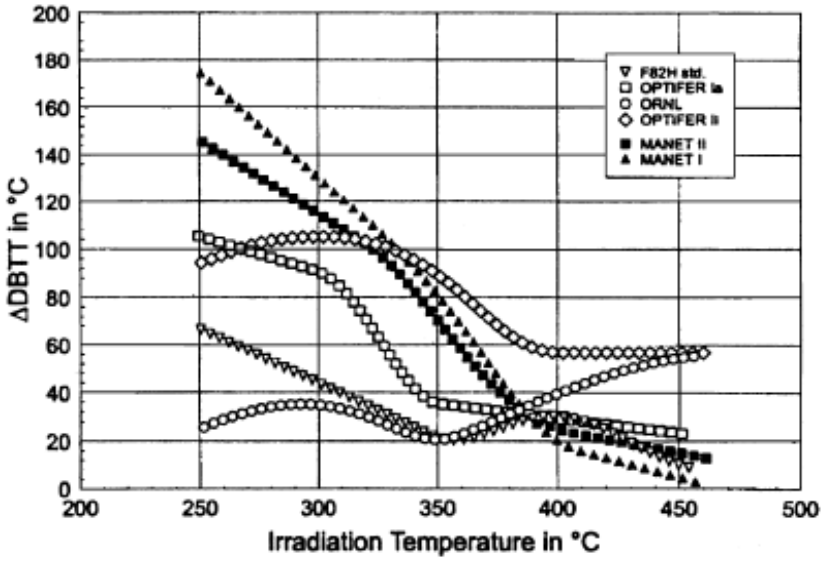

Fig.1.2.3.1 Irradiation induced shift in the DBTT as function of irradiation temperatures for different steels [4].

The understanding of the effect of irradiation on fracture properties (particularly at low temperature) and the effect of helium transmutation on the deformation and fracture of irradiated materials are major unresolved issues for F/M steels [6, 24-27].

In particular, the effect of the alloy composition (especially the Cr content) is presently not well understood. Kohyama et al. [7] carried out experiments to explore the shift of the DBTT in F/M steels under fission neutron irradiation (ΔDBTT). These results are shown in **Fig.1.2.3.2**. It is seen that there is a clear minimum in the ΔDBTT at about 9%Cr. In fact, both the DBTT and ΔDBTT are lowest for alloys containing about 9%Cr [7, 10, 11]. However these effects are not understood on a mechanistic level. Without such an understanding, it is difficult to design alloys with optimum behaviour [6].

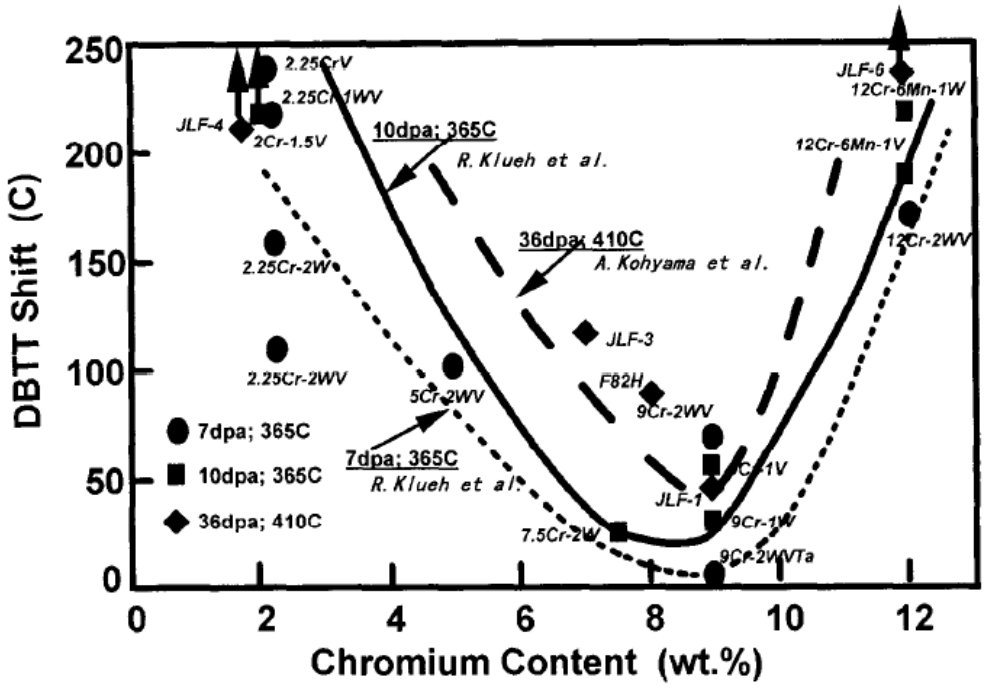

Fig.1.2.3.2. Effect of Cr content on DBTT shift of LAFs by neutron irradiation in FFTF [7].

Although F/M steels containing 9%Cr have less of a problem with low temperature hardening than V alloys due to their relatively low DBTT, the use of such steel in fusion reactors at temperatures below 400°C is still unreliable [28]. In addition candidate Cr-W F/M steels have a limited upper operating temperature from 550 to 600°C due to their low thermal creep strength. Therefore, the possible operating temperatures for current F/M steels is limited to 400-600°C. One approach to improve this is to use oxide dispersion strengthened (ODS) steels, which were first invented in the 1980s [29-32]. Based on the ferritic/martensitic steels, ODS ferritic/martensitic steels are produced by mechanical alloying of rapidly solidified alloy and ultra-fine oxide powders, followed by consolidation by hot extrusion, rolling or hot isostatic pressing [28]. ODS F/M steels have good thermal conductivity, and their

properties of good swelling resistance and low radiation damage accumulation are further enhanced from the base F/M steels [33]. They have higher temperature strength due to the presence of Y_2O_3 or TiO_2 particles dispersed in the ferrite matrix [28].

Research on ODS steels is rapidly growing, but relatively little is known on the irradiation response of this class of steels. Yamashita et al. claimed that ODS F/M steels are stable under irradiation to a rather high dose (200dpa) [34], although coarsening of oxide particles was observed [35]. Schaublin et al. recently observed very similar irradiation induced defects (dislocation loops, nanocavities) in ODS F/M steels to those seen in F/M steels [33]. In general, ODS F/M steels have several enhanced properties compared with candidate F/M steel, and more study of their irradiation response is being carried out [36].

1.3. Approaches to develop a mechanistic understanding of radiation damage in ferritic materials

This thesis is mainly concerned with the development of a mechanistic understanding of the radiation response of F/M steels. For this reason the discussion from now on will be restricted mainly to ferritic materials, i.e. α-iron, Fe-Cr model alloys and the steels themselves.

As discussed in chapter 1.2.3, the Cr content has a pronounced effect on the irradiation response of F/M steels. In order to gain a better understanding of the effect of the Cr content, one needs to gain a better understanding of the behaviour of model Fe-Cr alloys, which form the basis of ferritic/martensitic steels. The development of irradiation damage in Fe-Cr alloys has not been studied very extensively and it is now the subject of several integrated multi-scale modelling and experimental programs in the UK, Europe and the United States [6, 12, 13]. For example, in addition to the Oxford project, Matijasevic et al. from SCK.CEN (Belgium) has been working on neutron irradiated Fe-Cr and Hernandez-Mayoral et al. from CIEMAT (Spain) has been working on thin-foil irradiation of Fe and Fe-Cr. Comparison between these works has been made in the discussion chapter.

The Fe-Cr phase diagram shown in **Fig.1.3** illustrates the phase of Fe-Cr alloys as a function of temperature. However, this standard diagram is not adequate in the low-temperature low-Cr concentration region. Both experiments [37, 38] and modelling [39] have shown that for a Cr content less

than about 7%, short-range ordering occurs. For Cr contents greater than about 12%, a Cr-rich α’ phase occurs.

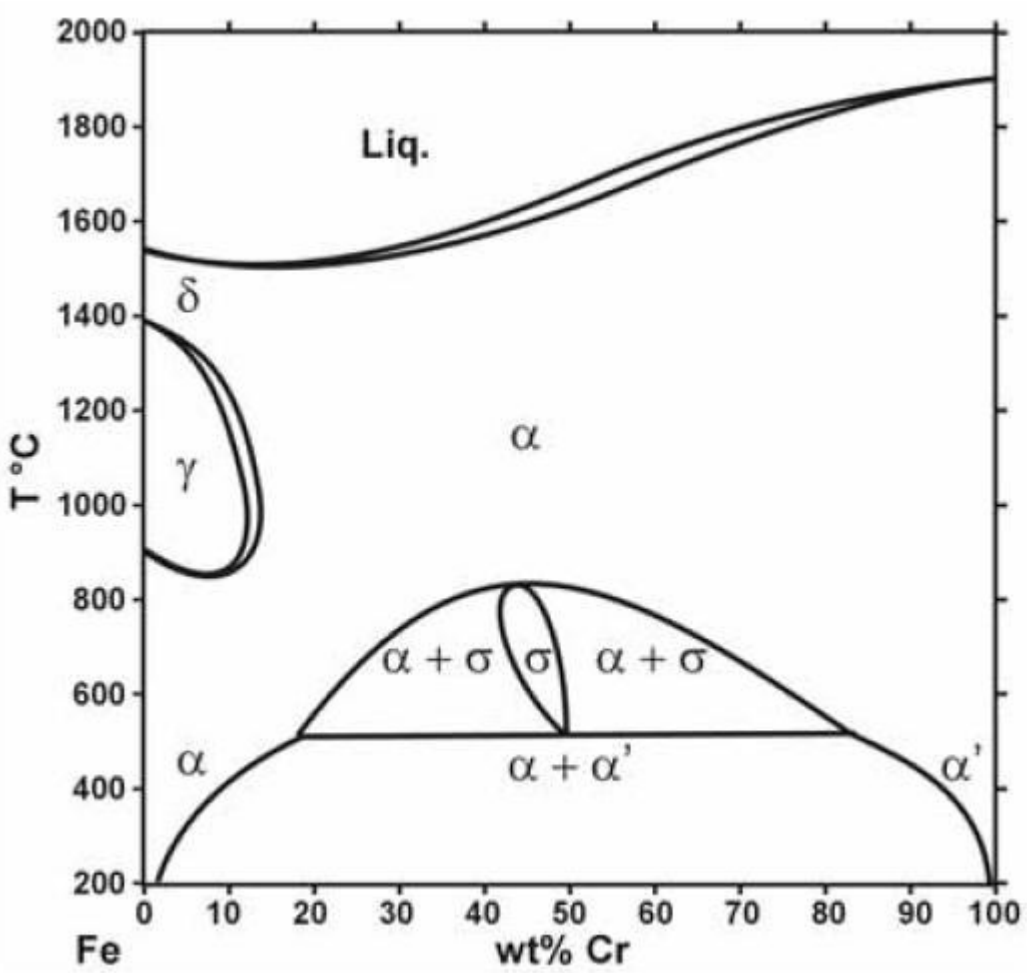

Fig.1.3 Phase diagram of Fe-Cr [40].

1.3.1 Experimental approach

No currently-available irradiation facility is adequate in reproducing the conditions which will prevail in a future fusion reactor. It is planned to construct an accelerator-based source of high-energy neutrons (the International Fusion Materials Irradiation Facility, IFMIF) in parallel with the proposed international experimental fusion reactor ITER [13]. However, this facility will not be available for at least a decade, and even when available its experimental volume will be very limited. For the near future fusion reactor damage will have to be simulated by other means [13].

Experiments on damage development of materials usually use fission neurons, protons and heavy-ions to simulate the effect of fusion neutrons. Microstructural evolution upon irradiation can be studied by several experimental methods such as Transmission Electron Microscopy (TEM) [41], Atom Probe Field Ion Microscopy (APFIM) [42, 43], Small Angle Neutron Scattering (SANS) [44, 45] and Positron Annihilation Spectroscopy (PAS) [46-49]. The current project focuses on TEM study of irradiation damage. Heavy-ion irradiation is commonly used to study the displacement damage because it has the advantage that it allows precise control of irradiation conditions such as dose, flux and temperatures. In addition, unlike fast-neutrons, ion irradiations do not cause activation and transmutation effects, which ease specimen handling issues in experiments. However, the disadvantage is that the ion range is much smaller than the range of fast neutrons so that bulk effects may not be simulated realistically [50].

1.3.2 Modelling approach

In parallel with the experimental work is computational modelling. The development of modelling has been one of the major differences in modern research on radiation damage. Multi-scale modelling programmes aim to give a better understanding of fundamental aspects of radiation damage, and to obtain information that not directly accessible from experiments. Studying radiation damage phenomena requires modelling for time scales from femtoseconds to years and length scales from sub-nanometer to meters. At the moment, multi-scale modelling is focusing on topics such as the production and migration mechanisms of point defects, plastic deformation mechanisms and fracture mechanics behaviour. Multi-scale modelling includes five major stages [1, 12]:

1. Ab-initio modelling which use quantum mechanics to develop inter-atomic potentials;

2. With the aid of the potential function, molecular dynamics modelling (MD) considers elastic collisions between atoms (and incident particle) and studies the primary displacement damage and cascade formation at a rather short time scale (~ps);

3. Kinetic Monte Carlo (KMC) simulation uses statistical mechanics to study cascade evolution at a larger time scale than MD;

4. Dislocation Dynamics simulation is used to model flow and fracture behaviour;

5. The finite element method predicts the properties of large structures.

The present fusion project at Oxford intended to combine modelling and experimental approaches to give a better fundamental understanding of the deformation behaviour of bcc metals including vanadium, tungsten, iron, and Fe-Cr binaries up to 12% Cr and of the steels themselves. The modelling project combined ab-initio modelling, development of novel inter-atomic potentials, molecular dynamics, kinetic Monte-Carlo methods and dislocation dynamics. The experiments provided data on the structure and properties of nano-scale defects generated in materials in damage cascades, plastic flow and fracture behaviour of the materials. My project focused on the evolution of microstructure damage in bulk Fe-Cr alloys, and previous relevant work is reviewed in the next section.

1.4. Radiation damage development in ferritic materials

In this section we review what is known about damage development in α-Fe, Fe-Cr alloys and steels, with an emphasis on fundamental damage mechanisms and TEM studies.

1.4.1 Cascade collapse in ferritic materials

1.4.1.1 Cascade collapse α-iron

Low-dose heavy-ion irradiation experiments have been carried out to simulate neutron displacement damage. In these experiments heavy-ions (often self-ions) are used to simulate the primary knock-on atoms (PKAs) caused by fast-neutrons. The primary knock-on atom (PKA) is defined as the first atom in the solid that gets struck by an incident particle. In the fusion neutron case the average PKA energy is typically several tens of keV. When the energy transferred to the knock-on atom is much greater than a few keV, the knock-on atom itself is able to displace many atoms, which may in turn go on to produce further displacements; this sequence of events is refer to as 'displacement cascade'. Thin foils are irradiated with heavy ions typically of energy up to about 100keV and are then viewed in the TEM. At low doses (< 10^{16} ions m^{-2}) cascades are well separated, and the experiments give direct information on defect formation within individual cascades [51-53].

In such experiments, it has been shown that in many materials vacancy loops are produced directly in cascades by a process of 'cascade collapse'. For

example, Jenkins, Wilkens and Katerbau [54] showed directly that vacancy loops are produced at cascade sites in Cu_3Au initiated by Cu^+ ions with energy ≥ 10keV. The same seems to be true in most fcc, bcc and hcp metals [41, 54-56].

However, iron is an exception to this general behaviour. Low-dose thin-foil experiments were carried out on α-iron by Jenkins et al. in 1978 [57]. It was observed that vacancy loops were not produced within individual cascades generated by self-ions. No visible damage was seen in α-Fe under self-ion irradiation at RT with energies 40-240keV at doses lower than $5x10^{16}$ ions m^{-2}. Vacancy loops were produced in individual cascades produced by very heavy or molecular ions. The defect yields were found to have a high dependence on ion mass. Both a/2<111> and a<100> loops were found in approximately equal numbers.

The development of irradiation damage in α-iron was further studied in the 1980s with the aid of in-situ TEM irradiation experiments. Such experiments were achieved on the Argonne IVEM-Tandem where a beam-line is fed directly into the microscope. With such a facility, a thin foil specimen can be viewed with TEM whilst under heavy-ion irradiation and the production and development of damage can be observed at different dose levels and at different temperatures. The production of loops by self-ion irradiation in pure Fe (and in ferritic steels in general) was observed only at overlap doses (>10^{18} ions m^{-2}) at RT and at 30K [58, 59]; the defect yield in Fe was much lower than in Cu and Ni (**Fig.1.4.1.1**). This observation confirms that individual self-

ion cascades do not collapse in iron. It was inferred that invisible vacancy clusters are produced at cascade sites, which only aggregate to form a visible loop under cascade overlap (a second cascade produced at the same site). Most dislocation loops found in experiments of this kind were determined to be of vacancy nature. The explanation to this is that interstitials created during cascade formation in the thin-foils (typically less than 50nm) are lost to the surface or form small clusters invisible in TEM [55].

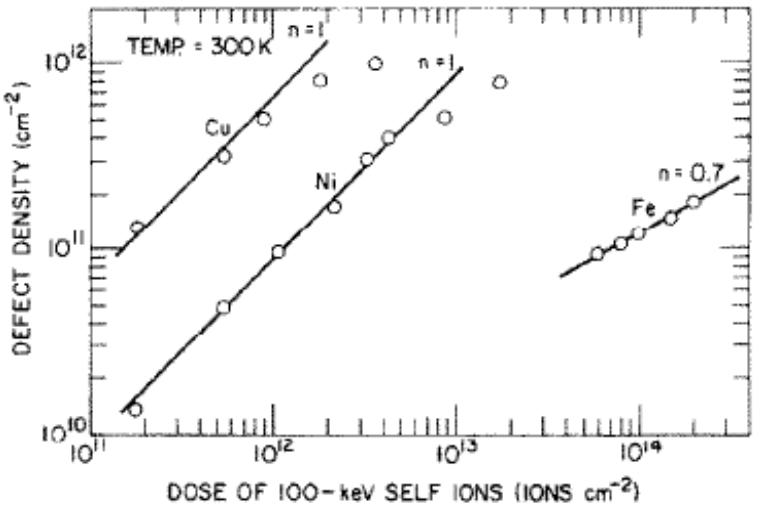

Fig.1.4.1.1 Dislocation loop density against dose of self-ion irradiation [58].

Recent work by Z. Yao et al. [60] with in-situ ion irradiation at RT and 300°C has confirmed that visible loop only started to appear at overlap doses of about 2×10^{16} ions m^{-2}. This work will be described in Chapter 6.

1.4.1.2 Cascade collapse in Fe-Cr alloys and ferritic/martensitic steels

Cascade collapse in Fe-Cr and F/M steels has not been studied extensively prior to the present Oxford project. However, Fukushima et al. have observed small defects produced by cascade damage in Fe-9Cr ferritic steel and Japanese Ferrite Martensitic Steel (JFMS) after heavy-ion irradiation [61]. Thin foils of both steels were irradiated with 40KeV Cu^{+} and Fe^{+} ions to doses of $8 \times 10^{16} – 8 \times 10^{17}$ ions m^{-2} at room temperature. Defects in the form of small (1-3nm) white dots in weak-beam images, believed to be dislocation loops, were observed. Low defect yields of <0.01 were observed in both materials, suggesting that cascade overlap was necessary for collapse to occur. The nature of the loops where determined to be 90% vacancy and 10% interstitial using the now discredited 2½-D technique [62]. The Burgers vectors of these loops were not determined. The temperature dependence of the defect yield was studied and it was found that the yield decreased gradually at temperatures ≥200^{o}C, which is probably due to the onset of vacancy migration, leading to increased recombination.

Recent in-situ experiments by Yao et al. [60, 63] have revealed that damage development in Fe-Cr alloys is similar to pure Fe, in that loops are seen only at overlap doses [60]. However the threshold dose for visible damage was lower in Fe-Cr alloys (i.e. Fe-5Cr, Fe-8Cr, and Fe-11Cr). It was also observed that both loop loss and loop “hopping” motion were reduced in Fe-Cr alloys

compared to pure Fe. This suggests that Cr has the effect of reducing loop mobilities by pinning. This work will be discussed in more detail in Chapter 6.

1.4.2 Damage evolution in ferritic materials under irradiation

1.4.2.1 Damage evolution in α-iron

Cluster damage in irradiated iron was first observed in the 1960s. Experiments by Masters revealed the presence of large (up to 150nm) rectangular interstitial loops after high-dose (10^{20} m^{-2}) 150keV self-ion irradiation. The loops were all believed to have **b** = a<100> character. It was thought that **b**= a/2<111> loops would glide out to the surface during irradiation and thus would not be observed [64]. In contrast, experiments by Eyre and Bartlett [65, 66] showed evidence of **b**= a/2<111> interstitial loops in iron after neutron irradiation. Interstitial loops with **b** = a<100> were also found after 1MeV electron irradiation [64].

Robertson et al. [67] studied micro-structural damage in α-iron of different purities by low-dose fission-neutron irradiation (E > 1MeV) at PLUTO/Harwell in the1980s. These authors showed that no visible damage was observed in all α-irons up to a dose of 4 x 10^{23} neutrons m^{-2} at 353K. At doses above 4 x 10^{23} neutrons m^{-2}, small loops were mainly confined to isolated and grain boundary dislocation lines; visible dislocation loops in the matrix were only observed at highest dose. This observation is consistent with experiments on heavy-ion irradiation described in chapter 5.1, in which cascades produced by Fe ions did not collapse spontaneously to vacancy loops at low doses. However, it was surprising that interstitial loops, which were believed to be

lost to the surface in thin foil experiments, were also not observed in these bulk specimens.

Robertson et al [67] found very small defects in a relatively impure iron irradiated at 80^{o}C to a dose of 3.4 x 10^{23} neutrons m^{-2}. A homogeneous damage structure was found under a further increase in dose to 7.5 x 10^{23} neutrons m^{-2}. These damage structures consisted of populations of small loops of size less 10nm and larger loops of size up to 40nm. It was found that most smaller loops had Burgers vector **b**= a/2<111> whilst most of larger loops had **b** = a<100>. Some of the larger loops were analysed by the inside-outside technique to be interstitial in nature. Small loops with **b**= a/2<111> and a<100> were also identified in nearly-pure iron after fast neutron irradiation to low doses of 0.06dpa at 280^{o}C. The authors reported indirect evidence suggesting these loops were also interstitial in nature [68].

Micro-structural evolution in neutron-irradiated iron as a function of irradiation temperature from 473 to 673K has been studied by Horiki et al. [69]. Pure iron specimens were irradiated at the Japanese Material Test Reactor (JMTR) with neutrons of energy > 1MeV to a dose ~1.0 x 10^{24} neutrons m^{-2}. In the temperature range 473-573K, very small defect clusters were observed, with most defects located near dislocation lines. At a temperature of 623K, dislocation loops developed; voids were observed only at this temperature. At a higher temperature of 673K, the dislocation loops changed to irregular shapes. Subsequent electron irradiation was carried out to determine the nature of the loops [69]. Loops produced at 473K were determined to be

interstitial. In ‘T-cycle’ irradiations of 473/673K (i.e. where the temperature was cyclically changed between 473K and 673K during irradiation), the number density of interstitial loops was much lower than in an irradiation carried out at 673K alone. This strongly suggested that a large number of invisible vacancy type cluster accumulated at low temperature (473K), which evaporated at high temperature and suppressed the formation of interstitial clusters.

Hernandez-Mayoral et al. recently studied the evolution of radiation damage in pure iron irradiated in the Belgium Reactor BR2 (Mol, Belgium) to study the flux and dose effects [63]. It was found by TEM analysis that both the defect densities and sizes increased with dose. It was also found that at the same dose level (dpa), irradiation with higher flux generated a higher defect density.

Yao et al. [60], Jenkins et al. [70] and Hernandez-Mayoral et al. [63] carried out a series of thin-foil experiments on UHP Fe and Fe-Cr alloys from 300^{o}C to 500^{o}C in parallel to the work of this thesis. These experiments will be described briefly in this chapter, and a more detailed discussion will be postponed to Chapter 6 where comparison to the bulk experiments will be made.

Yao et al. [60] found that at 300^{o}C, strings of small interstitial loops were first formed in the thicker regions of the foil. As the irradiation progressed, the strings coalesced into larger and elongated ‘finger-shaped’ loops formed. Contrast experiment showed that the majority of the resolvable loops had

Burgers vector a/2<111>. At 400^{o}C [71], the damage structure was somewhat similar to the case of 300^{o}C. A mixture of a/2<111> and a<100> loops were found. At 500^{o}C [70] [71], the damage structure changed significantly from lower temperatures. It consists of predominately a<100> prismatic edge loops of size several hundred nanometres and formed regular arrays.

The unexpected transition in damage microstructure from 400-500^{o}C was explained by parallel theoretical calculations carried out by Dudarev et al. [72, 73] on the anisotropic elastic self-energies of dislocation loops (refer to chapter 1.4.3 and Chapter 6).

In summary, both interstitial and vacancy loops were found in irradiated iron by varies people. These loops have a mixture of ½<111> and <100> Burgers vectors. However a consistent picture of radiation damage evolution has not been established for Fe.

1.4.2.2 Fe-Cr alloys

Gelles et al. have studied Fe-Cr specimens irradiated at temperatures from 400-450°C to doses ~10^{26} n m^{-2}. In these experiments, the fraction of a/2<111> loops increased with increasing Cr content. This observation was used to explain the change in swelling of different Cr content in Fe-Cr alloys. It was thought that a<100> dislocations in ferritic materials are sessile (unable to move conservatively); therefore Fe 3% Cr has the least void-swelling due to the large fraction of a<100> loops. A peak swelling of 0.7% was found in a specimen of Fe-9%Cr irradiated at 425°C [10, 20][2].

Parollo et al. also worked on the irradiation response of Fe-Cr alloys (0, 2, 6, 12 and 18 at. % Cr). Neutron irradiation was carried out at 400°C in the BR-10 fast reactor to doses in the range 5.5-7.1dpa. It was observed that dislocation loops with **b** = a<100> were predominant in irradiated Fe, Fe-2Cr and Fe-6Cr. In Fe-Cr alloys containing more than 6% Cr, both a<100> and a/2<111> loops were found. The loops were believed to be interstitial in nature [74].

Yoshida et al. studied the effect of Cr and temperature on defect accumulation using HVEM [75]. It was shown that under electron irradiation, the nucleation and growth of interstitial loops was slower in the presence of Cr compared with pure Fe, and the nucleation rate had a very strong dependence on irradiation temperature. Compared with pure Fe, the saturation of Fe 10Cr

[2] For a further discussion of void-swelling, see section 1.4.4

happened at a much higher loop density (**Fig.1.4.2.2**). It was also observed using EDS analysis that Cr was enriched on the interstitial loops.

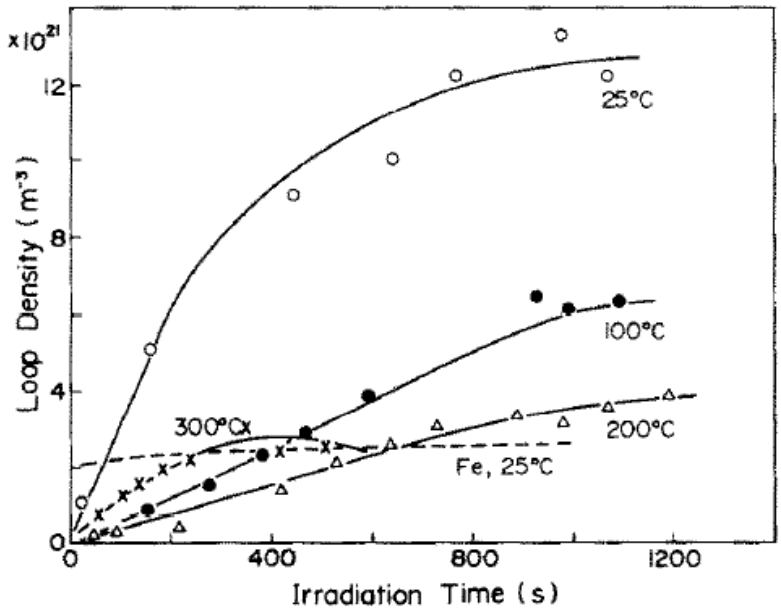

Fig.1.4.2.2 Irradiation time dependence of loop density in Fe-10Cr at several temperatures. Data for Fe at 25 °C are also shown for comparison. [75].

It was shown by Arakawa and his co-workers [76], that the presence of Cr in Fe had the effect of reducing the motion distance and frequency of 'loop jumping' (refer to [60, 76] for video of this loop motion) under electron irradiation. In addition, under post-irradiation annealing, the motion frequency of loops in Fe-9Cr was significantly reduced by Cr. It was concluded that the presence of Cr atoms has the effect of suppressing the motion of loops and therefore enhances the production of defects by minimising annihilation (refer to **Table.1.4.2.2**) [76].

Values of quantities related to the motion of interstitial-type dislocation loops in pure Fe and Fe–9Cr under high-energy electron irradiation with a beam flux of 1×10^{24} e^-/m^2s below a fluence of 6×10^{25} e^-/m^2. The 'motion frequency' is defined as the ratio of the number of the occurrence of one-dimensional motion of loops to the number of all the loops per second

	Temperature [K]	Pure Fe	Fe–9Cr alloy
Motion frequency [%/s]	190	32(±8)	7(±2)
	295	1.0(±0.3)	12(±4)
	375	< 0.4	1.0(±0.3)
Motion distance [nm]	190	20(±10)	10(±3)
	295	30(±8)	10(±3)
	375	–	10(±3)
Volume density [/m^3]	190	2×10^{22}	1×10^{22}
	295	3×10^{21}	$<2\times10^{22}$
	375	1×10^{21}	$<7\times10^{21}$
Size [nm]	190	< 20	< 20
	295	< 20	< 10
	375	< 100	< 10

Table.1.4.2.2 Values of quantities related to the motion of interstitial-type dislocation loops in pure Fe and Fe-9Cr under high-energy electron irradiation [76].

Matijasevic et al. [77] have studied Fe-Cr model alloys under neutron irradiation in the Belgian Reactor 2 (BR2). Both a<100> and a/2<111> dislocation loops were observed in these experiments. These authors found that the sizes of damage clusters increased with dose but decreased with Cr concentration. It was also found that the density of defect clusters saturated at about 0.6dpa.

Damage development in Fe-Cr alloys has also been studied by Jenkins et al. [70] and Hernandez-Mayoral et al. [63] using in-situ heavy-ion irradiations. At 300^{o}C, damage evolution was qualitatively similar to the case of UHP Fe. Strings of loops formed at doses of about 10^{19} ions m^{-2}. The strings developed into resolvable dislocation loops at a dose of about 2 x 10^{19} ions m^{-2}. Finger-like loops were seen in the 300^{o}C experiment, but on a much finer scale than in pure Fe. Loop coalescence was suppressed in Fe-8Cr compare to the case of UHP Fe. In Fe-8Cr specimens irradiated at 500^{o}C, the authors found

a<100> interstitial loops with few (if any) **b**= a/2<111> loops. This trend of a change in Burgers vector with irradiation temperature was the same as that found in UHP Fe. The overall damage structure at 500^{o}C was also very similar to that found in UHP Fe, except that the damage was on a much finer scale with much higher loop number densities. Small voids were also found in this material at the highest dose.

1.4.2.3 Ferritic/martensitic steels

Some remarks on the irradiation response of F/M steels have already been made in chapter 1.3. Here some other studies are briefly reviewed.

Allen and his co-workers have recently studied the irradiation resistance of HCM12A F/M steel [78, 79]. This steel was irradiated with 3.2MeV protons to 10dpa at 400^{o}C and with 5MeV Ni ions to 50dpa at 500^{o}C. The hardness was measured using nano-indentation and was found to increase with dose until saturation at approximately 5dpa, where the hardness increment was about 70%. The corresponding increase in yield stress was roughly 520-550MPa. Owing to the lack of visible dislocation loops and voids under TEM examination, the authors suggested that the increase in hardness is attributed primarily to precipitate formation [78, 80].

Allen et al. also studied the microstructure of the F/M steels T91 and 9Cr-ODS under 5MeV ion irradiation. It was found in T91 specimens irradiated at 500^{o}C

to 150dpa that some dislocation loops were present and all loops were found to have **b** = a<100>. However the dominant microstructural feature was dense dislocation tangles. In 9Cr-ODS, no loops were identified. The microstructure change due to irradiation in 9Cr-ODS was very small. A 25% reduction in the size of Y_2O_3 particles was observed at 150dpa. No voids were observed in either material under irradiation [79].

1.4.2.4 Other steels

There has been much work on the irradiation response of other classes of steels [17]. Work by Fujii and his co-workers [62] observed dislocation loops in A533B reactor pressure vessel (RPV) steel following a 3MeV Ni^{2+} ion irradiation to 1dpa. The irradiation was carried out at 290°C with dose rate and dose of 1.6 x 10^{15} ions m^{-2} s^{-1} and 1.6 x 10^{19} ions m^{-2} respectively. Small dislocation loops of size 2-6nm were observed after irradiation and all the loops that could be analysed by **g.b** contrast experiments had **b** = a<100>. Loops with **b** = a<100> were observed even after post-irradiation annealing, which suggests that the nature of the loops was interstitial.

Hernandez-Mayoral et al. [81] recently studied the RPV steel and its model alloys (i.e. FeCu, FeMnCuNi and FeMnNi) under neutron irradiations. It was found that both density and size of the damage microstructure increased with irradiation dose. The presence of solute atoms such as Cu, Mn and Ni had a strong effect in decreasing the size of the damage microstructures. It was

observed that for the same dose, the defect size decreases as the material becomes more complex with the RPV steel itself having no observed defect at any dose carried out in the experiment.

1.4.3 Comments on the Burgers vector of dislocation loops in ferritic materials

As described above, dislocation loops have been observed in ferritic materials irradiated by heavy-ions, neutrons and electrons. In thin foil experiments, loops in thin regions were believed to be vacancy in nature, whereas in bulk experiments, the nature of loops was usually determined to be interstitial.

In α-Fe and other ferritic alloys, both **b**= a<100> and **b** = a/2<111> loops were observed in most (if not all) experiments where Burgers vectors were determined. Both vacancy and interstitial loops were found with both Burgers vector types [64, 65, 82-85]. The relative properties of the two types of loops depend on the alloy composition, but often they occur in similar proportions. The observation of both Burgers vector rather than predominantly a/2<111> is different compared with other bcc metals such as Mo and V [82]. Based on continuum elasticity estimates (elastic energy proportional to Gb^2, where G is the shear modulus), a/2<111> loops would be expected to be energetically favoured, and therefore the presence of <100> loops was puzzling and not well understood.

In 1965, Eyre and Bullough [66] proposed that during irradiation, interstitial loops in bcc metals can nucleate on the {110} plane with Burgers vector a/2<110>. Such loops enclose a high-energy stacking fault, and at early stage in their growth, the stacking fault is removed by shear in either an a<100> or an a<111> direction, and as a result, loops with **b**= a/2<111> and **b**= a<100> are produced, respectively [66].

However, Marian and his co-workers disagreed with Eyre and Bullough's explanation on the formation of a<100> loops [86]. Marian et al. claimed that the high stacking-fault energy of bcc materials discounts the formation and stability of faulted loops and argued therefore that Eyre and Bullough's theory is not plausible to describe the formation of a<100> loop. They proposed instead a new explanation for the nucleation and growth of the a<100> loops, based on MD simulations. Such simulations showed that self interstitial atoms (SIAs) produced in collision cascades initially aggregate as small a/2<111> clusters. a<100> clusters are initially formed on {110} planes by interaction between two a/2<111> clusters of comparable size [87, 88]. The a<100> cluster can then rotate to an {100} plane as it grows in size. It was shown that a<100> loops are immobile and metastable with respect to a/2<111> loops [86, 87].

The transformation of the Burgers vector of dislocation loops has been observed experimentally. Recent work of Arakawa has shown that the Burgers vector of small loops may change upon high energy (1MeV) electron irradiation or simple heating [76]. It was observed that transformation occurs

from an a/2<111> Burgers vector either to another a/2<111> type, or to an a<100> type. Loops with **b**= a<100> were also observed to transform to a/2<111> loops.

Recent calculations by Dudarev [72, 73] explained the presence of a<100> loops in bcc Fe by considering the effect of crystal anisotropy. These authors showed that in bcc Fe, due to spin fluctuations, an elastic instability is developed near the α–γ phase transition temperature (T_c = 912^{o}C), resulting a dramatic reduction of the shear stiffness constant C'. This reduction in C' has a strong effect on the anisotropic elastic self-energies of dislocations and relative stabilities of a<100> and a/2<111> prismatic edge loops. This theory predicts that a<100> loops will become relatively more stable in pure Fe with increasing temperature.

The presence of a<100> loops results in a profound effect on the radiation response of the material. For example, as discussed in chapter 5.4, Gelles [10] has suggested that the presence of predominant a<100> loops has the effect of suppressing void swelling in Fe-3Cr. Little et al. [9] have argued that the evolution of the damage structure and the associated swelling resistance of ferritic alloy is due to the relative rates of nucleation and growth of the two interstitial loop types.

1.4.4 Void swelling of ferritic materials under irradiation

Void-swelling of ferritic steels and alloys has been studied extensively over the last 20 years. Ferritic steel possesses low swelling characteristics under

electron, charged particle and neutron irradiations [9]. **Fig.1.4.4.1** illustrates an ion-irradiated (to 140dpa) duplex alloy (Uranus-50) at 625^{o}C. There are many fewer voids produced in the bcc ferrite grain compared with that in an adjacent fcc austenite grain of similar composition. This is a good demonstration of the swelling resistance of ferrite material.

Fig.1.4.4.1 Micrograph showing void content in adjacent ferrite and austenite grains of the duplex alloy, Uranus-50 (25 000X) [8].

It is believed that when interstitials and vacancies are produced by irradiation at high dose and high temperature, most are lost by mutual recombination or by absorption into sinks such as dislocations. The surviving interstitials aggregate to form interstitial dislocation loops; and the vacancies aggregate to form voids, which can be stabilised by residual surface-active gases or helium

generated by transmutations. The voids can grow by absorbing vacancies because the dislocations act as biased sinks for the preferential absorption of interstitials.

When considering alloys, it was thought in the 1970s that solute atoms have the effect of reducing void nucleation. The picture was that solute atoms trap both vacancies and interstitials with finite binding energy, and form complexes. These solute/defect complexes will the act as sites to allow recombination with incoming point defects of opposite type and thus reduce the number of vacancies that could contribute to void nucleation [89]. This explanation is however, inconsistent with some later experimental observations by Gelles et al. [10].

Gelles et al. used high-dose neutron irradiation in the Experimental Breeder Reactor (EBR)-II to examine the swelling of Fe-Cr binary alloys and Fe-Cr-C ternary alloys. The swelling was examined by TEM and microstructure changes included the production of voids, dislocation loops and networks. It was observed that reduction of chromium to the Fe-3Cr range resulted predominantly a<100> dislocation structures, while increases above Fe-12Cr produced predominantly a/2<111> dislocation structures. The void swelling was minimised for low chromium content (i.e Fe-3Cr range), and the peak swelling of 0.7% was found in Fe-9Cr as shown in **Fig.1.4.4.2.** Gelles et al.'s work is consistent with that of Little and Stow [11] (**Fig.1.4.4.2**) if one ignores dose variations. The minimum swelling observed in Fe-3Cr was then explained as due to the existence of predominant a<100> loops, which are

considered sessile (unable to move conservatively) and thus have small mobility. The decrease of swelling at higher chromium content (>9Cr) is likely due to the presence of precipitates. The (EBR)-II experiment was later confirmed by Katoh, Kohyama and Gelles (1995) [90] at the Fast Flux Test Facility Materials Open Test Assembly (FFTF/MOTA). The irradiation was done to a higher dose level and similar results was achieved, in particular, it was found 9%Cr still had the highest swelling.

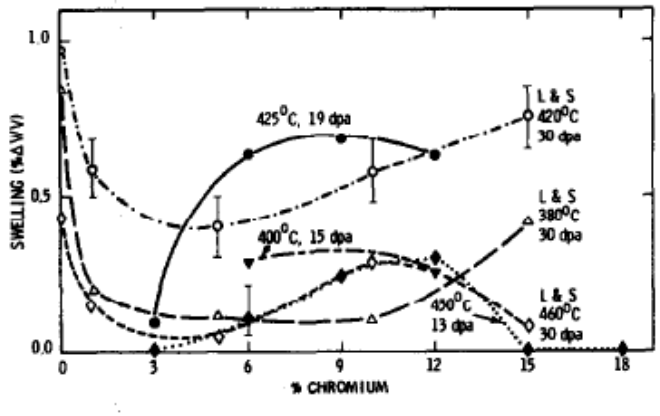

Fig.1.4.4.2 Effect of Cr content on swelling [10].

Parollo et al. have also worked on void-swelling of Fe-Cr alloys. The irradiation was carried out at 400°C in the BR-10 fast reactor to doses in the range 5.5-7.1dpa. As shown in **Fig.1.4.4.3**, the result of the work of Parollo et al. agrees well with that of Gelles et al. [74].

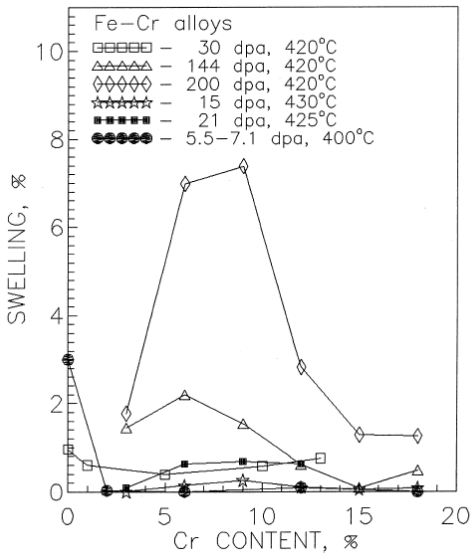

Fig.1.4.4.3 Effect of Cr content on swelling [74].

It was also reported that both ultimate and yield strengths in neutron irradiated FeCr alloys increase monotonically with increasing Cr content (**Fig.1.4.4.4**).

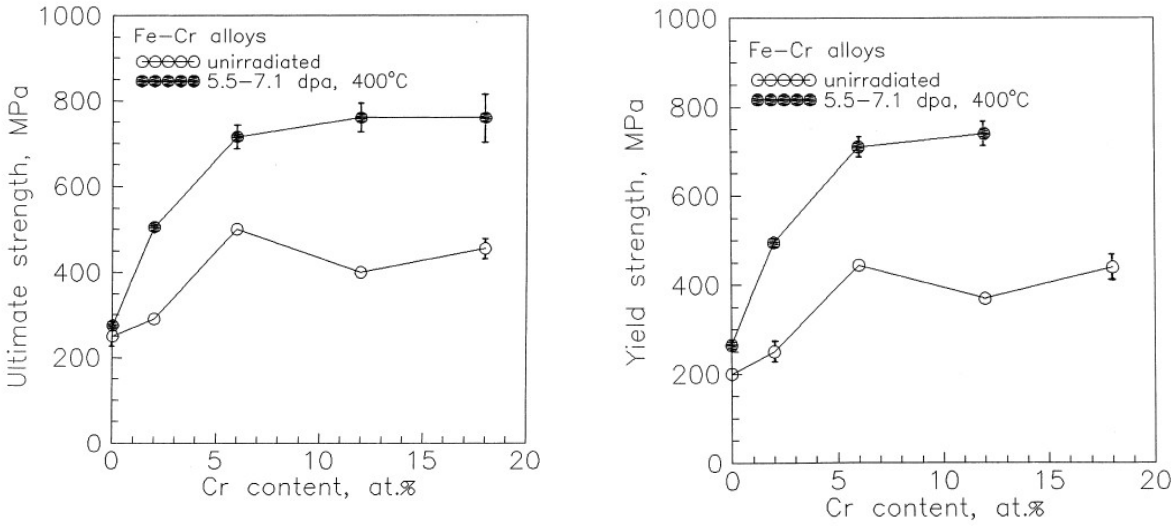

Fig.1.4.4.4 Effect of Cr content on ultimate strength (left) and yield strength (right) [74].

Although later work by Garner and his co-workers [91, 92] suggested a much higher steady-state swelling rate than Gelles et al.'s for Fe-Cr alloys, the Cr dependence of irradiation induced swelling was found to be similar to previous work by Gelles.

Recently, Tanaka et al. [93] have studied the swelling of Fe-Cr alloys under multi-ion irradiation. The irradiation was done at TIARA Takasaki with single, dual and triple ion beams consisting of Fe^{3+}, He^{+} and H^{+} ions at temperatures 470-600^{o}C. As shown in **Fig.1.4.4.5**, for both 9 and 12Cr, the swelling is much higher under triple ion irradiation (self-ion and He+H) compared with dual ion irradiation (self-ion and H or He). The triple ion irradiation produced larger cavities and higher swelling, and so demonstrates the synergistic effect of He and H irradiation in Fe-Cr. The swelling peak under triple ion irradiation was found to be 4% in Fe-12Cr at 510^{o}C. **Fig.1.4.4.6** shows the cross-section view and the TRIM calculation for a Fe-12Cr irradiated to 50dpa at 510^{o}C. Swelling in an ODS ferritic alloy was suppressed to less than 0.01% under the same irradiation condition to 50dpa [93].

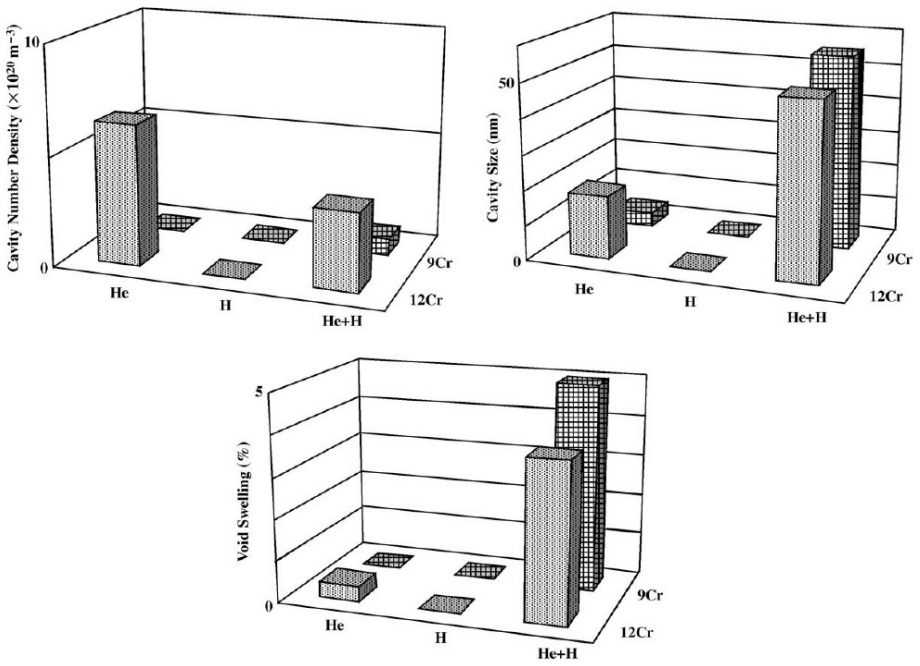

Fig.1.4.4.5 Synergistic effect on cavity number density, size and swelling, developed in 9Cr and 12 Cr alloys irradiated at several consitions [93].

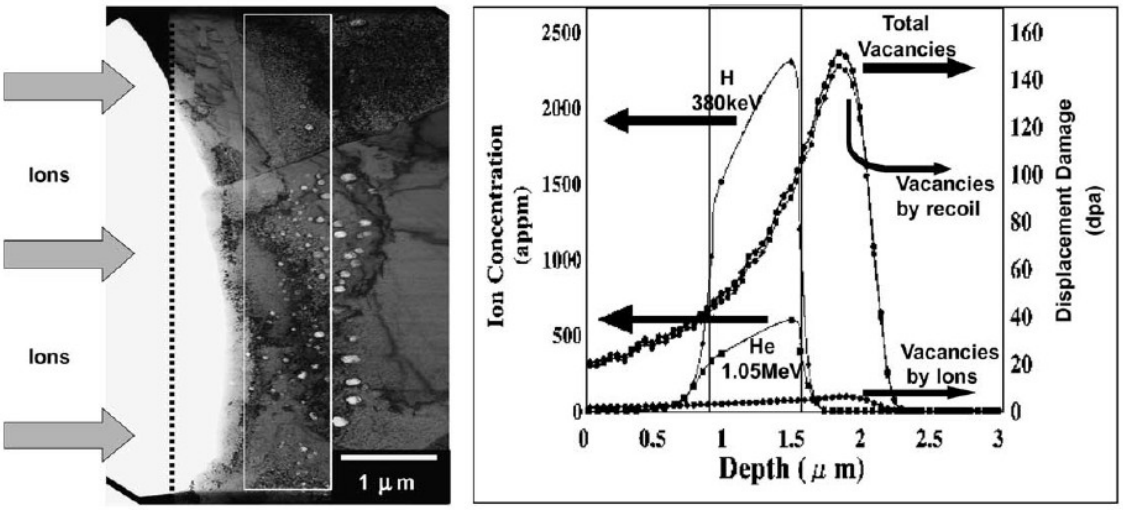

Fig.1.4.4.6 Cross section view and TRIM calculations for an Fe-12Cr alloy irradiated to 50dpa at 510°C [93].

1.5. Summary of literature

To summarise, displacement cascade collapse to visible loops does not occur in pure iron under self-ion irradiation below overlap doses. This is consistent with low-dose neutron irradiations where visible loops do not appear in the matrix. Irradiation with heavier ions (>Ga^{+}) can however cause spontaneous collapse of cascades. Determination of the nature of small loops is very difficult but there is evidence of the existence of vacancy loops in thin-foil experiments. Both **b**= a<100> and **b**= a/2<111> loops were observed in almost all experiments.

Micro-structural evolution in Fe-Cr alloys under low-dose heavy-ion irradiation generally exhibits very similar properties to the pure iron. Both **b**= a/2<111> and **b**= a<100> loops are observed in roughly equal amounts. In-situ TEM experiments show that the threshold dose for visible damage is lower in Fe-Cr alloys; however the mechanism of the effect of the Cr content on damage production is not yet established.

In steels, damage development at low doses usually cannot be analysed by TEM. Therefore work been focused on high-dose damage effects (such as void-swelling) and the effect of He. It seemed damage accumulation in these materials is similar to other ferritic materials. Both **b**= a/2<111> and **b**= a<100> loops were observed, and the loops was thought to be interstitial in nature. In respect of irradiation induced hardening and embrittlement, it is found that both the DBTT and ΔDBTT are at minimum for alloys with 9%Cr, although the mechanism responsible for this effect is not understood. In the

high dose regime, it is found that ferritic materials generally exhibit much better swelling resistance than austenitic alloys. It has been observed in several experiments that alloys with 9%Cr have the biggest swelling after irradiation. A possible explanation to this is that swelling is suppressed by predominately sessile dislocations (**b**= a<100>) at low Cr content (~3%), and by segregation at high Cr content (12%Cr). The synergistic effect of transmutation H and He gasses on the effect of swelling has been confirmed in recent experiments, and such effects appear to be significant. The ODS F/M steels have revealed enhanced properties in the respect of void swelling and low temperature hardening resistance, however, extensive study of such steels needs to be carried out.

Chapter 2: Experimental Methods

2.1. Introduction

This chapter describes some of the experimental methodologies employed in this project. The heavy-ion irradiation experiment and the specimen preparation techniques will be explained in detail. The electron microscopy techniques are included separately in the next chapter and will not be described in this chapter.

2.2. Fe and Fe-Cr Specimens

Both Fe and Fe-Cr materials investigated were polycrystalline. The pure iron specimens were of 5N purity and contained about 0.01wt% impurities including 0.013% C [60, 68]. The Fe-Cr alloys were supplied by Metal Crystals and Oxides Ltd., Cambridge as cold-rolled foil of thickness 0.1 ~ 0.3 mm, with purity 99.99+%. Before irradiation, specimens were thinned to a thickness of 100μm using mechanical grinding and punched into TEM 3mm discs before final pre-irradiation polishing. The techniques used for this are described in chapter 2.4.1.

2.3. Irradiation

Irradiations for this project were carried out at the Surrey Ion Beam Centre. The facility consists of a Van De Graff Ion Accelerator, which is capable of producing heavy-ions of energy up to 2MeV (**Fig.2.3.1**) [94]. The irradiation was done in a vacuum of the order 10^{-5} Torr.

The specimen was mounted to a heatable target holder which is capable of heating up to a maximum of 800^{o}C (**Fig.2.3.1**). The temperature of the heating stage was controlled by a heating unit as shown in **Fig.2.3.2**. When the system is switched on, the actual temperature of the wafer holder is measured by a thermo-couple and can be read on an electronic temperature controller. The controller compares the actual temperature with the desired one and switches on/off the heating element by relays K to keep the target holder to the desired temperature. The error of the set temperature is within 10^{o}C [95].

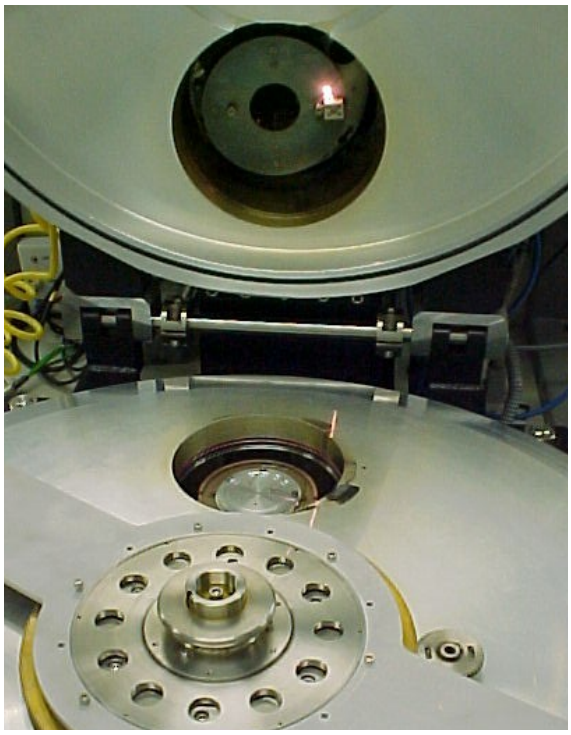

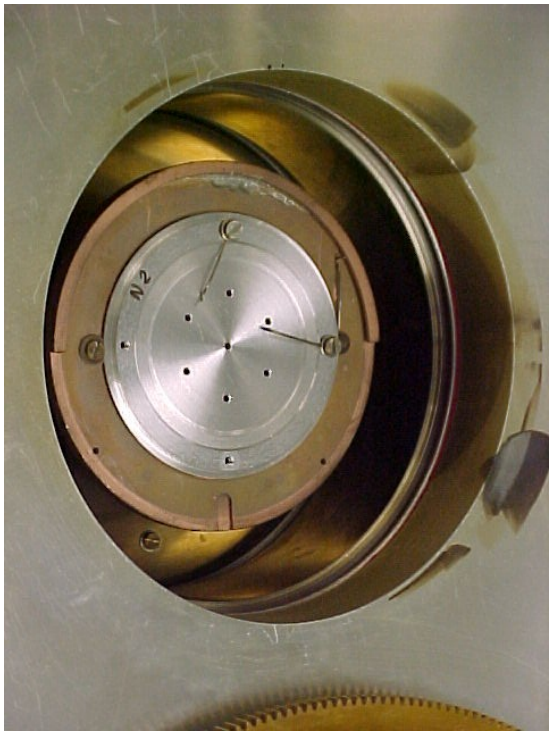

Fig.2.3.1 (a) Accelerator used for implantation; (b) Target chamber; (c) Heating stage with diameter about 10cm.

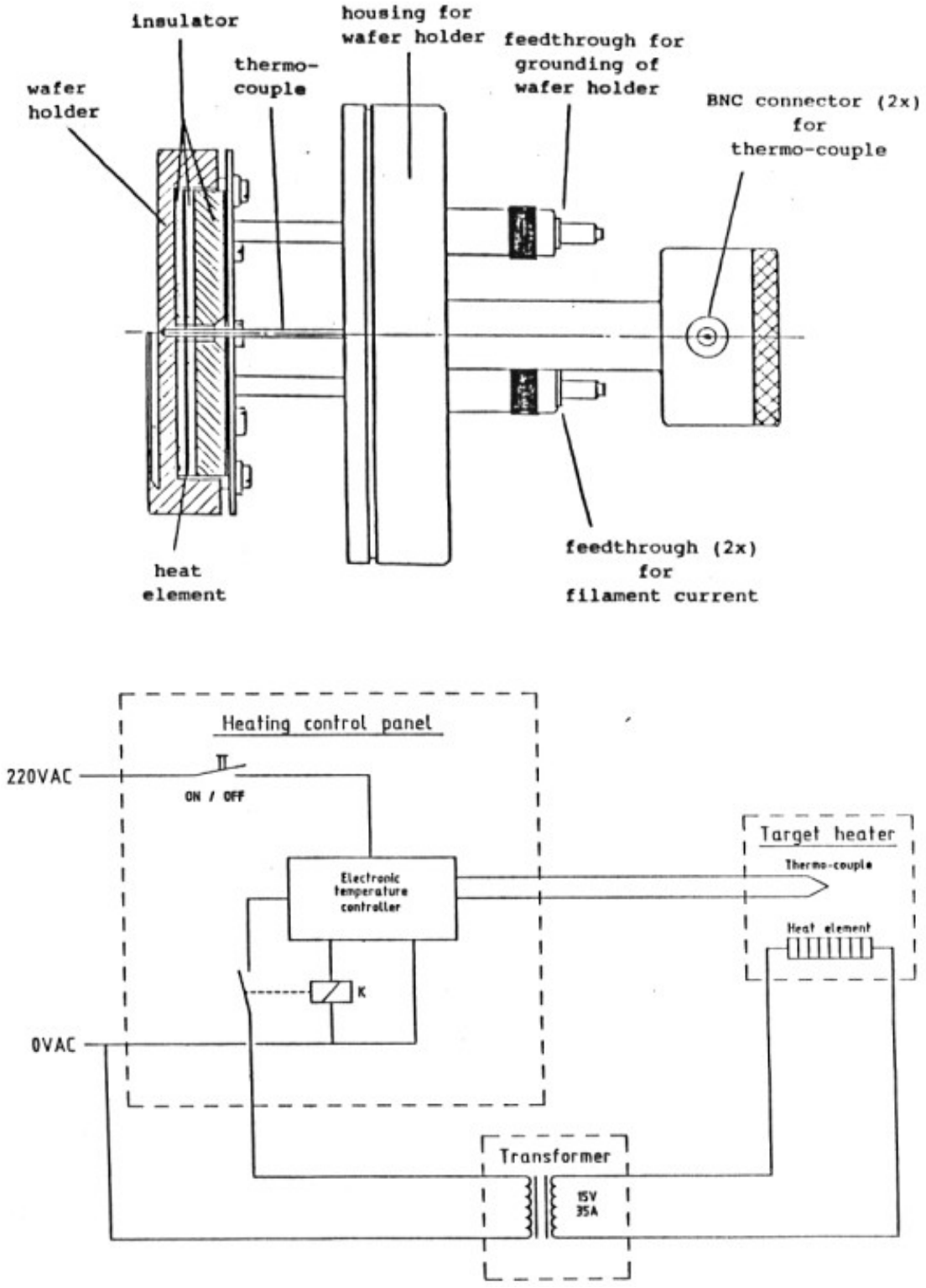

Fig.2.3.2 (a) Heatable target specimen holder; (b) Target heating system [95].

Specimen mounting for irradiation

The specimens were put into stainless steel holders (as shown in **Fig.2.3.3**). The holders were then screwed to the plates onto the target chamber heating stage in the ion-beam facility. The contacting surfaces of the holder and the plate were carefully polished to maximise the thermal conductivity.

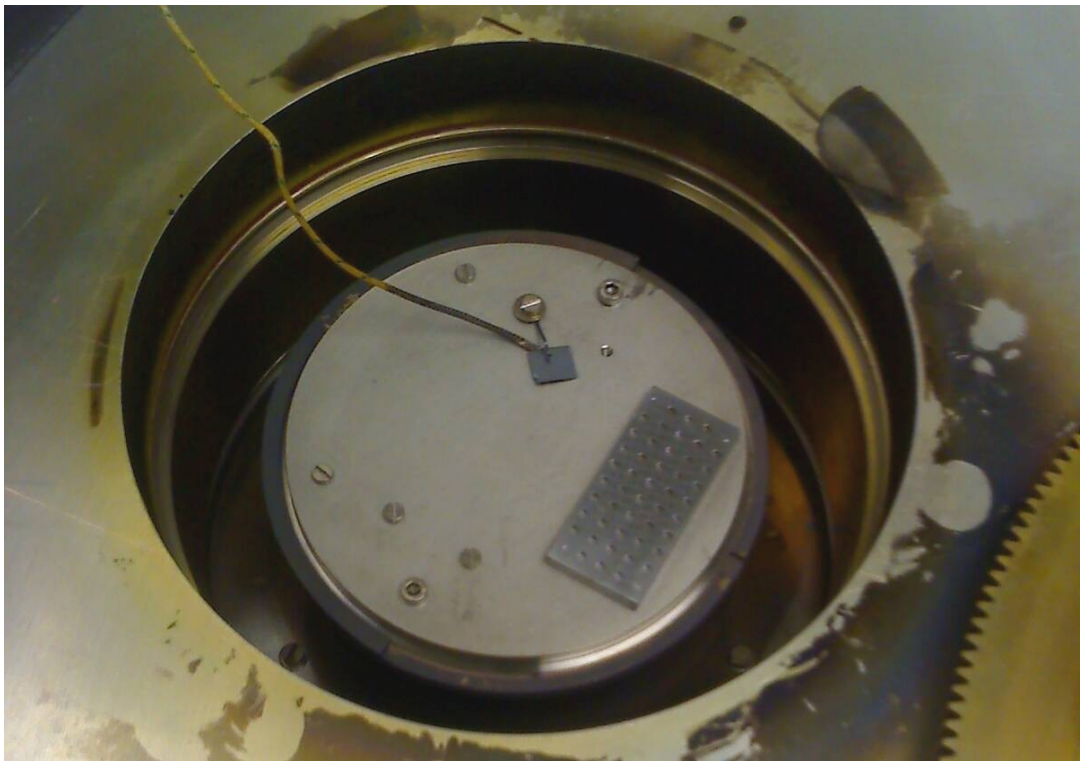

Fig.2.3.3 TEM specimen holder with capacity of holding 46 discs, mounted on the hot stage in the target chamber. The wire clamped to the plate was an addiction thermal couple used for temperature calibration. It was not used during irradiations.

SRIM Calculation:

The first irradiation was carried out at 300°C with a mono-energetic ion beam of energy 1.5MeV. It was not possible to produce 2MeV ions due to technical problems of the accelerator. The irradiation was done to the dose of $1x10^{19}$ ions m^{-2}. A calculation using the Stopping and Range of Ion in Matter (SRIM) programme [96] showed a damage peak of 2.5 dpa buried under the surface at a depth of about 400-500nm (**Fig.2.3.4**). A displacement energy of 40eV was used in all SRIM calculation in this project [97].

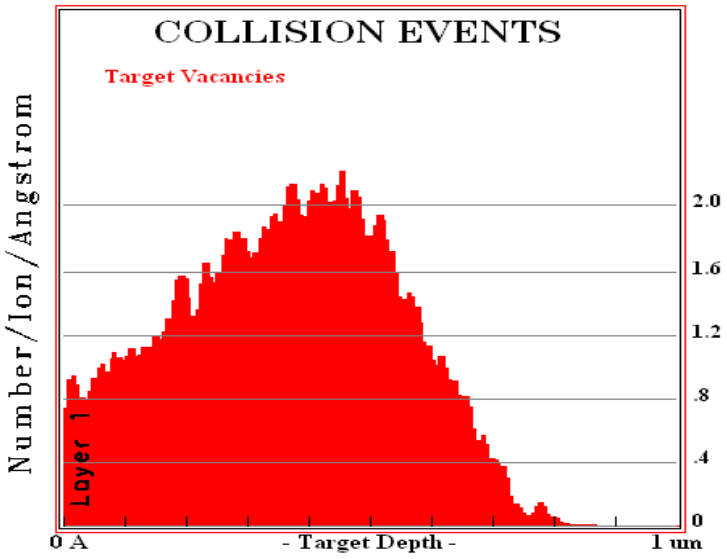

Fig.2.3.4 SRIM calculation of 1.5MeV Fe^{+} ion irradiation on Fe target.

The figure shows that the dose level in a single-energy irradiation has a strong dependence on target depth. This makes specimen preparation very difficult, since the damage dose in TEM specimens is critically dependent on the amount of material removed from the irradiated surface. For subsequent irradiations, a modified irradiation method was applied by using dual-energy

ion implantation. The specimen was irradiated first with 500keV ions, followed by 2MeV ions. The lower-energy irradiation was carried out to a dose half that of the higher-energy irradiation. This resulted in a more 'flat' damage profile, where the damage dose is less dependent on the target depth, as shown in **Fig.2.3.5**. All the experiments carried out in this work were aimed at analysing the peak damaged region. Therefore, unless otherwise specified, all the dpa values quoted in this thesis refer to the maximum dose of the particular irradiation calculated by SRIM.

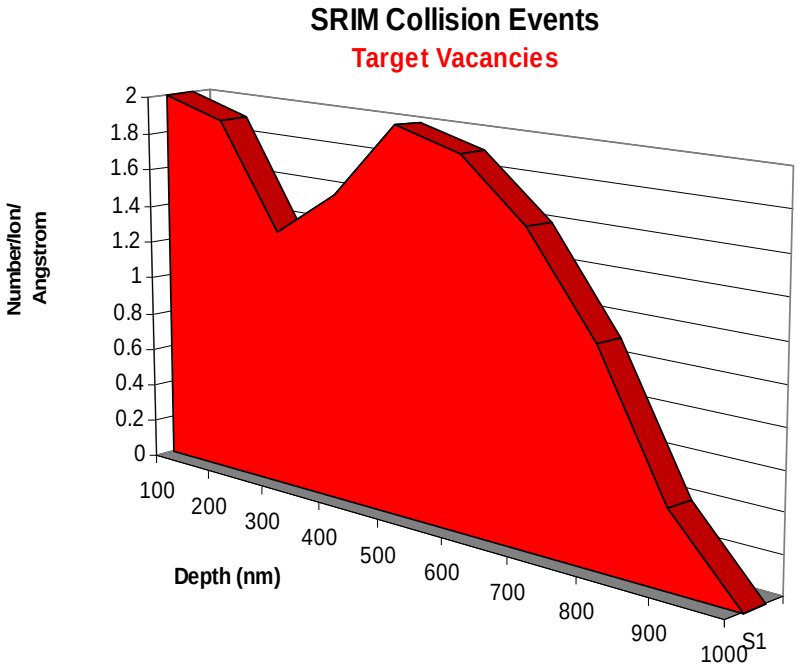

Fig.2.3.5 SRIM calculation of dual-energy (500keV+2MeV) Fe^{+} ion irradiation on Fe target.

Limitations of Irradiations

The damage produced using this method lies in a shallow layer of about one micron from the ion-entry surface. Even though this depth is sufficient to be considered as bulk irradiation (i.e. no significant surface effects during irradiation), the narrow damage range makes TEM specimen preparation very difficult.

The Surrey Ion Beam facility has an unstable beam current, which resulted in an unstable dose rate. **Fig.2.3.6** shows that the dose rate in the 500^{o}C run increased by a factor of about two during the irradiation. The instability of the beam current will also affect the local temperature, which may be increased by up to about 20^{o}C by beam heating. Fluctuations in temperature are therefore likely to be present, and the real specimen temperature is likely to be somewhat higher than that set by the thermostat.

As described above, dual-energy irradiation was used in order to create a flat damage profile. However the two consecutive irradiations using different energies may have an effect on the formation of the damage structures. Energy-degrader would be a preferable method: however this was not possible in the Surrey Ion Beam Centre.

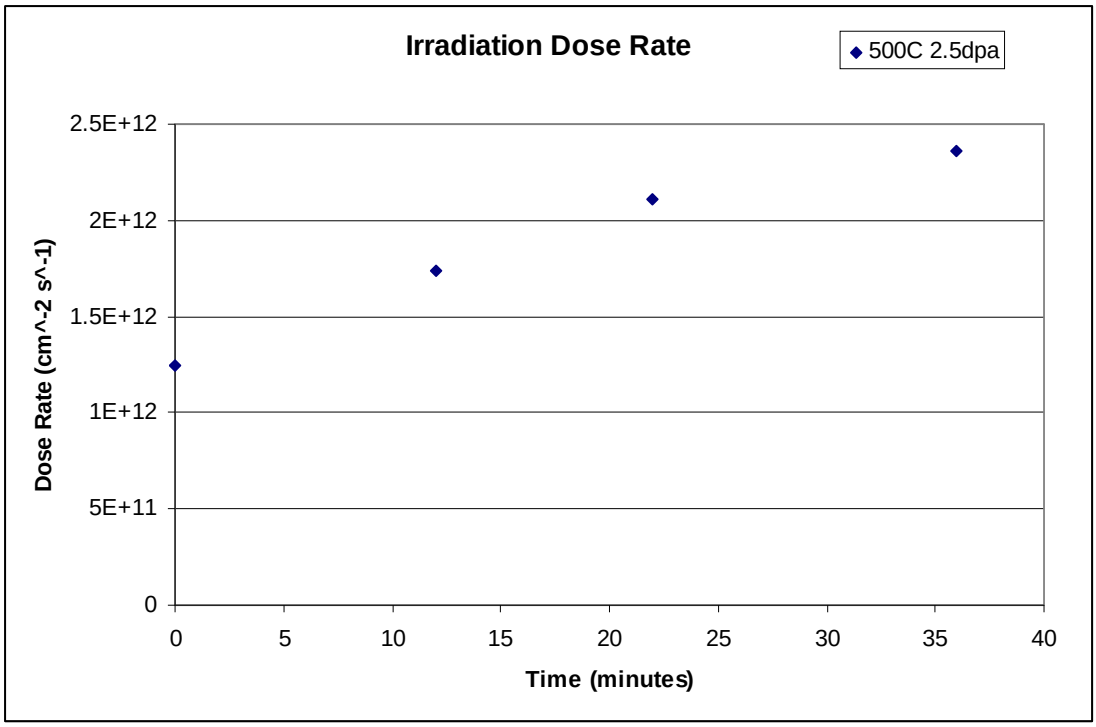

Fig.2.3.6 Irradiation dose rate variation during implantation obtained from Surrey Ion Beam data log.

2.4. Specimen Preparation

Specimen preparation is very important in diffraction contrast experiments in ferritic materials, which are ferromagnetic. The operation of the microscope relies heavily on qualities of the specimen such as its thickness and the position of the hole in the disk. Surface quality is also very important. Fe specimens tend to oxidise quickly on exposure to air. This section will describe the specimen preparation method used both before and after irradiation.

2.4.1 Pre-irradiation Preparation

The aim of pre-irradiation preparation was to achieve a flat, polished irradiating surface that is free of deformation caused by mechanical polishing. In the matrix of the specimen, the dislocation density was reduced by annealing.

Mechanical grinding

Before irradiation, specimens were punched into standard 3mm TEM discs, and thinned to about 100microns by grinding using silicon-carbide paper up to P2500 (FEPA Abrasive P grade with corresponding particle size of 8.4 ± 0.5 microns).

Heat treatment

After thinning, specimens were annealed as a precaution to reduce possible high dislocation densities from the mechanical polishing. In each case specimens were annealed at 800^{o}C for 4 hours in a vacuum furnace (with vacuum of about 10^{-6} mbar) followed by slow cooling (10-20hours). After this treatment all specimens had a simple ferritic microstructure with a low dislocation density. No dislocation loops was observed before irradiation.

Pre-irradiation electro-polishing

After annealing the specimens were electro-polished for a few seconds. This was done to remove any surface deformation caused by mechanical polishing. The conditions of this electro-polishing are described in detail in the next section (chapter 2.4.2.1).

2.4.2. Post-irradiation: Preparation of TEM specimens

The key to the preparation of TEM specimens is to access the peak damage region (as shown in **Fig.2.3.3** and **Fig.2.3.4**) in the microscope. This was done by controlled removal of the top surface, followed by back-thinning to achieve electron transparency [98]. The steps are illustrated in **Fig.2.4.2.1**.

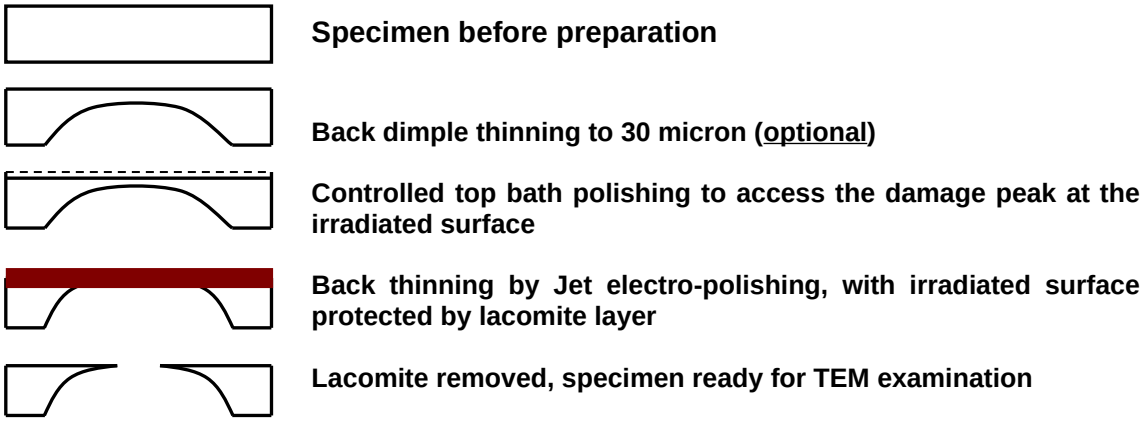

Fig.2.4.2.1 TEM specimen preparation for irradiated bulk specimens

For thicker specimens, mechanical back thinning was usually effected by dimple grinding the un-irradiated surface, to a minimum thickness of less than 50μm. This reduced the time taken for the final jet electro-polishing and thus reduced the possibility of erosion. It also helped to direct the jet to the centre of the disc. However this was not essential for achieving a good TEM specimen.

Top surface removal (using flash electro polishing)

Top-surface thinning is the crucial and most difficult part of the whole preparation process. A very accurate thinning (removal of about 500 nm with a margin of error of ±100nm) is required because the peak damage is very close to the irradiated surface (as shown in **Fig.2.3.3** and **Fig.2.3.4**). This was achieved using a bath polishing technique with accurate temporal control.

The apparatus for bath polishing is shown in **Fig.2.4.2.2**. The specimen was held horizontally with platinum-tipped tweezers with the irradiated surface facing downwards as shown in **Fig.2.4.2.2(a)** [99]. The cathode was a cylindrical metal plate placed concentrically inside the beaker as shown in **Fig.2.4.2.2(b)**. The beaker was filled with electrolyte consisting of 5%$HClO_4$ and 95%methanol. Liquid nitrogen was poured on the electrolyte in order to cool it. A relay timer was connected into the circuit to control the time (down to 0.1 second) for which the current flowed between the specimen and the cathode, while keeping the voltage constant. It was observed that good polishing could be achieved at 30V with a temperature of about -30^{o} C and current of about 2A.

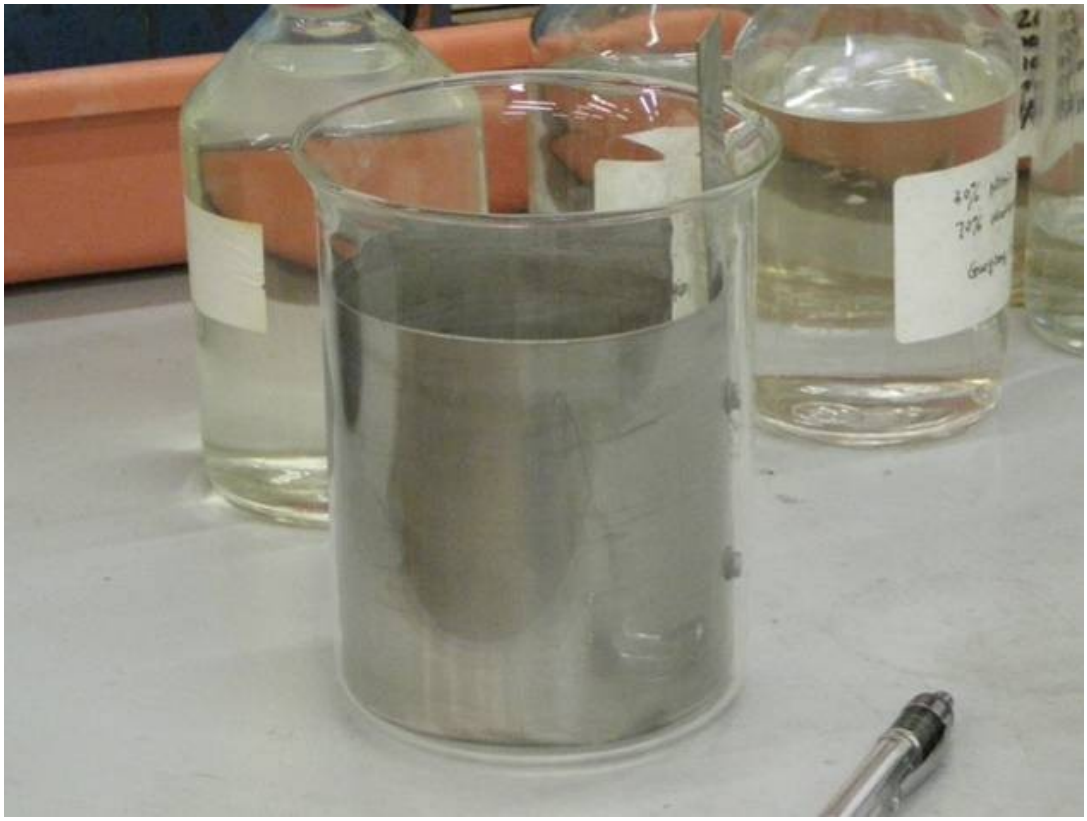

Fig.2.4.2.2 (a) Photograph showing TEM specimen held by platinum-tipped tweezers; (b) Photograph of cathode;

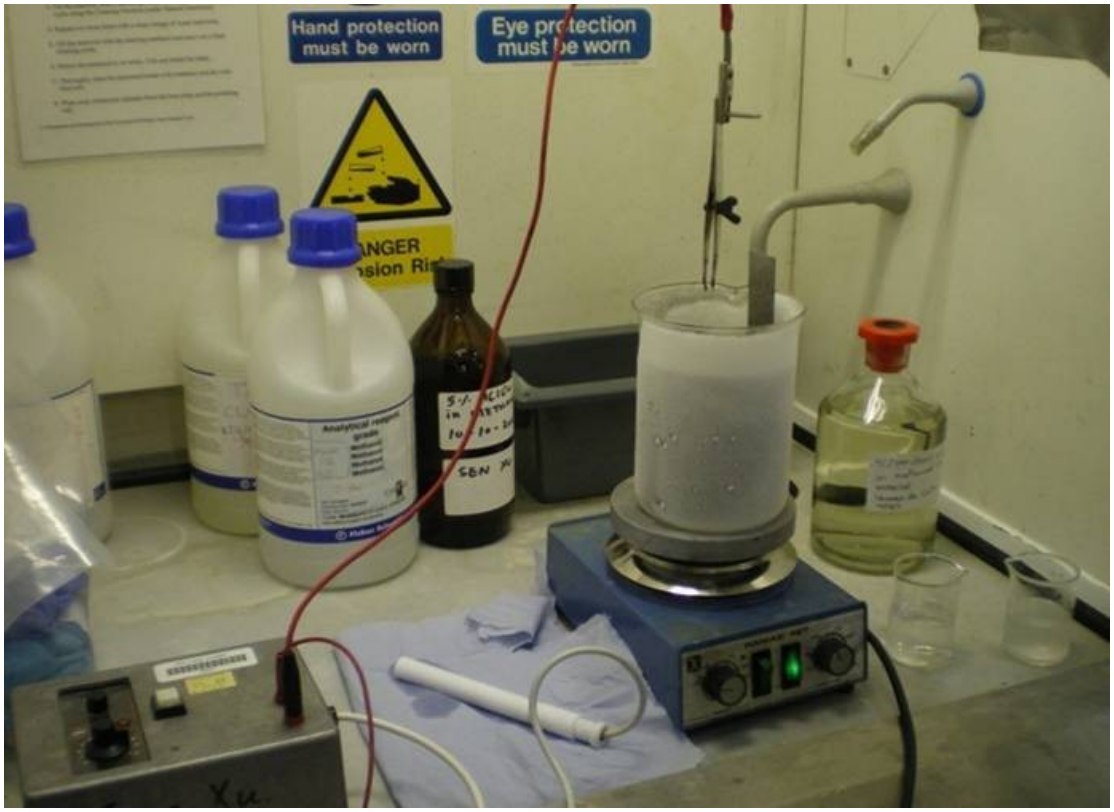

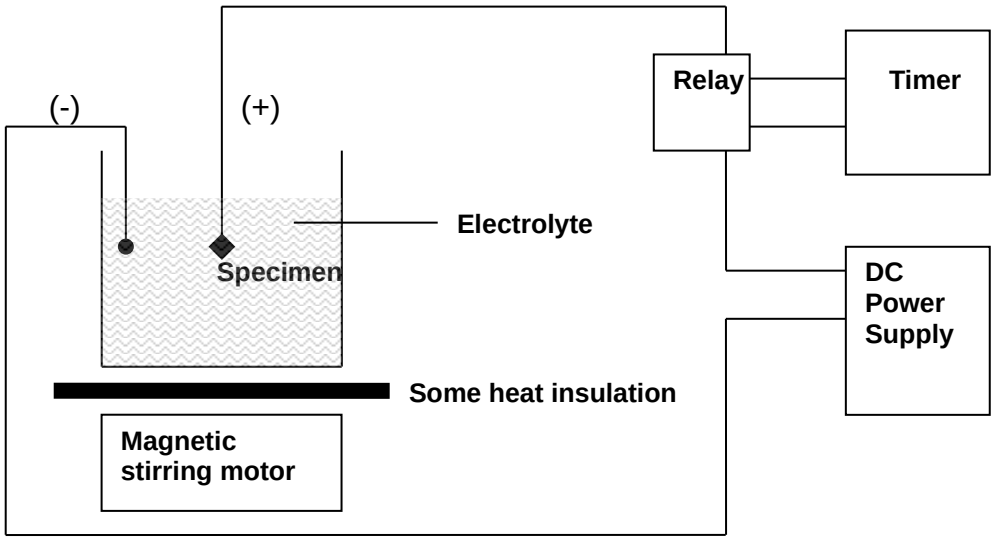

Fig.2.4.2.2 continued: (c) Photograph showing the apparatus for bath electro-polishing; (d) Diagram showing the apparatus for bath electro-polishing technique.

In order to determine appropriate polishing times, the polishing rate was measured by applying both micro-indentation and FIB-indentation. The micro-indent produced on the surface has a top-down pyramid shape which can be used to obtain the depth (**Fig.2.4.2.3(a)**). The diagonal of the square base of the pyramid is seven times its height (depth). Therefore, by measuring the change in diagonal, the amount of material removed can be calculated. However this method produces problems after a few seconds of polishing because the edges of the indent get smoothened by electrolyte, making measurement difficult and inaccurate.

For this reason a FIB-indentation method was also applied. The FIB was used to mill a series of trenches as shown in **Fig.2.4.2.3(b)**. These trenches differed in depth from 100nm to 500nm. After electro-polishing, the amount of material removed was estimated by looking at how much a particular trench was polished away. The two methods were used together, and the polishing rate in a typical case is shown in **Fig.2.4.2.3**. The two indentation methods gave good agreement, with a typical polishing rate of 100±50 nm per second (**Fig.2.4.2.4**).

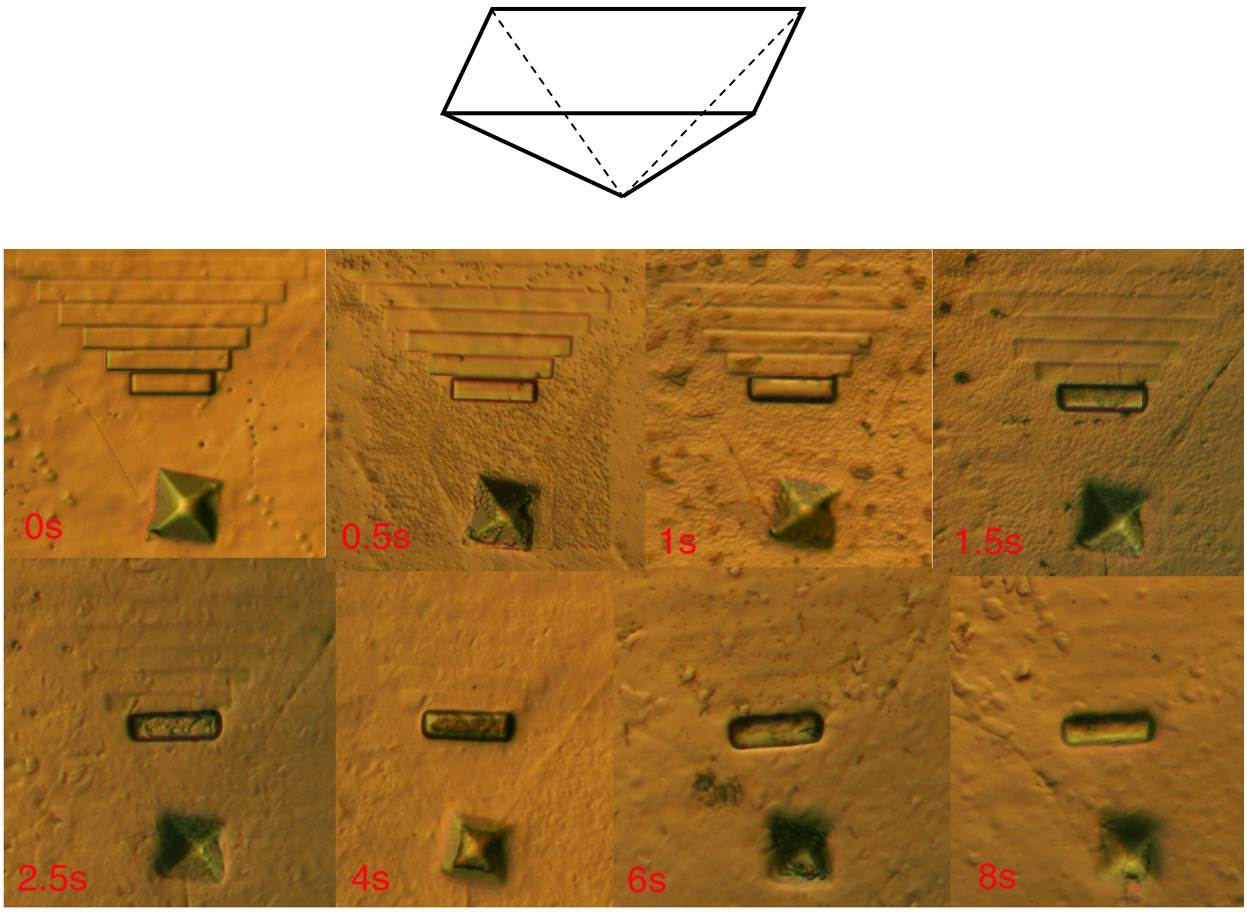

Fig.2.4.2.3 (a) Illustration of a micro indent used to measure the surface removal; (b) Optical micrograph showing surface removal during polishing. The FIB indents consist of a range of depth up to 1micron.

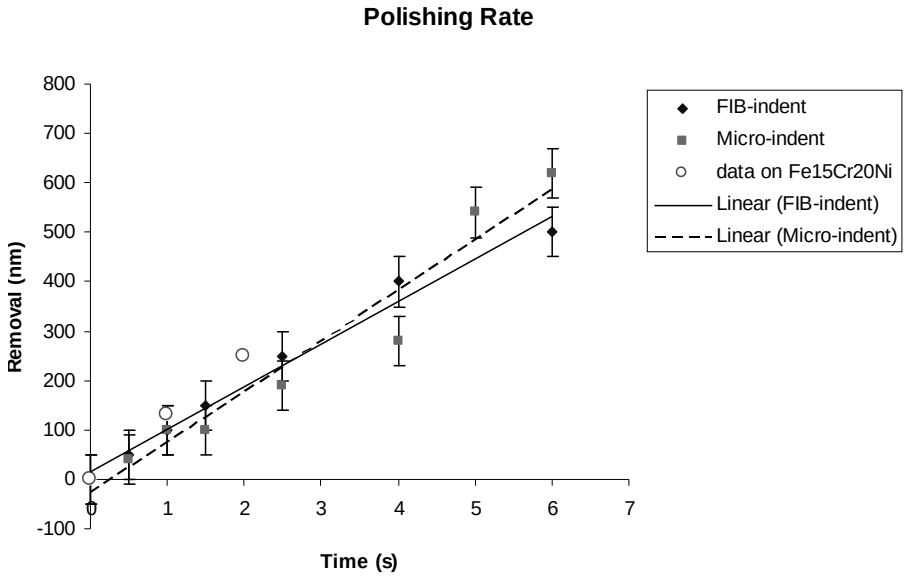

Fig.2.4.2.4 Polishing rate for Fe-5Cr. Circles represent data from Kestel [99] on Fe15Cr20Ni using similar polishing conditions.

It is important to note that the reproducibility of the polishing rate is affected by many factors including electrolyte temperature, stir rates, electrode separations and electrolyte contamination. Therefore, when polishing specimens using this method, it is recommended always to apply FIB indentation on the surface and to polish in small successive time periods.

It was also found that the optimum polishing interval is about one second. For shorter times, good polishing conditions cannot be established and etching usually occurs. Polishing for times longer than one second caused the polishing rate to increase. Therefore to achieve a total polishing time say of five-seconds, it is preferable to apply five consecutive polishes each of one second with the specimen kept in the electrolyte during the whole process.

Back thinning

With the peak damage region revealed by previous step, the final step was to back-thin using jet electro-polishing to make the specimen electron transparent. The process was done using a TenuPol 5 Jet-electropolisher. During the process, the top surface was protected by painting a layer of lacomit varnish. However, this method causes a certain amount of electrolyte to be trapped inside the holder, and may result in the edge of the specimen being polished faster than the centre. This was prevented by painting a ring of lacomit on the back, unirradiated surface to guide the electrolyte to the centre of the specimen.

Finally, the painted lacomit layer was removed with lacomit remover solution and washed in cooled methanol in several consecutive baths.

2.5. Specimen Storage

If possible, specimens were introduced immediately into the TEM after preparation. Otherwise, specimens were stored in ‘dry ethanol’ (ethanol saturated with anhydrous sodium sulphate) where they could remain in good condition up to about one week.

Chapter 3: Transmission Electron Microscopy techniques

Full details of the full range of diffraction contrast and other methods used for characterising radiation damage in the TEM are found in the books of Hirsch et al. [100] and Jenkins and Kirk [55] and will not be described here. We do however describe some of the specialised techniques of particular relevance to this project. Note that the beam direction in this thesis is defined to be the same as the zone axis direction (i.e. pointing upwards), **except** for the case of the inside-outside contrast experiments, where beam direction was defined as the direction of the electron beam (i.e. pointing downwards), in order to be consistent to reference [55].

3.1. Foil Thickness measurements

In the experiments described in this thesis, one of the ways in which radiation damage is quantified by measuring the number of dislocation loops per unit volume. This requires a measurement of the foil thickness in the area under examination.

3.1.1 Convergent beam microscopy

Convergent beam microscopy was used in some cases to accurately measure the thickness of the specimen [101]. First, a strong two-beam diffraction condition was set up using a reflection such as (200). Then a spot-size

(condenser 1 control) capable of producing a fine electron probe (~ 10 nm) was selected, together with a large condenser aperture. The probe was then focussed on the region of interest, and the microscope switched to diffraction mode to produce a series of parallel fringes in the convergent-beam disc (**Fig.3.1.1(a)**). The distance between the centres of the transmitted beam and the 1st order diffracted beam was measured as L_0 as illustrated. The measurements L_1, L_2, L_3… represent the distances between the centres of the diffracted beam to the successive minima. The absolute values of the distances are not important, because only the ratios of the distances are needed in the calculations.

In order to obtain the thickness of the specimen, the following equation was plotted.

$$\left(\frac{S_i}{n_i}\right)^2 = \frac{-1}{\xi_g^{\,2}}\left(\frac{1}{n_i}\right)^2 + \frac{1}{t^2} \qquad \textbf{Equ.3.1.1}$$

where t is the thickness of the specimen, ξ_g is the extinction distance of the excited reflection g, n_i is an integer. S_i expresses the deviation of the i-th minimum from the exact Bragg position and is defined by the following equation.

$$S_i = \frac{\lambda}{d^2}\left(\frac{L_i}{L_0}\right)$$

where λ is the wavelength of the incident beam and d is the spacing of the reflection planes.

The next step was to plot $(S_i / n_i)^2$ versus $(1/n_i)^2$ for different values of n_i (i.e. n_i =1, n_i =2 …) to find out which value of n_i generates a linear profile of

Equ.3.1.1. It was found in this case n_i =3 produced the linear plot shown in **Fig.3.1.1(b)**.

From **Equ.3.1.1**, the intersection on the y-axis gives the value of $\frac{1}{t^2}$ and the gradient of the line is $\frac{-1}{\xi_g^{\ 2}}$. Therefore both t and ξ_g could be obtained directly from the plot.

It was important to obtain the value of ξ_g, even though it was not necessary in the determination of the foil thickness. This is because the value of ξ_g can be used in estimating the foil thickness of specimens using thickness fringes with similar diffraction conditions.

In this particular case the thickness was determined to be 129 ± 20 nm, where the error comes from the uncertainty in the measurements of fringes separations.

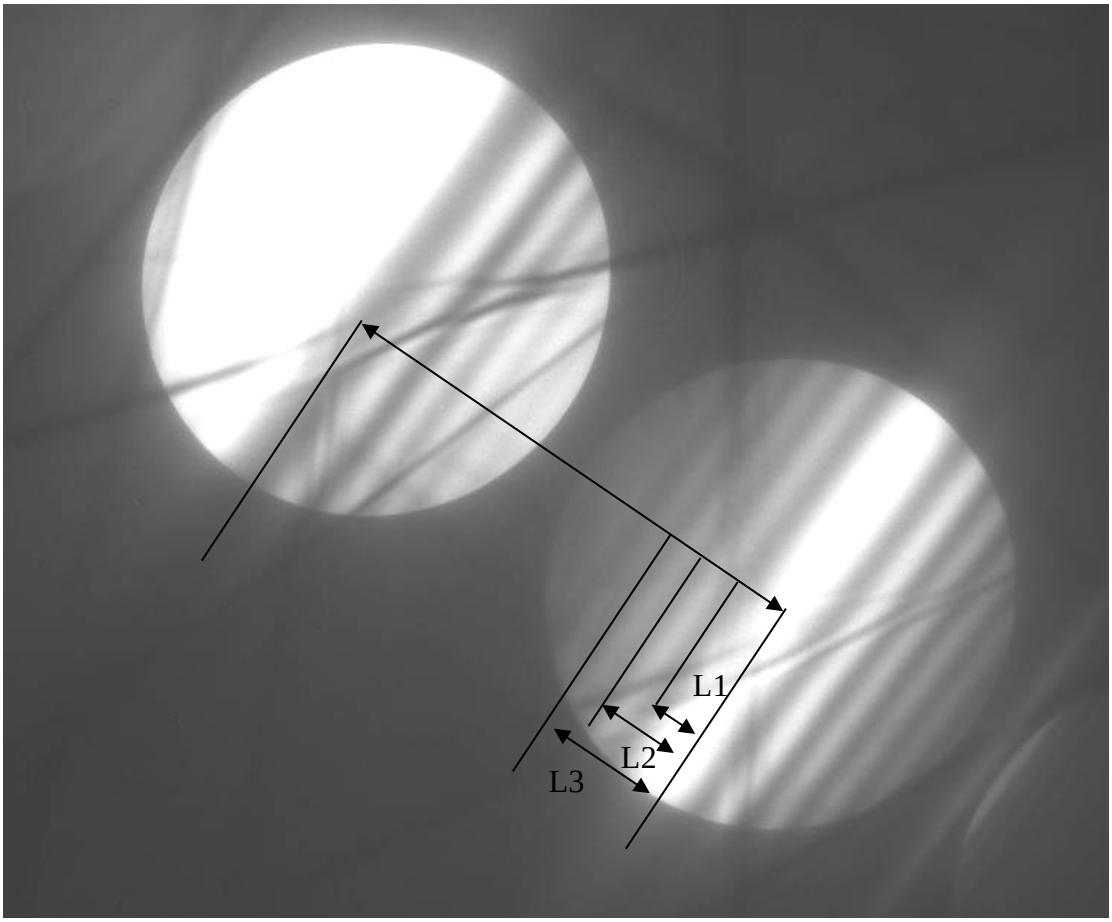

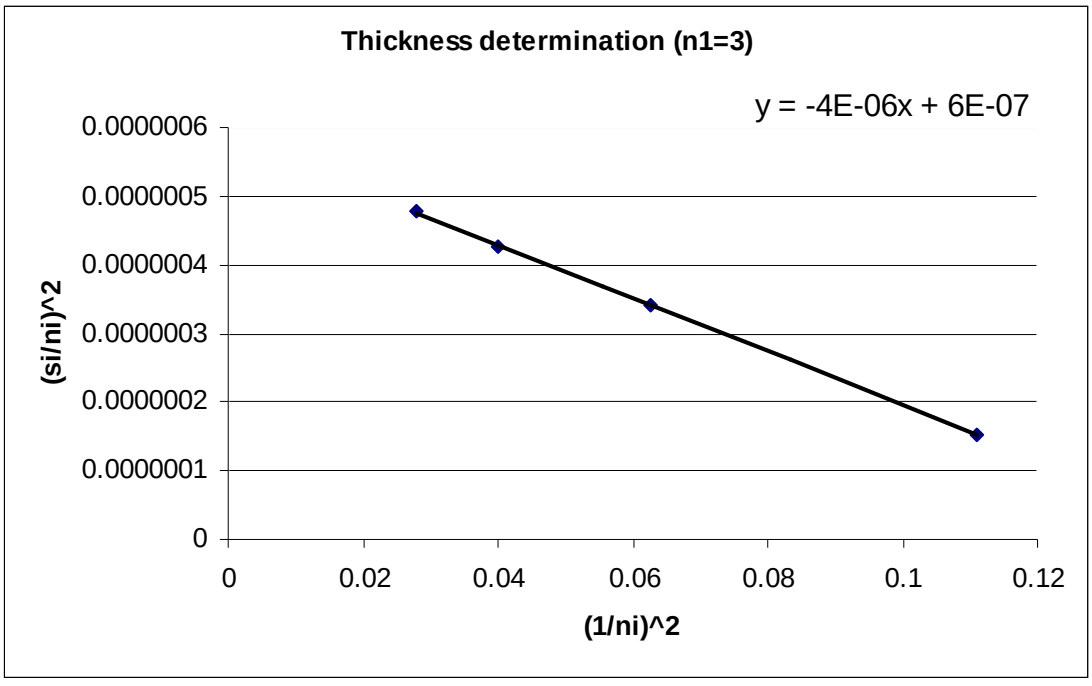

Fig.3.1.1 (a) Convergent beam fringes in the diffraction mode; (b) Graph used to determine the foil thickness.

3.1.2 Foil thickness measurements using Electron Energy-Loss Spectrometry (EELS)

Electron energy-loss spectrometry (EELS) is the analysis of electron energy distribution of inelastic interacted electrons. The inelastic scattered electrons carry a large amount of information about the electron structure of the specimen atoms. By carrying out EELS this information could be separated and quantified. In this work EELS was used to measure the specimen foil thickness .The methodology employed in this work is described briefly in this section. A detailed theoretical background can be found in [102, 103].

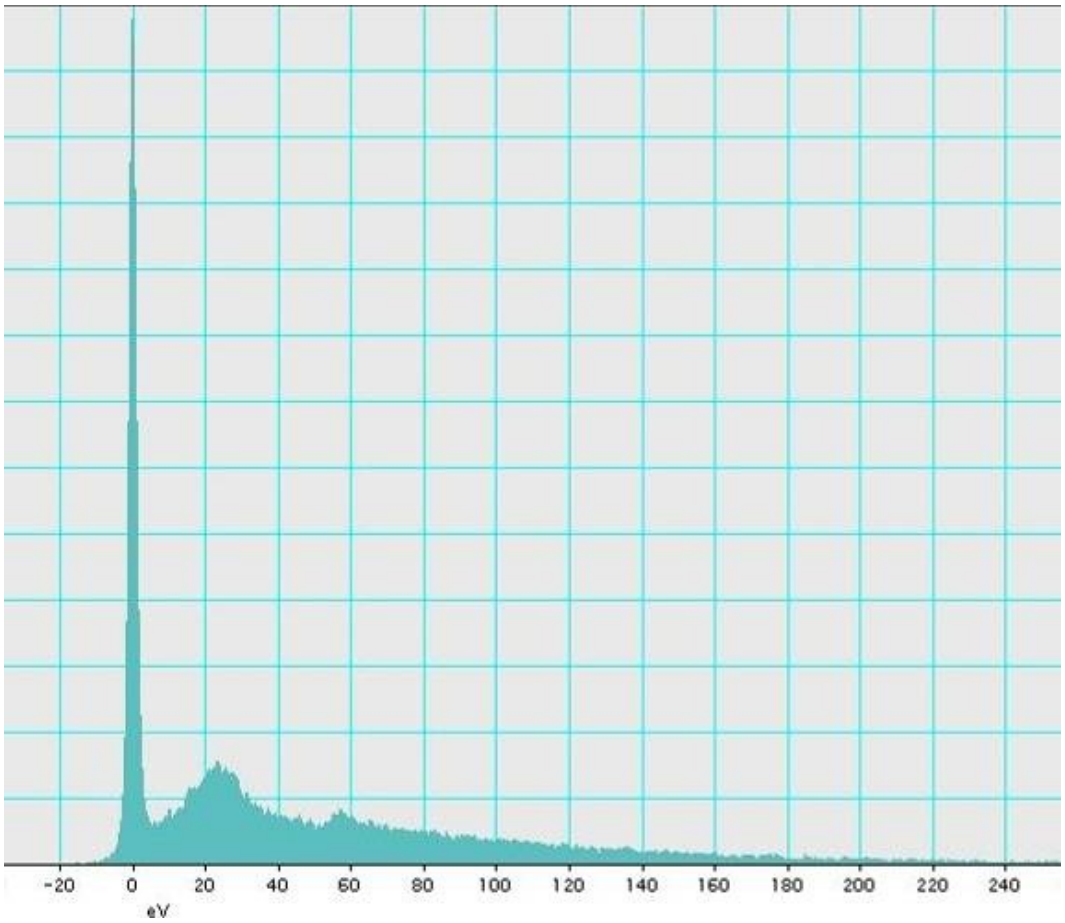

Fig.3.1.2 EELS spectrum of Fe specimen recorded using the JEM-3000F with Gatan Imaging Filter.

Fig.3.1.2 shows an energy-loss spectrum obtained from a Fe specimen (irradiated at 600^{o}C to 7dpa) recorded using the JEM-3000F microscope equipped with a Gatan Imaging Filter. The spectra was acquired in TEM ‘‘image coupling’’ mode with camera length of 12cm (optimum for EELS collection for this mode). Three different collection angles were used for corresponding entrance apertures, these angles were: 8.5mrad for 3mm aperture, 5.5mrad for 2mm aperture and 1.8mrad for 0.6mm aperture. The results were obtained as an average of the measurements using the three collection angles. The main features seen here are a zero-loss peak, and a broad energy loss peak due to plasmon scattering.

The amount of inelastic scatter increases with specimen thickness and such thickness information could be extracted from this energy-loss by estimating the ratio between the intensities of zero-loss peak (I_0) and total intensity in the spectrum (I_T). In practice, due to the rapidly fall of EELS spectrum, the total intensity of the spectrum is represented by the total intensity in the low-loss portion (I_l) of the spectrum up to 50eV.

The thickness t could be measured using the following equation:

$$t = \lambda \ln\left(\frac{I_l}{I_0}\right)$$

Where I_l is the total intensity of the low-loss portion of the EELS spectrum; I_0 is the total intensity of electrons without energy loss (zero-loss peak). In metallic specimens, λ could be represented using the following equation:

$$\lambda = \frac{106FE_0}{E_m \ln\left(\frac{2\beta E_0}{E_m}\right)}$$

Where λ is in nm, E_0 is the electron incident energy measured in keV, and in this case is 300keV;

F is the relativistic correction factor defined as:

$$F = \frac{\left(1 + \frac{E_0}{1022}\right)}{\left[1 + \left(\frac{E_0}{511}\right)^2\right]}$$

And E_m is the average energy loss in eV which for a material of average atomic number Z, can be derived by:

$$E_m = 7.6Z^{0.36}$$

β is the collection angle measured in mrad. Calculations of β have been done for the JEM-3000F and the value of β for the entrance apertures 0.6mm and 2mm are 1.3 and 5.5 respectively.

The accuracy of thickness measurement using EELS is within 20% [103].

3.2. Diffraction Pattern Rotation Calibration

The CM20 microscope does not correct the rotations between the image and the diffraction pattern automatically. Therefore it was important to calibrate these rotations.

As shown in **Fig.3.2**, Molybdenum Trioxide crystals were used to calibrate the angle between the diffraction pattern and the image. In the process of the calibration, the sense of inversion was checked by defocusing the diffraction

pattern in a known sense. In this particular magnification camera length combination, the rotation correction is about 23°.

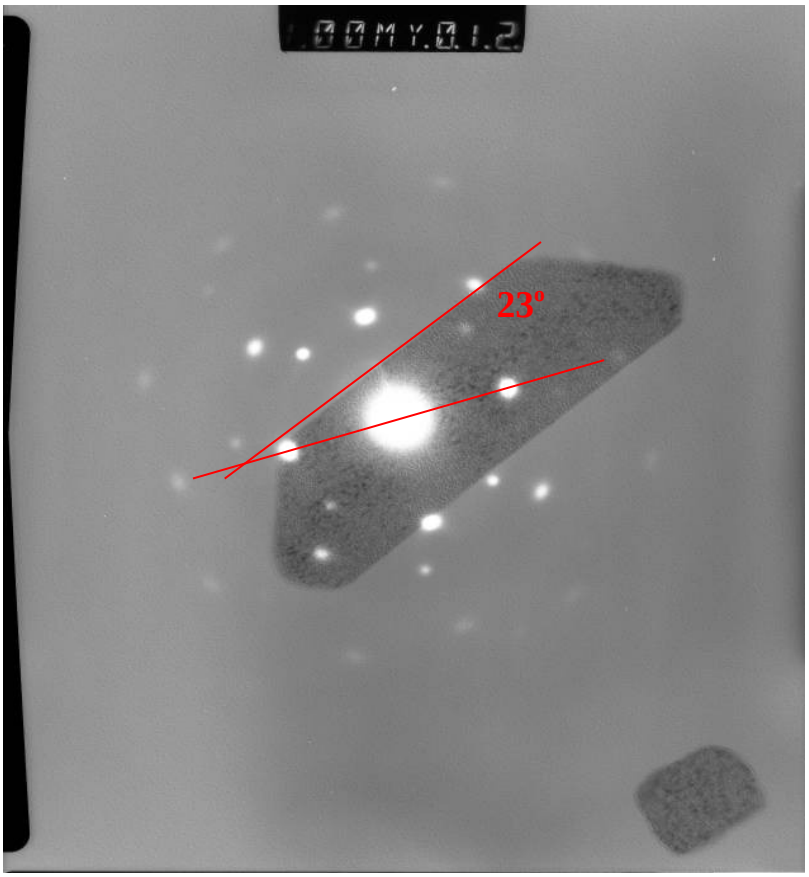

Fig.3.2 A double exposed negative showing both Molybdenum Trioxide crystal and its diffraction pattern.

3.3. Burgers vector analysis

In bcc Fe and Fe-Cr alloys dislocations have two possible types of Burgers vectors: a/2<111> and a<100>, as described in chapter 1.4.3. The Burgers vectors of the loops were determined using the standard **g.b** = 0 invisibility criterion. The detailed background and theory of this technique can be found in [55].

Fig.3.3 is an example of a typical contrast experiment performed to determine the Burgers vectors of dislocation loops. The specimen is Fe-8Cr irradiated at 300^{o}C. The four micrographs were taken near the [001] foil orientation under kinematical bright-field (a two-beam condition with a small positive deviation parameter, i.e. $S_g > 0$) diffraction conditions using the four different diffraction vectors available near this pole. A |**g.b**| table was constructed for these diffraction conditions. Because **g.b** = 0 will give very low (if not zero) image contrast, the type of Burgers vectors can be deduced by observing the appearance of loops in each micrograph. In the figures, the dotted circle marks the loops which have **g.b**=0.

This method is an effective way to determine the type of Burgers vectors (i.e. a/2<111> or a<100> type in general). In order to determine the exact Burgers vector of some loops (i.e. which particular a/2<111> or a<100> variant), contrast experiments at more than one zone axis might be required.
At some foil orientations, some loop variants have **g.b** = 0 for all of the easily-available reflections. This applies in this example for loops with Burgers vector [001]. This fraction of 'missing' loops should be considered in the Burgers vector analysis.

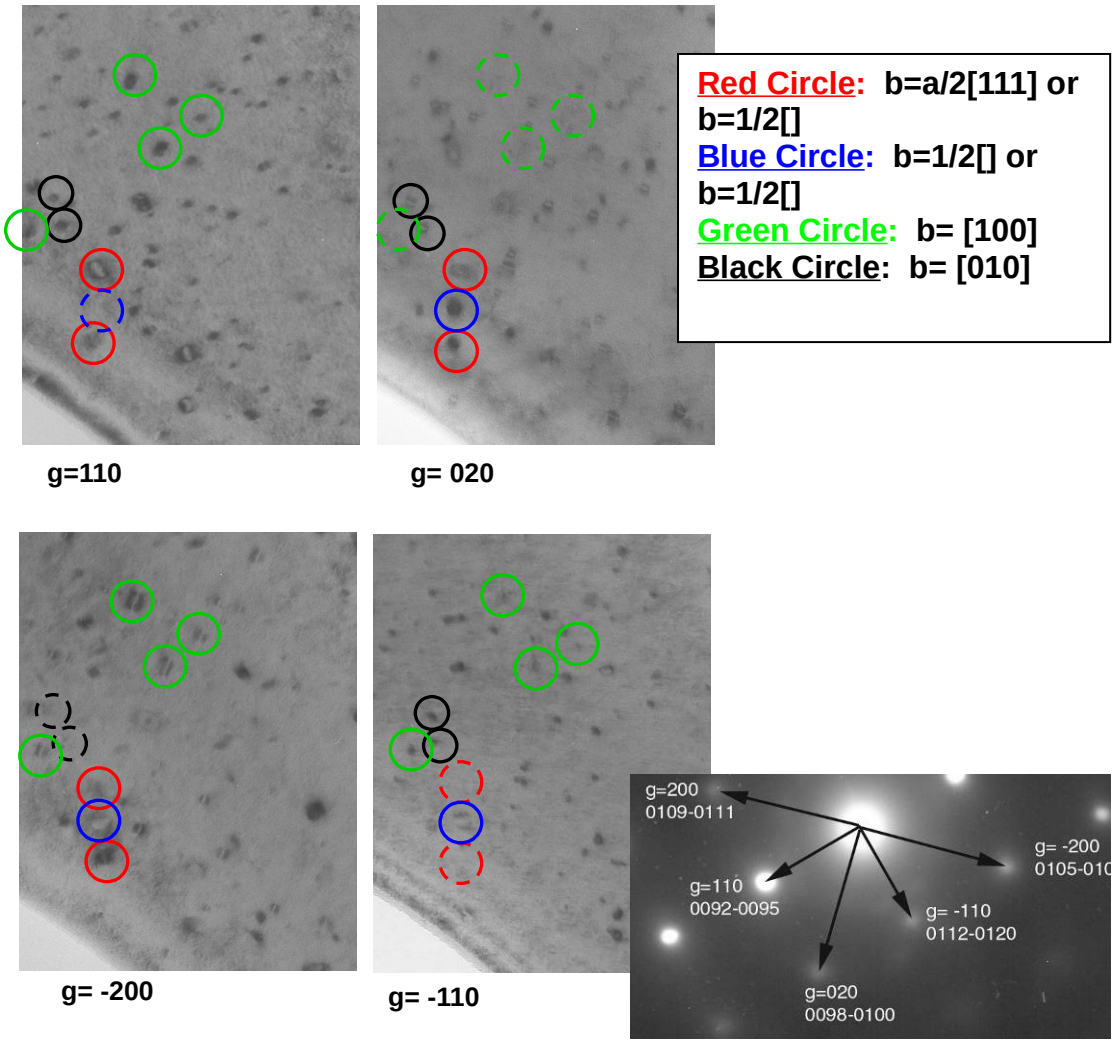

g\b	a/2[111]	a/2[$\bar{1}11$]	a/2[$1\bar{1}1$]	a/2[$11\bar{1}$]	a[100]	a[010]	a[001]
110	**1**	**0**	**0**	**1**	**1**	**1**	**0**
020	**1**	**1**	**1**	**1**	**0**	**2**	**0**
$\bar{2}00$	**1**	**1**	**1**	**1**	**2**	**0**	**0**
$\bar{1}10$	**0**	**1**	**1**	**0**	**1**	**1**	**0**

Fig.3.3 g.b contrast experiment of Fe-8Cr irradiated at 300°C.

3.4. Determination of the vacancy or interstitial nature of loops

The nature (vacancy or interstitial) of the dislocation loops is one of the most difficult things to characterise. There are several ways to determine the nature of dislocation loops, and each has its advantages [55]. The inside-outside technique was used in this work. This technique is potentially the most reliable way to determine the nature of loops; however, its reliability depends on the amount of known information on the loop, in particular its habit plane and Burgers vector. It is often difficult to get all the information required and it is sometimes necessary to make certain assumptions, for example that its inside-outside behaviour is the same as that of an edge loop. The typical procedure of this technique as applied in this work is explained briefly next. The theoretical background and detailed method can be found in [55]. The beam direction was chosen to be ‘pointing downwards’ (i.e. same direction as the electron beam) according to [55] in all the inside-outside contrast experiments. The beam direction was chosen to be ‘pointing upwards’ elsewhere in the thesis.

The definition of the Burgers vector of a loop is shown in **Fig.3.4.1**. The direction of loop normal **n** and the electron beam direction **z** are defined as shown and kept consistent throughout the experiments. The Burgers vector is defined by the closure failure and direction is shown in the figure. Note that **b** points upwards for an edge interstitial loop (**b**. **z** < 0). One could equally define this same Burgers vector with the opposite direction. Therefore it is important to keep a consistent indexing scheme throughout the experiment.

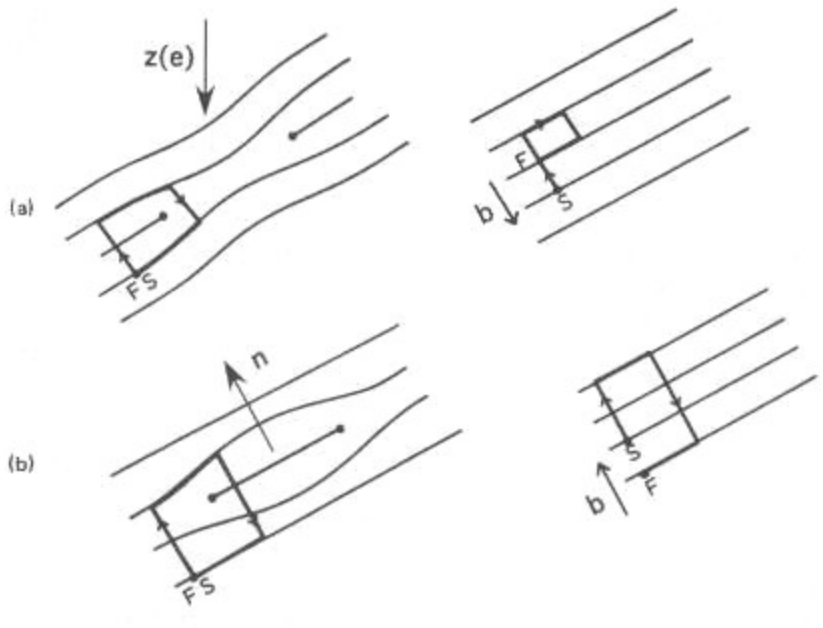

Fig.3.4.1 Definition of Burgers vectors using the Finish-Start/Right-hand (perfect crystal) (FS/RH) convention, for (a) a vacancy loop, and (b) an interstitial lop. The dislocation line direction is taken as clockwise when viewed from above. The Burgers vector is defined by the closure failure b=FS. Definitions of the loop normal n and electron beam direction z are also shown[55].

The principle of the inside-outside technique for an edge dislocation loop is shown in **Fig.3.4.2**. An inclined edge loop of either interstitial and vacancy nature is imaged under bright-field kinematical or dark-field weak-beam conditions. In the kinematical condition, the foil was initially set to two beam condition, and subsequently tilted away slightly from two beam condition while keeping S_g positive. The weak beam condition used usually had g3g to g4g. The direction of the diffraction vector **g** is shown with $S_g > 0$. The sense of lattice rotations caused by the loop strain field is shown in the figure with curved arrows. These regions diffract strongly, and depending on the loop nature, sense of inclination and diffraction vector, the peak of the image lies either inside or outside the projection of the loop, thus generating inside or

outside contrast (as indicated in **Fig.3.4.2**). Formally, inside contrast arises when (**g.b**)S_g<0 and outside when (**g.b**)S_g>0. From this physical principle, one can determine the nature of the loop, by obtaining information on: (1) its inside-outside contrast (with ± **g** experiments); (2) its Burgers vector (**g.b** experiment); and (3) its habit plane or sense of inclination.

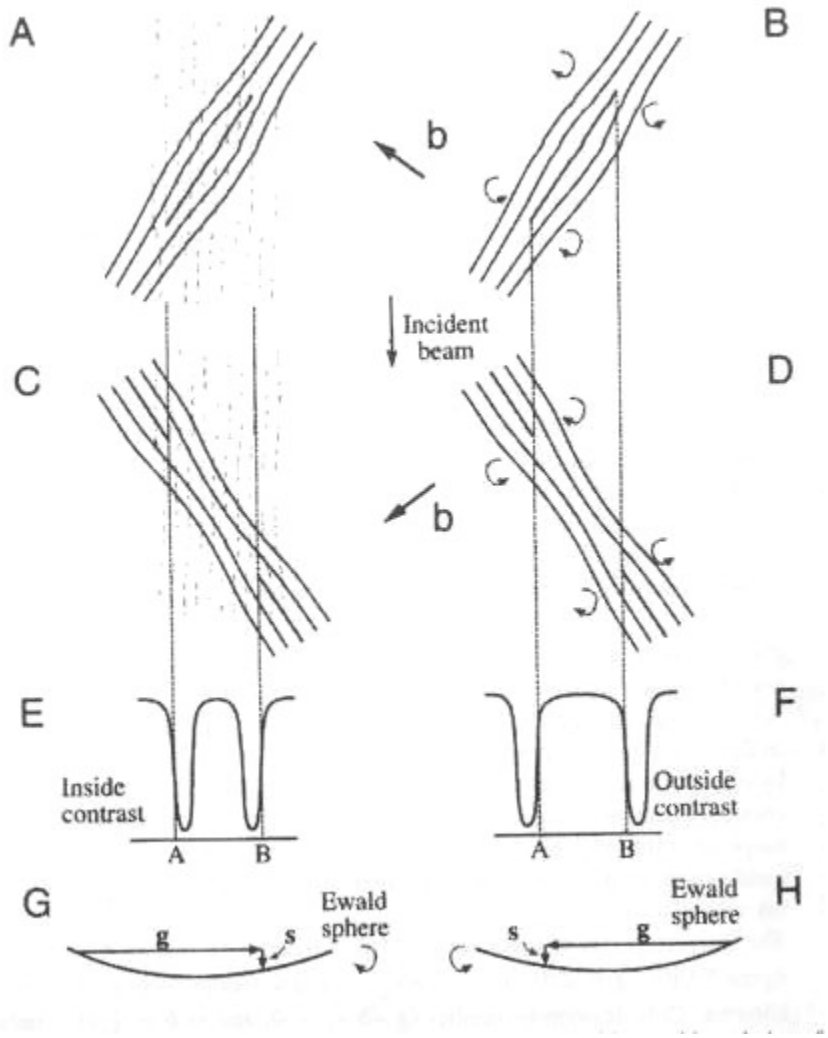

Fig.3.4.2 illustration of inside-outside technique for an edge dislocation loop. An inclined interstitial loop is shown in A with the sense of plane rotations indicated in B. The same is shown for a oppositely-inclined vacancy loop in C and D. The position of the image contrast with respect to the projection of the loop dislocations is shown in E and F for the diffraction conditions shown in G and H, respectively. The g in G and H are opposite but in both G and H s_g is positive. Inside contrast results when clockwise rotation of the diffracting planes brings them into the Bragg condition G. Outside contrast results for the counter clockwise case H. Formally, inside contrast arises when $(g.b)s_g < 0$, while outside contrast arises when $(g.b)s_g > 0$ [55].

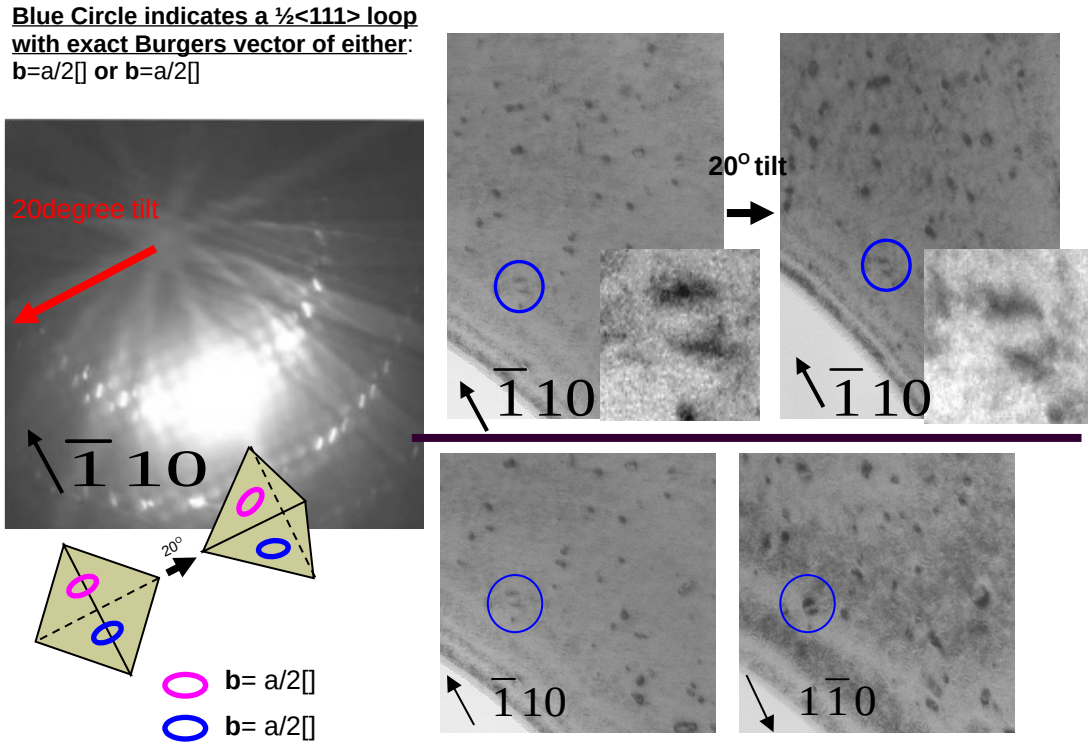

Fig.3.4.3 Nature analysis of Fe-8Cr using inside-outside technique near [001] zone axis. The two possible Burgers vectors of the circled loop was determined using g.b analysis. From the sense of rotation after the tilting, the loop is determined to be a/2[$\bar{1}11$]; outside contrast in g=$\bar{1}10$ implies the loop is interstitial. Note that the diffraction pattern showing on the left showing Kikuchi map was taken at g=110, therefore the diffraction condition does not represent the condition at which the pictures were taken.

Fig.3.4.3 is an example of the inside-outside technique carried out on the same specimen (Fe-8Cr irradiated at 300°C). The bottom two micrographs illustrate a pair of images with the same but opposite diffraction vectors, taken at the same location on the specimen. The micrograph on the left shows 'outside contrast'. Because of the 4-fold symmetry of the system, there is more than one way of indexing the directions. It was chosen in this work to label the diffraction vector on the left micrograph to be **g**=$\bar{1}10$, and thus we have **g**=$\bar{1}10$ with 'outside contrast'. The same indexing scheme was kept for the rest of the experiment.

The condition for the generation of outside contrast is (**g.b**)s_g > 0, where s_g is positive (because the image was taken under bright-field kinematical conditions.) Therefore, we have

$$\mathbf{b}.(\bar{1}\,10)>0. \qquad \textbf{Equ.3.4}$$

It is clear that in order to determine the loop nature, the exact Burgers vector has to be obtained. In this particular case, the dislocation loop illustrated in the blue circle has possible Burgers vectors of ±a/2[$\bar{1}\,11$] or ±a/2[$1\,\bar{1}\,1$] from the previous **g.b** experiment. However, the two possible directions of Burgers vectors would give opposite results in the nature determination. Therefore the loop was imaged with a 20^o tilt towards the [110] direction. The tilting experiment showed that the habit plane of the loop is more likely to lie close to ($\bar{1}\,11$) rather than ($1\,\bar{1}\,1$), as shown in **Fig.3.4.3**. If the loop were of edge or close-to-edge type, which is expected for bulk radiation damage of this size, then the ($\bar{1}\,11$) habit plane would indicate that the loop had **b**=±a/2[$\bar{1}\,11$] rather than ±a/2[$1\,\bar{1}\,1$]. Because we have **b**.($\bar{1}\,10$)>0 from **Equ.3.4**, this implies that **b**= +a/2[$\bar{1}\,11$]. From the choice of definition of **b** in Fig.3.4.1, the loop has interstitial nature.

Chapter 4: Results on radiation damage in α-iron

In this chapter work on the characterisation of ion-irradiated α-iron will be presented. The main feature seen in all specimens was a moderately high density of resolvable dislocation loops, qualitatively similar to the microstructures seen in neutron-irradiated Fe and Fe-Cr alloys [67, 77]. The number densities, sizes and Burgers vectors of loops were characterised and results were compared between specimens under different irradiation conditions. A nature analysis of loops in Fe was attempted but it was not successful in these bulk irradiations due to the difficulties of both specimen preparation and microscopy with ferritic specimens. Parallel thin-foil experiments showed that in specimens irradiated at 300^{o}C and 500^{o}C, all large loops were of interstitial type [63]. It will be shown in the next chapter that loops in bulk Fe-Cr alloys, irradiated under the same conditions as Fe, are also of interstitial nature.

As part of all the TEM experiments described in this chapter, the existence of voids was carefully looked for by the defocusing method. However no voids were found in any specimens.

4.1 Radiation damage microstructures

Fig.4.1.1 and Fig.4.1.2 show two pairs of micrographs illustrating typical damage structures in Fe specimens irradiated at 300^{o}C and 500^{o}C. Fig.4.1.3 show a series of micrographs of Fe irradiated at various

conditions. Damage in all cases took the form of dislocation loops with sizes ranging up to about one hundred nanometres.

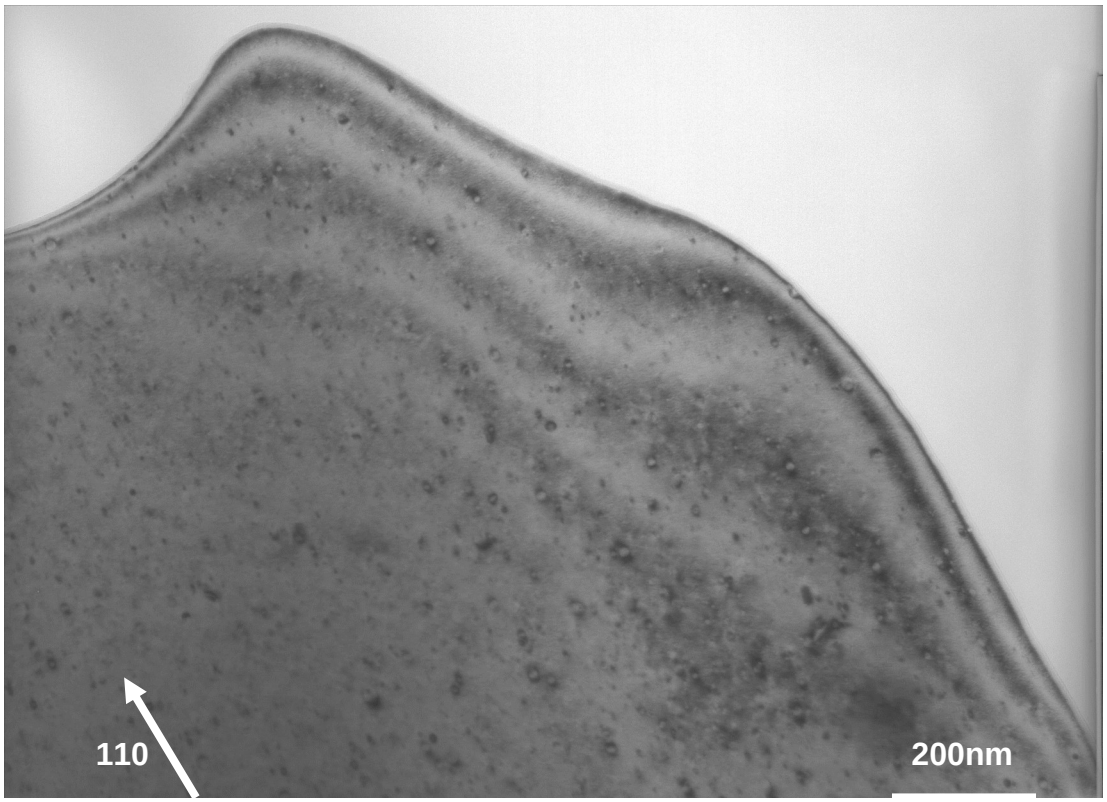

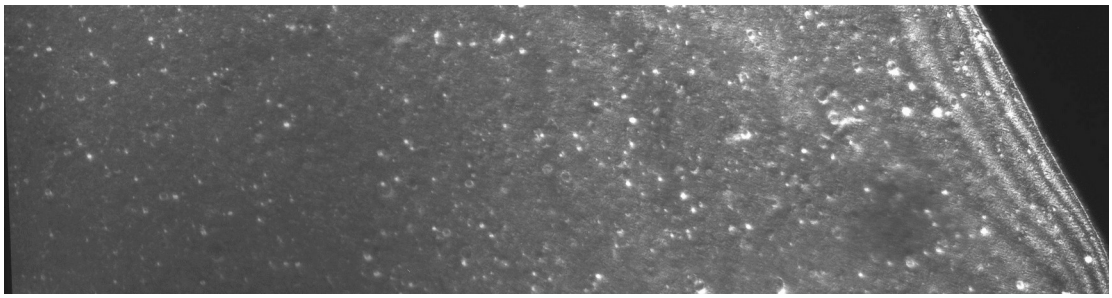

Fig.4.1.1 TEM micrographs of Fe specimen irradiated at 300°C to a dose of $1x10^{19}$ ions m^{-2} (2.5dpa). Both bright field kinematical (upper) and dark field weak beam 'g2g' (lower) picture were taken near the [001] zone axis with g=110.

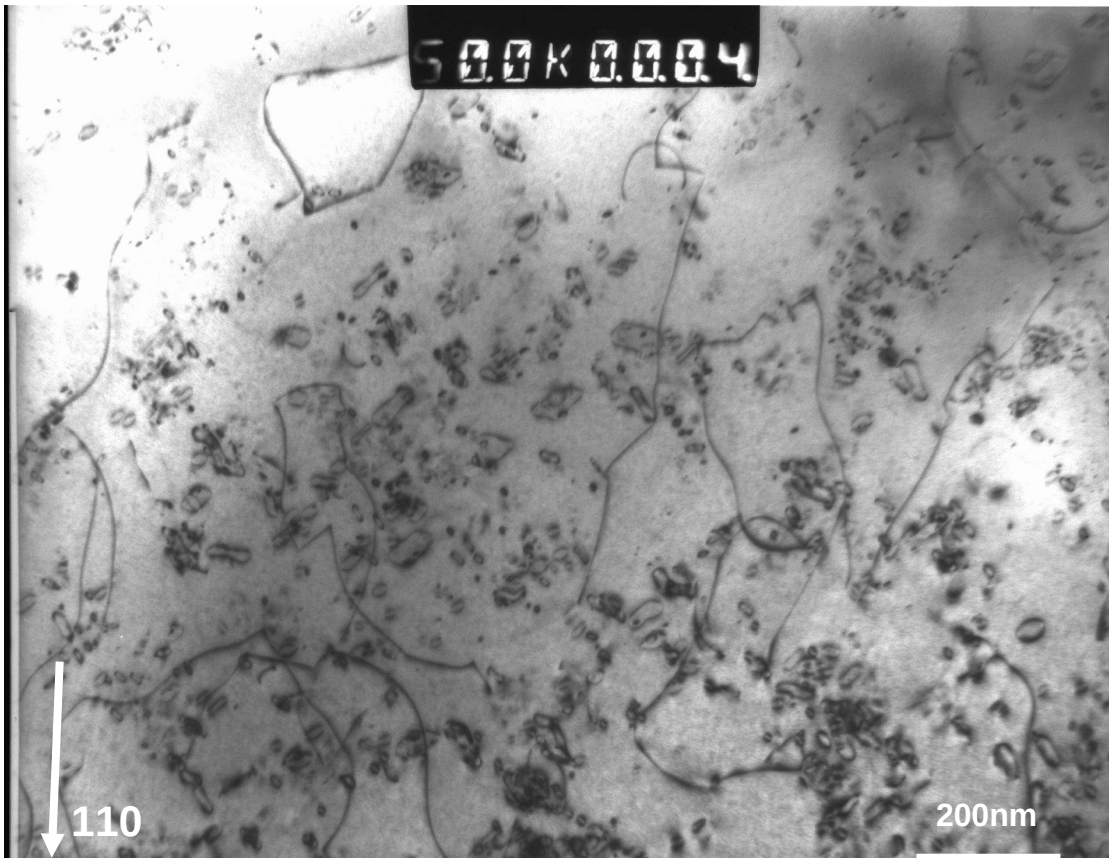
50.0K 0.0.0.4
110
200nm

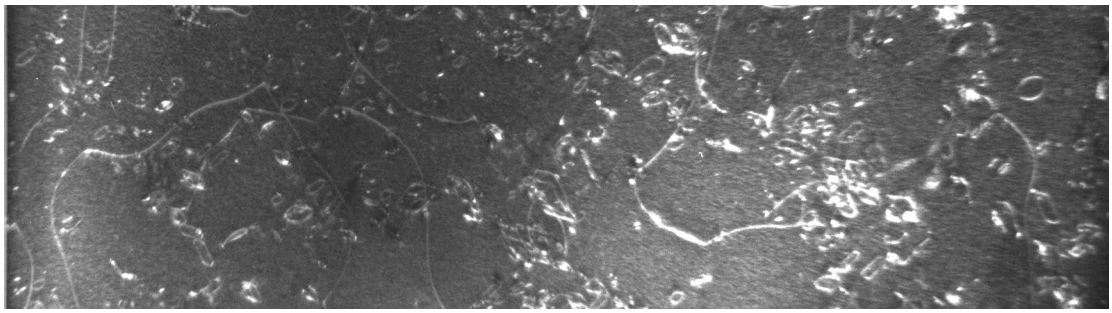

Fig.4.1.2 TEM micrographs of Fe specimen irradiated at 500°C to a dose of $3x10^{19}$ ions m^{-2} (7dpa). Both bright field kinematical (upper) and dark field weak beam 'g3g' (lower) picture were taken near the [111] zone axis with g=110.

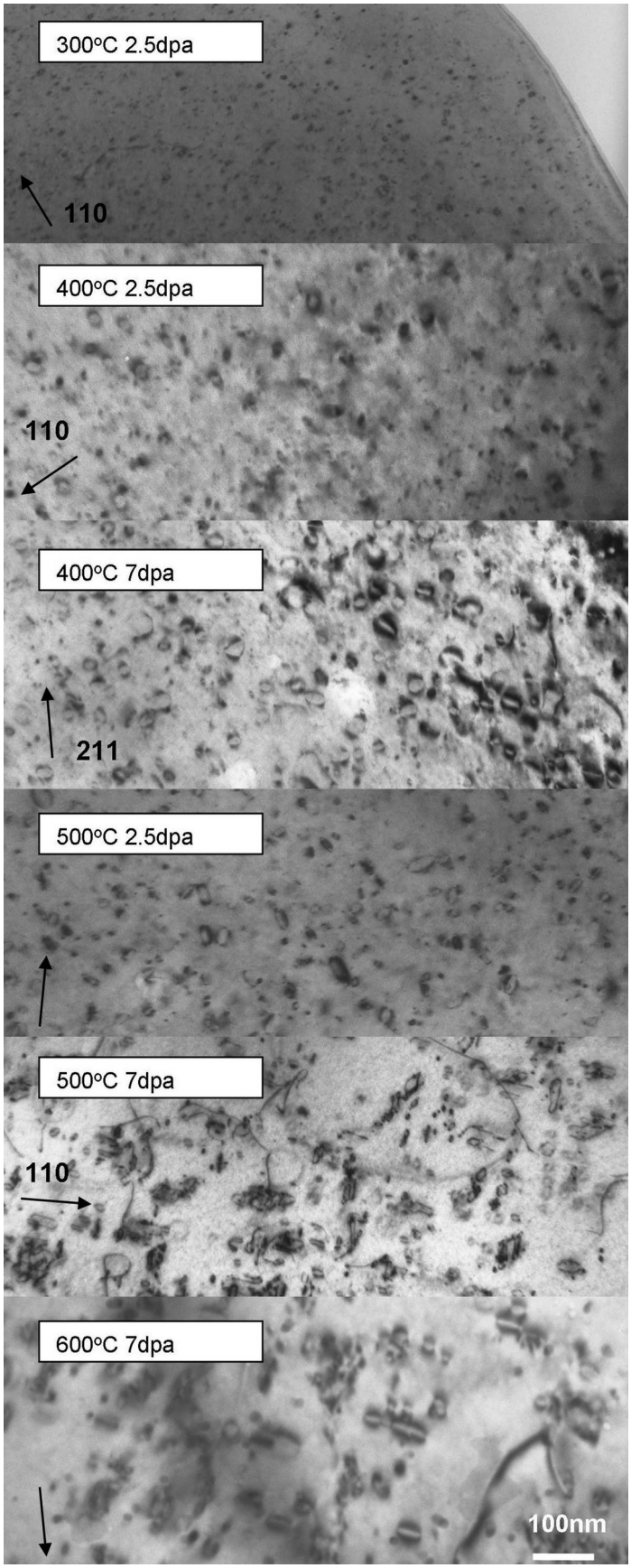

Fig.4.1.3 Micrographs of pure Fe specimen irradiated at different conditions.

At 300°C, the damage structures were on a much finer scale compared to those seen at higher temperatures, and the number density of loops was higher. The dislocation loops in specimens irradiated at 400°C and 500°C to $1x10^{19}$ ions m^{-2} (2.5dpa) were similar in shapes and morphologies. However at 500°C, in the specimen irradiated to $3x10^{19}$ ions m^{-2} (7dpa), the dislocation loops started to associate with each other and more complex loop shapes were observed. In addition to dislocation loops, specimens irradiated under this condition also contained networks of line dislocations, which were absent in specimens irradiated at lower temperatures. It was observed that some dislocation lines had circular shapes similar to dislocation loops, but at a much larger scale (>200nm). Similar damage structures were observed in specimens irradiated at 600°C to 7dpa. The size distributions and number densities of the loops were measured, and are described next.

4.2 Dislocation loop size characterisation

The loop image size distributions were measured for Fe specimens at various irradiation temperatures (300– 600°C) and doses (2.5-7dpa). In this thesis, the image size of a dislocation loop with circular contrast is defined to be the diameter of its contrast. Image size of loop with ‘double arc’ or ‘elliptical’ contrast is defined to be the major axis of its contrast.

Determination of size for individual small dislocation loops (<10nm) is difficult. The relationship between the image and actual loop size depends on the foil thickness, the depth of the loop in the foil and the exact diffraction conditions and. In this thesis, a large population of dislocation loops (>100) with different

diffraction conditions (including +/-g, BF/DF) were measured to maximise the accuracy of the average loop size characterisation.

The distributions are presented as histograms showing the percentage of the loop population with different loop image sizes. Each bin represents a 10nm range in size.

For loops less than 10nm, the image size is less representative of the actual loop size, because the difference between the loop image size and true loop size can be affected by foil thickness, depth of the loop and the diffraction conditions. In addition, dislocation loops smaller than 2nm are usually invisible. Therefore, an average loop size of 6nm was estimated for all loops with image sizes below 10nm. The sampling population was about 150-250 loops in each specimen and the statistical error was taken into account.

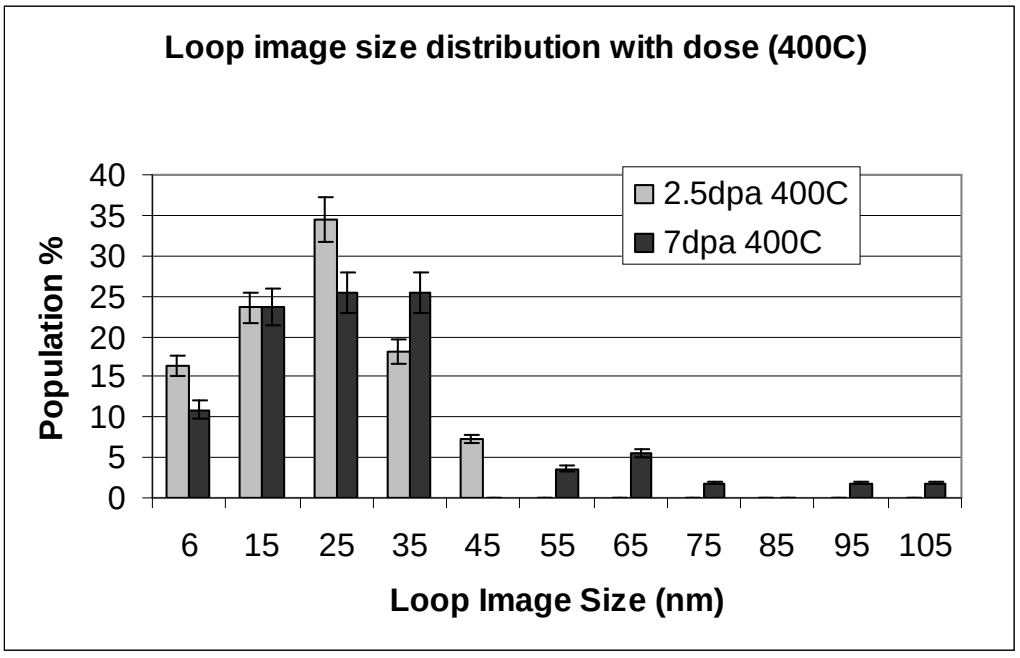

Fig.4.2.1 Histogram showing loop image size distributions of Fe irradiated at 400°C with different doses.

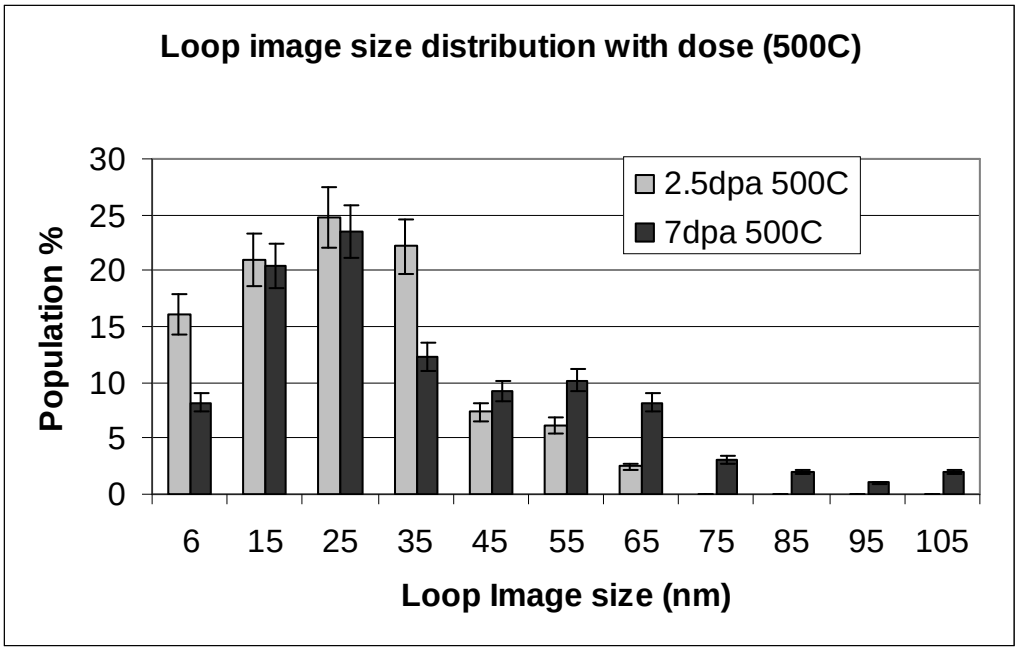

Fig.4.2.2 Histogram showing loop image size distributions of Fe irradiated at 500°C with different doses.

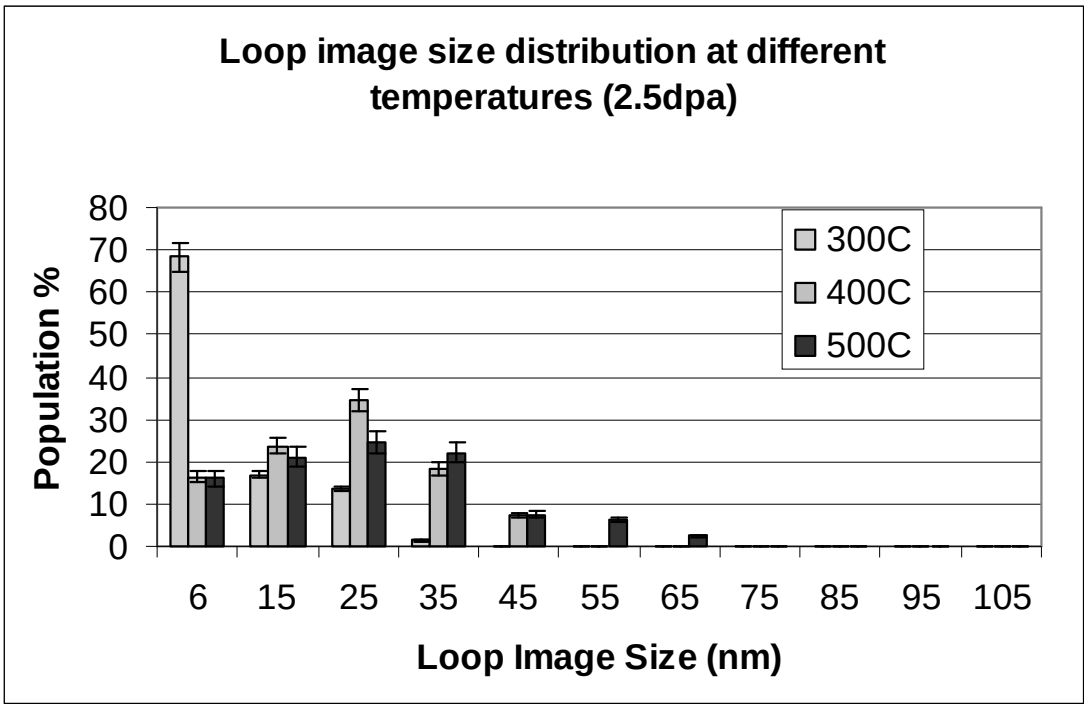

Fig.4.2.3 Histogram showing loop image size distributions of Fe irradiated at 2.5dpa at different irradiating temperatures.

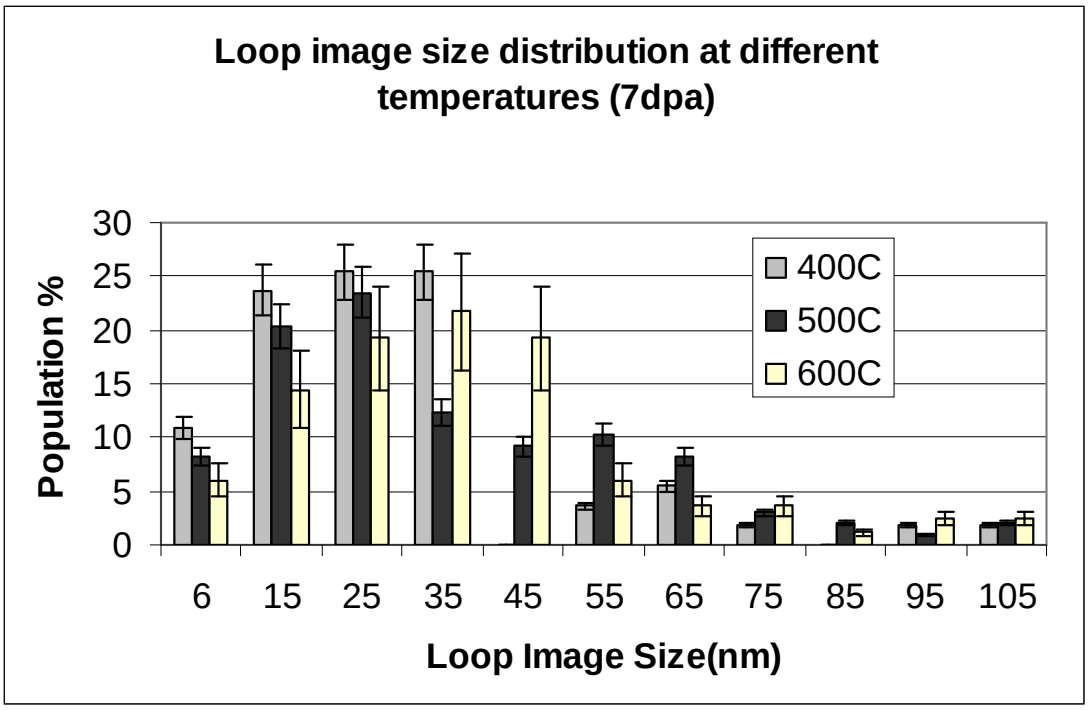

Fig.4.2.4 Histogram showing loop image size distributions of Fe irradiated at 7dpa at different irradiating temperatures.

Fig.4.2.1 and **Fig.4.2.2** show loop image size distributions at the same irradiation temperature for different irradiation doses. At both 400^{o}C and 500^{o}C, an increase in dose from 2.5 to 7 dpa caused a shift to larger sizes in the distributions, and the distributions became broader by about a factor of two. The average loop size increased from 21.8±2.7 nm to 29.4±2.6 nm at 400^{o}C and from 25.4±2.3 nm to 35.4±1.8 nm at 500^{o}C.

.

The effects of irradiation temperatures on loop size distributions are shown in **Fig.4.2.3** and **Fig.4.2.4**. Higher irradiation temperatures resulted in larger loops. The average loop size at 7 dpa increased from 29.4±2.6 nm at 400^{o}C to 35.4±1.8 nm at 500^{o}C to 37.8±2.5 nm at 600^{o}C. However, the irradiation

temperature had only a small effect on the spread of the distribution comparing to the effect of dose.

The changes in average loop sizes with temperature and dose are shown graphically in **Fig.4.2.5**. It is clear that loop sizes increased with both irradiation temperature and dose.

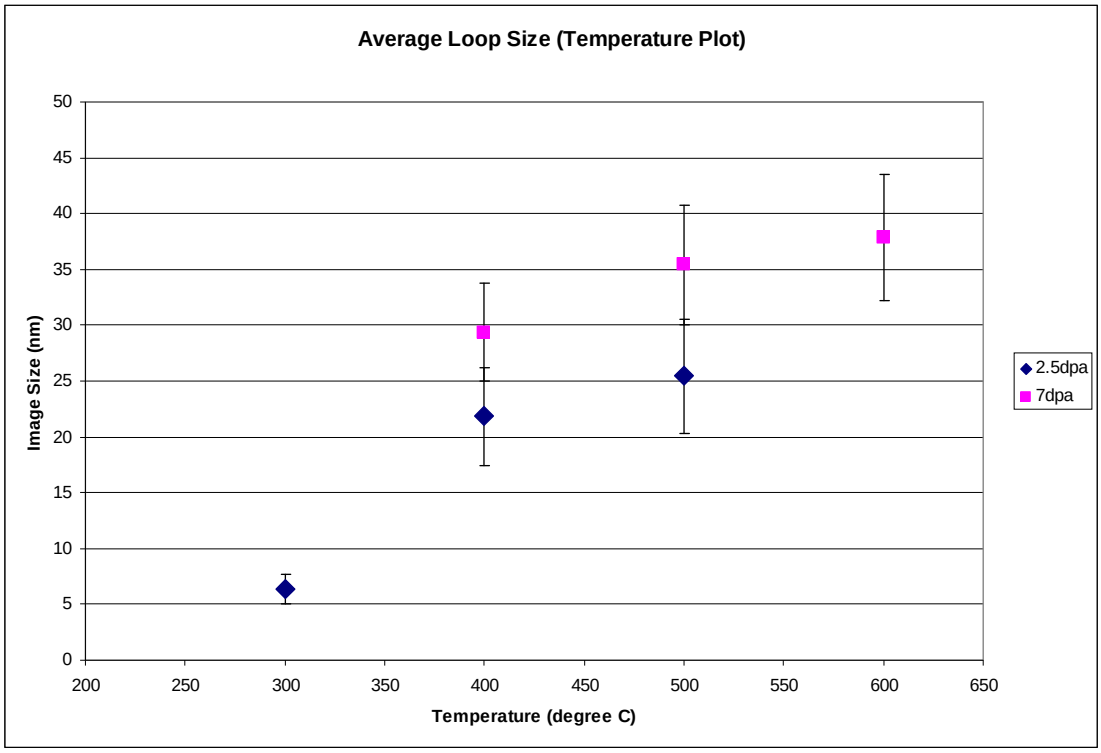

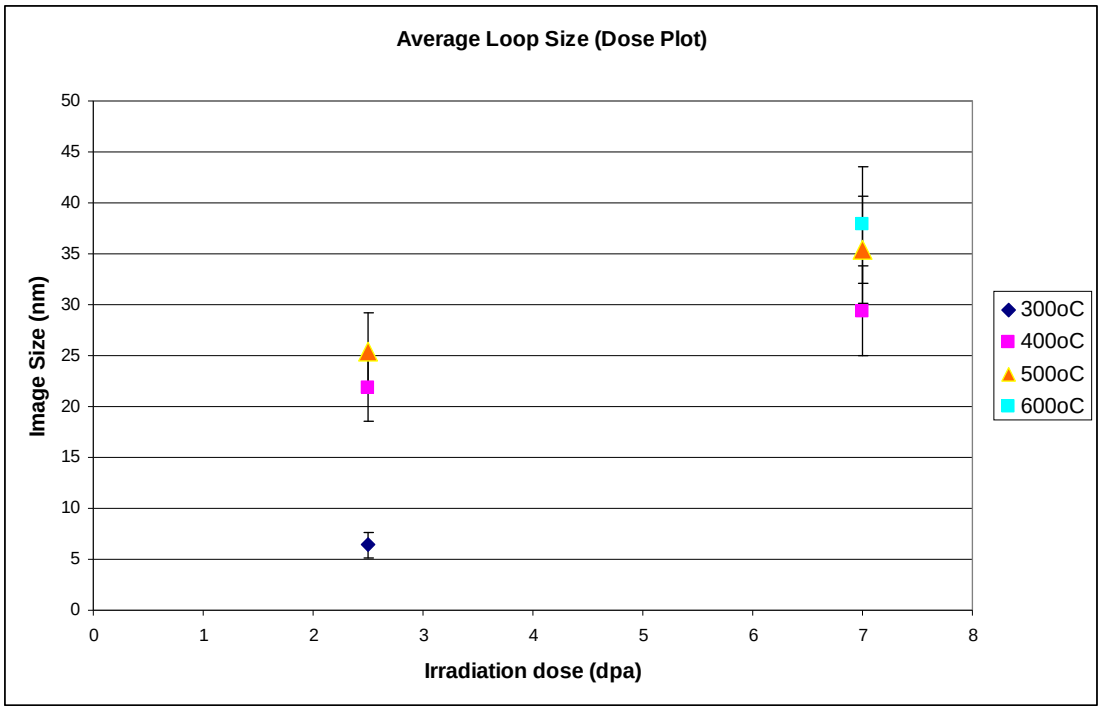

Fig.4.2.5 Plots of average loop image size as a function of: (a) temperature; (b) dose.

4.3. Loop number densities

Measurement of volume number densities requires a knowledge of the foil thickness. EELS and convergent beam techniques were both used in this project for measuring foil thickness. The detailed methodologies were explained in chapter 3.1.

In pure Fe, the EELS experiment was carried out with Dr. Vanessa de Castro on a specimen irradiated at 600^{o}C (see **Fig.4.3.1**). Four regions of the specimen were analysed and an average loop number density was calculated based on the four measurements. The average loop number density was

(1.79 ± 0.38) x10^{21} loops/m^2, where the error comes from a combination of statistical error and systematic error produced by the EELS method [103].

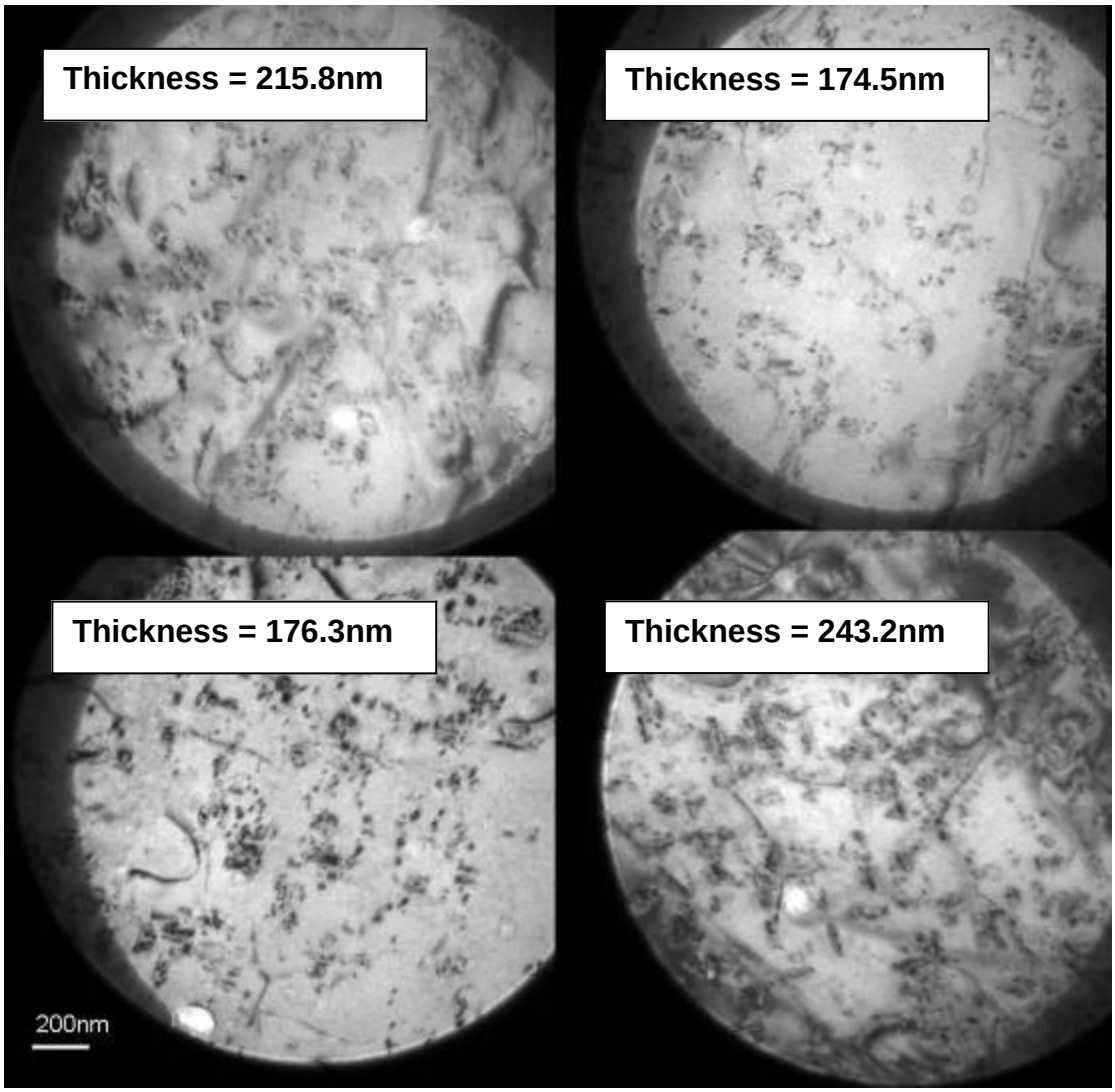

Fig.4.3.1 Micrographs showing areas where EELS thickness measurements were carried out.

Unfortunately, other experiments with pure Fe specimens were carried out without thickness measurements due to instrument unavailability. For these specimens the foil thickness was estimated with the aid of thickness fringes and errors were included for the uncertainty in these estimations.

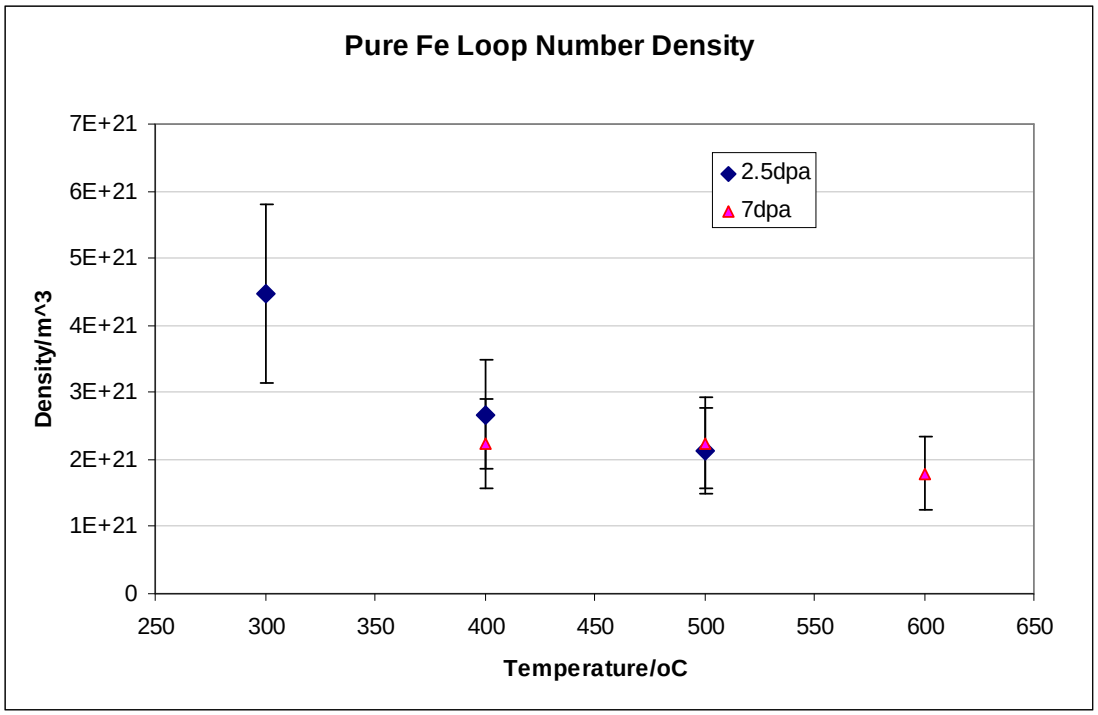

Fig.4.3.2 Dislocation loop number density as a function of irradiating temperatures.

Fig.4.3.2 shows the loop number densities at different irradiation conditions. At irradiation temperatures ≥ 400°C the loop number densities were similar and showed no obvious dependence on dose. At 300°C the number density was about a factor of two higher than at other irradiation conditions.

4.4. Loop Burgers vector characterisation

Two types of Burgers vectors, i.e. a/2<111> and a<100> occur in bcc Fe as described in chapter 1.4.3. The Burgers vectors of the loops were determined using the standard **g.b** = 0 invisibility criterion.

4.4.1 Burgers vector characterisation on 300°C/2.5dpa specimens

Fig.4.4.1 shows a series of micrographs taken near the [001] zone axis in a Fe specimen irradiated at 300°C to a dose of 2.5dpa. The |**g.b**| table shows that an [001] foil orientation is favourable for **g.b** analysis. It is possible easily to obtain the diffraction vectors **g** = 200 and 020 as well as **g** = $1\bar{1}0$ and 110. From images taken using the first of these pairs of diffraction vectors one can immediately distinguish a/2<111> and a<100> loops. All loops of type a/2<111> stay in contrast in both **g** = 200 and 020, while the two types of a<100> loops (i.e. a[100] and a[010]) are out of contrast in one of the two **g**-vectors. Similar considerations apply to the second pair of reflections, where in this case both sets of edge-on a<100> loops will be in contrast in both **g** = $1\bar{1}0$ and 110, whilst loops with **b** = a/2<111> will be out of contrast in one of the pair. In the experiment illustrated in **Fig.4.4.1**, images were obtained using all four reflections. Both +**g** and –**g** images were obtained as well as BF and WBDF images.

It can be seen in the micrographs shown that most large loops remain visible in both 200 and 020, whereas the same loops appear on only one of the 110-type micrographs. In addition, the contrast appearance is consistent in micrographs taken in ±**g** and under the different diffraction conditions. By obtaining the Burgers vectors for about 200 loops in two different specimens, we conclude that 92 ± 6% of the loops have Burgers vector of type a/2<111>.

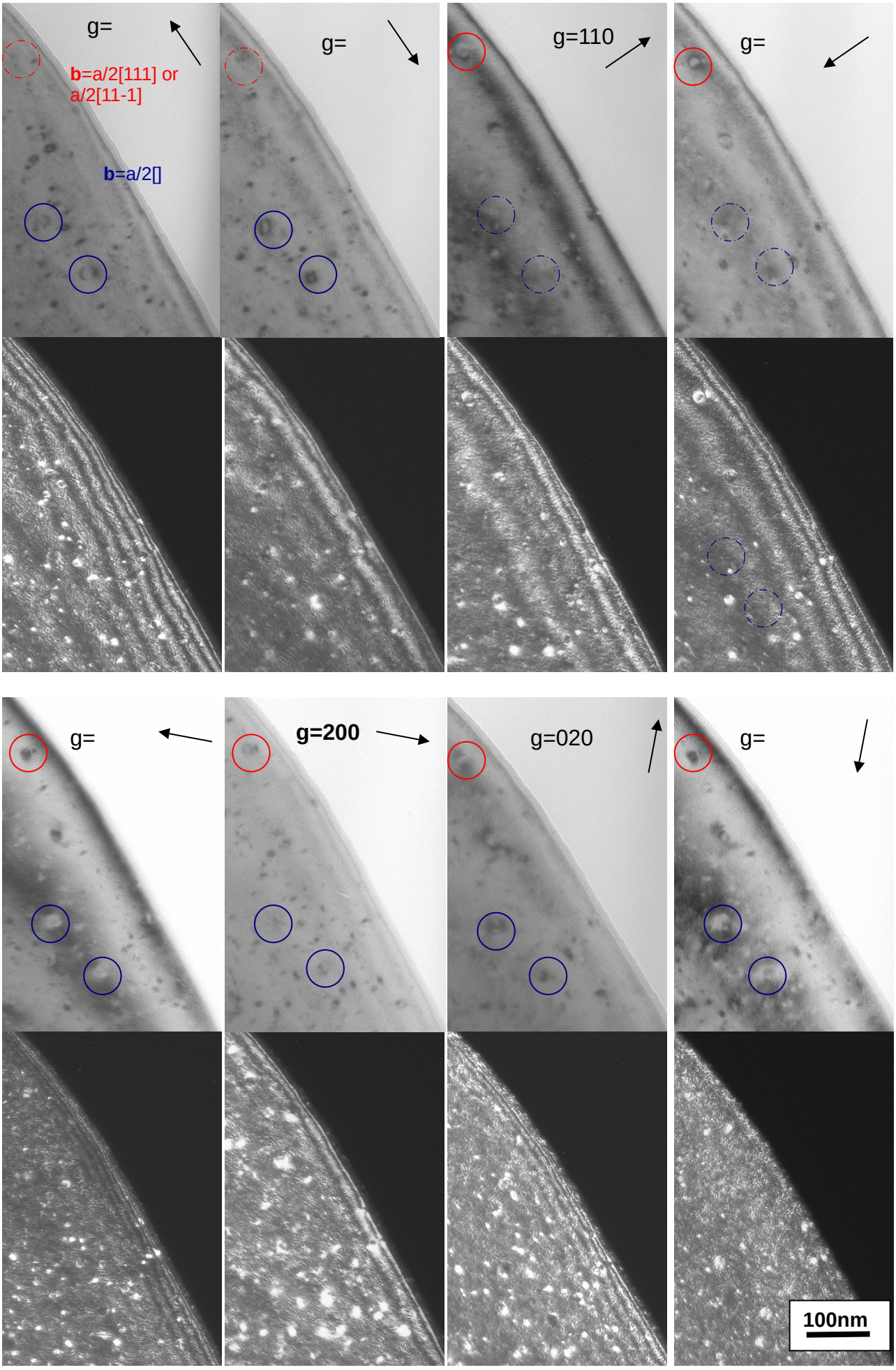

Fig.4.4.1 (Micrographs): g.b contrast experiments near zone axis [001]; the red circles mark loops

with b=a/2[111] or a/2[$1\,1\,\bar{1}$] while the blue circles mark loops b=a/2[$\bar{1}\,11$].

g\b	a/2[111]	a/2[$\bar{1}\,11$]	a/2[$1\,\bar{1}\,1$]	a/2[$11\,\bar{1}$]	a[100]	a[010]	a[001]
$\bar{1}\,10$	**0**	**1**	**1**	**0**	**1**	**1**	**0**
110	**1**	**0**	**0**	**1**	**1**	**1**	**0**
$\bar{2}00$	**1**	**1**	**1**	**1**	**2**	**0**	**0**
020	**1**	**1**	**1**	**1**	**0**	**2**	**0**

Fig.4.4.1 continued (Table): g.b table for [001].

4.4.2 Burgers vector characterisation on 400°C/7dpa specimens

Fig.4.4.2 shows a selected **g.b** analysis of a Fe specimen irradiated at 400°C to 7 dpa. The foil shown in the figure had a foil normal close to [011]. At this foil orientation, four reflections ($0\bar{1}1$, $\bar{2}00$, $\bar{2}1\bar{1}$ and $\mathbf{2\bar{1}\bar{1}}$) are accessible. However, these four reflections are not sufficient to differentiate the Burgers vector type a[100], a/2[111] and a/2[$\bar{1}11$] because loops with all three burgers vector will only go out of contrast (g.b=0) at g= $0\bar{1}1$. In order to complete the analysis, the specimen was first tilted to the [111] orientation and imaged under g=$1\bar{1}0$. This orientation effectively puts all a/2[111] loops out of contrast and therefore differentiate a[100] from ½[111]. The specimen was further tilted to **z** =[113] and g= $\bar{1}\bar{2}1$ and $\bar{2}\bar{1}1$ were reached. The addition of $\bar{1}\bar{2}1$ reflection differentiate loops with **b**= a[100] from **b**=a/2[$\bar{1}11$] (as shown in the g.b table) and allowed a complete Burgers vector analysis. Among the one hundred loops analysed, 75 ± 7% of the loops had **b**= a/2<111> with the rest being a<100>. All the variants were found present in similar numbers. It was also observed that the a/2<111> loops were significantly larger in size than the a<100> loops.

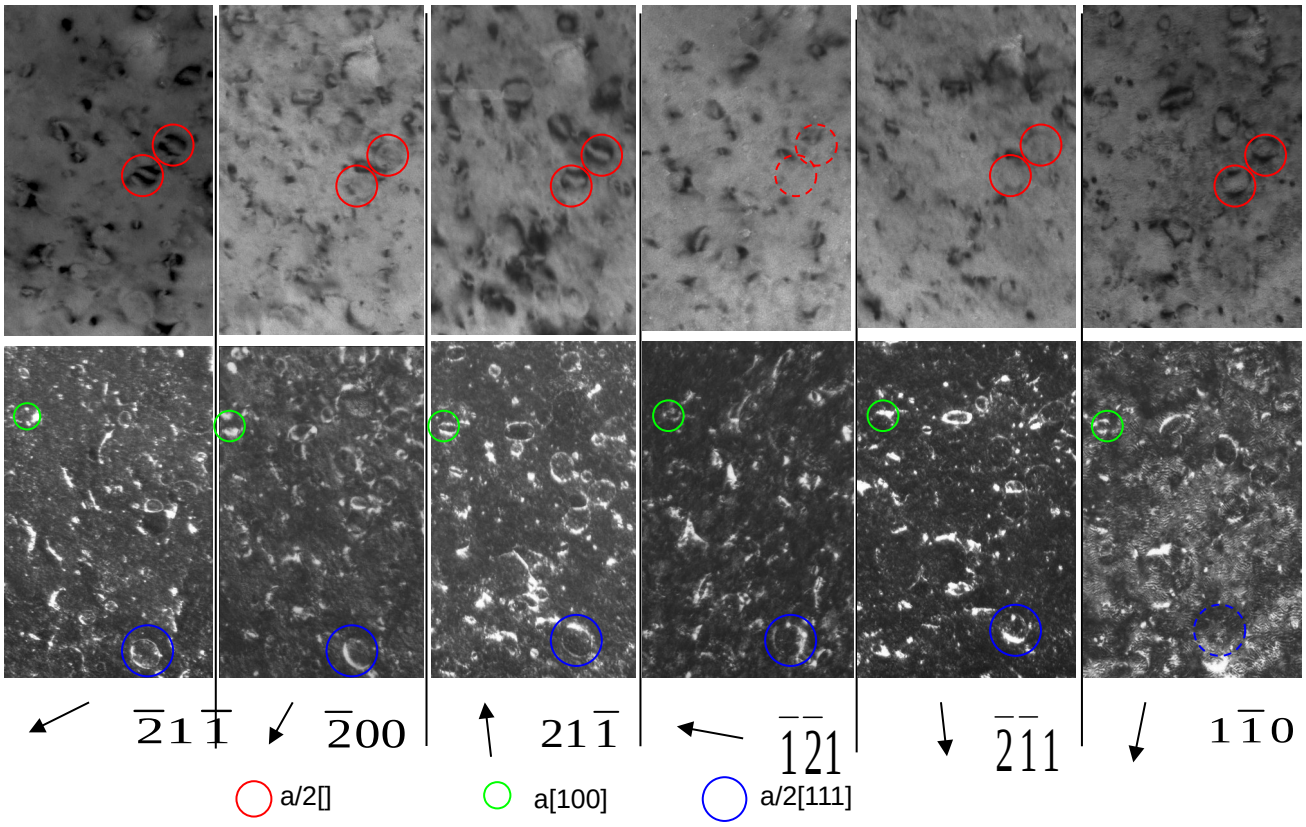

Zone axis	g\b	a[100]	a[010]	a[001]	a/2[111]	a/2[$\bar{1}11$]	a/2[$1\bar{1}1$]	a/2[$11\bar{1}$]
	$\bar{2}1\bar{1}$	**2**	1	1	**1**	**1**	2	0
[011]	$\bar{2}00$	**2**	0	0	**1**	**1**	1	1
	$21\bar{1}$	**2**	1	1	**1**	**1**	0	2
[113]	$\bar{1}\bar{2}1$	**1**	2	1	**1**	**0**	1	2
	$\bar{2}\bar{1}1$	**2**	1	1	**1**	**1**	0	2
[111]	$1\bar{1}0$	**1**	1	0	**0**	**1**	1	0

Fig.4.4.2 Micrographs: g.b contrast experiments near zone axis [011], [113] and [111]. Several loops were circled with respect to their Burgers vectors.Only a sufficient selection of micrographs was shown here. (Table): g.b table for a selection of g vectors near [011], [113] and [111].

4.4.3 Burgers vector characterisation on 500°C/7dpa specimens

Fig.4.4.3 shows three micrographs of a Fe specimen irradiated at 500°C to 7dpa. The micrographs were taken with 3 different diffraction vectors close to the [001] zone axis. These conditions are similar to the case shown in **Fig.4.4.1**. It was found that 95 ± 7% of the two hundred resolvable loops have Burgers vectors of type a<100>. The microstructures found in specimens under such irradiation conditions are noticeably different from the case of the lower temperatures. The dislocation loops were much bigger and more complex in structure. A large population of line dislocations was also observed throughout the specimen. This structure was observed in multiple specimens under the same irradiation condition. Specimens which had undergone the same heat treatment but were not irradiated were also looked at and no dislocations of such density were found. Therefore it is believed that these line dislocations structures are radiation induced. The **g.b** analysis reveals that the line dislocations have a/2<111> Burgers vectors.

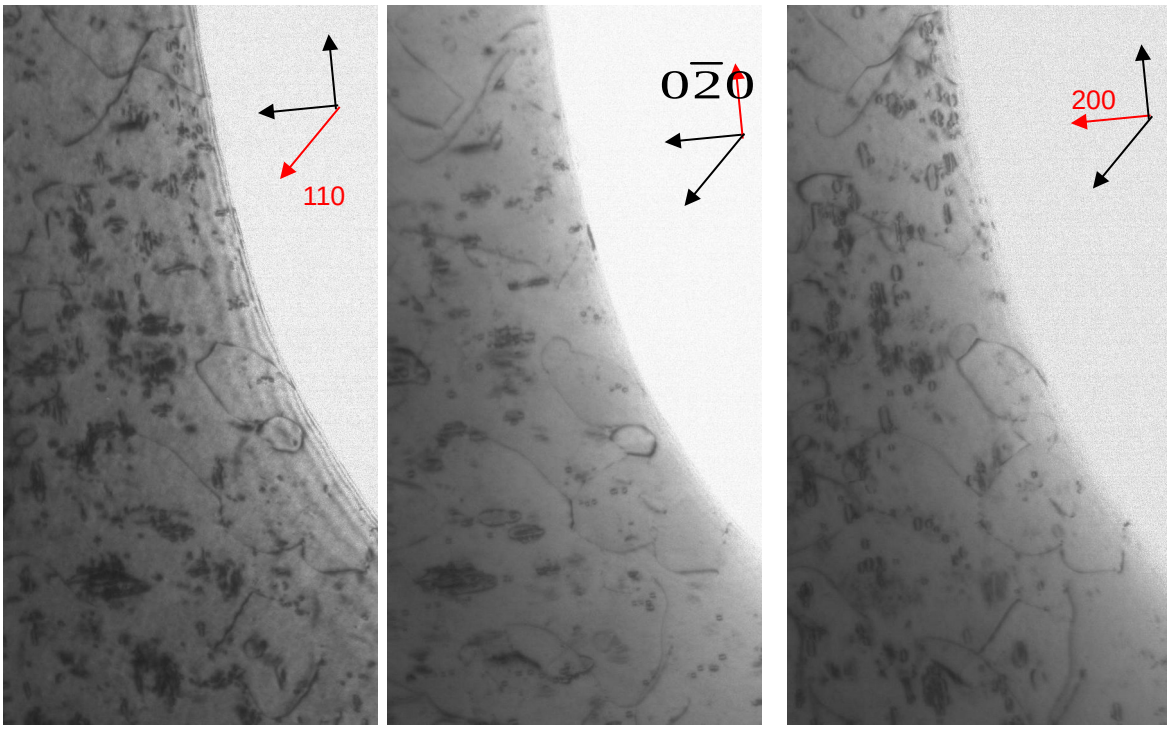

Fig.4.4.3 Micrographs showing g.b contrast experiments near zone axis [001] at irradiation temperature of 500°C.

The proportion of a/2<111> loops as a function of irradiation temperature is summarised below in **Fig.4.4.4**.

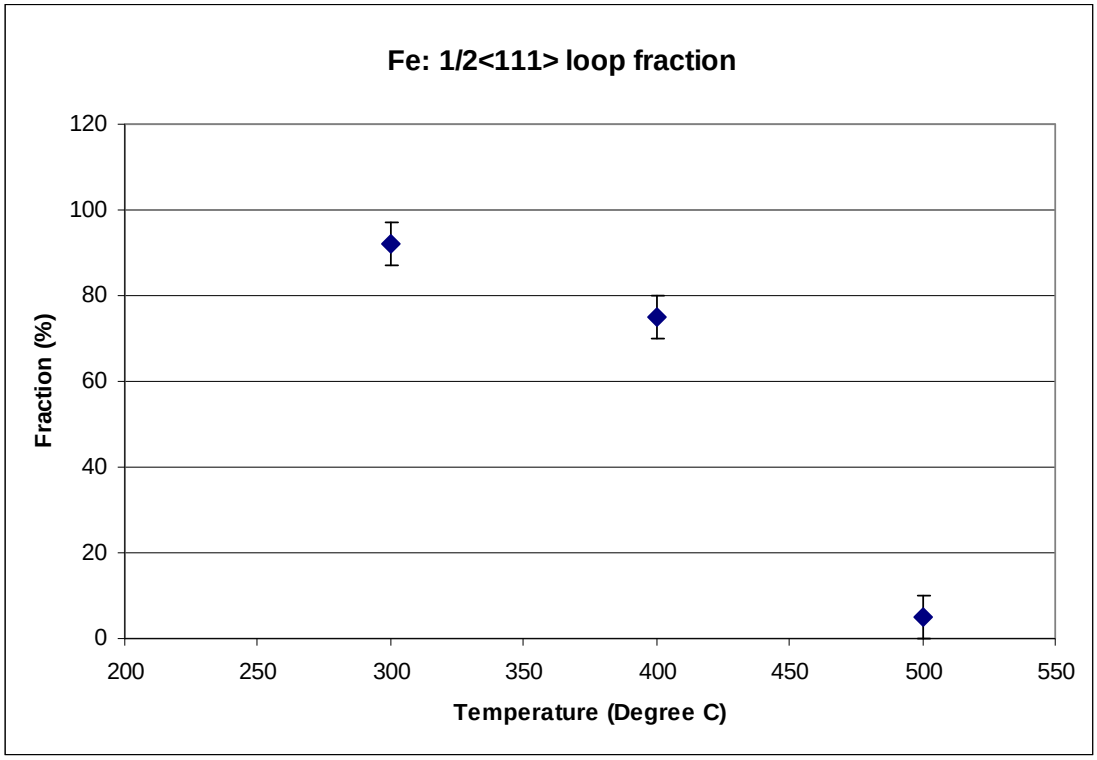

Fig.4.4.4 Fraction of a/2<111> loops at different irradiation temperatures

4.5. Interstitial point defect densities

Assuming that all loops are of interstitial type, an estimation of the interstitial point defect density could be made using loop number densities and average loop sizes. It was estimated that a<100> edge loop of diameter 2.5nm contains 121 interstitial point defects. The same number of point defects will be contained by an a/2<111> loop of diameter 2.7nm [71]. Assuming that the number of point defects contained in a loop is proportional to the square of the loop size, the numbers of point defects were estimated and plotted in **Fig.4.5**. Discussion of this plot is carried out in Chapter 6.

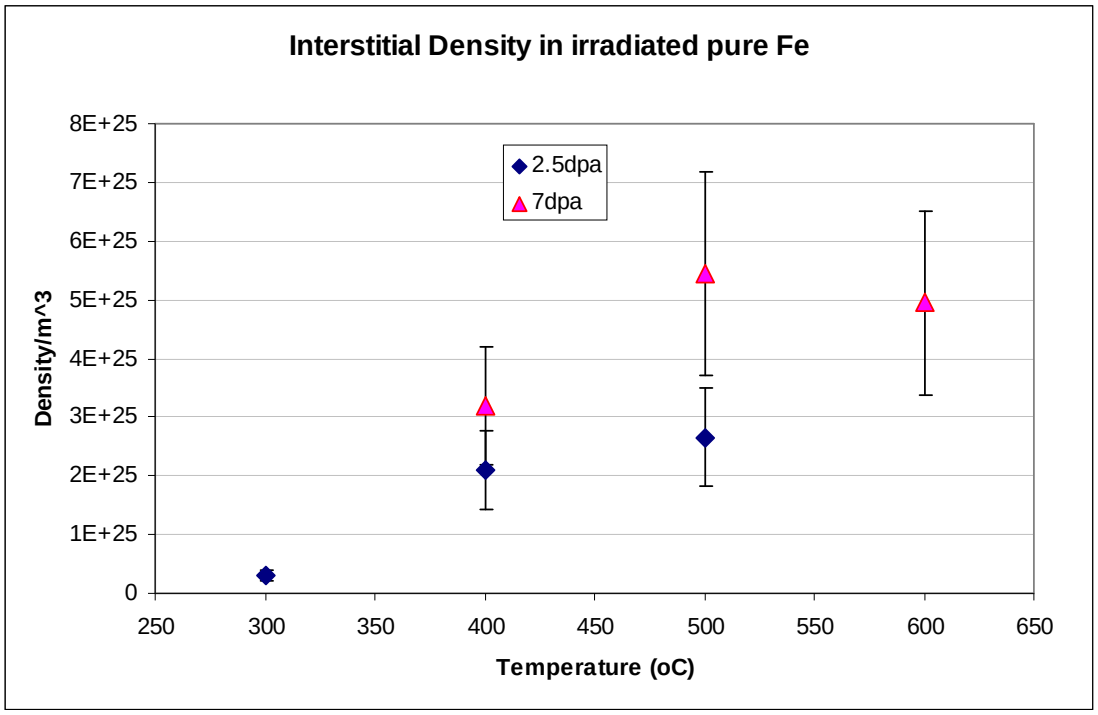

Fig.4.5 Interstitial density as a function of irradiation temperature.

4.6. Comments on experimental uncertainty

The error quoted for most experimental results are from the statistical error. In addition to those random errors, there are systematic errors which arise from the experimental methodology. This section will discuss some of the uncertainties in the experiments.

The loop size and number density results could be affected by the quality of the TEM foil. This is because the contrast of smaller dislocation loops (e.g. loops less than 10nm) could be lost when specimens have a poor surface quality, produced for example by surface oxidation. Such effects will be less important at higher irradiation temperatures (i.e. above 400^{o}C) because loops had larger sizes [98].

The results of all the **g.b** experiments are based on loops whose Burgers vectors could be accurately identified. It is important to mention that in some specimens, there were a small number of loops (typically of size <5nm) whose Burgers vectors could not be identified. This was mostly due to weak or anomalous image contrast or surface contamination. In addition to this, in some of the **g.b** experiments, a fraction of loops could remain out-of-contrast throughout all the diffraction conditions. An example of this would be a[001] loops in the experiments described in chapter 4.4.1 and 4.4.3, where the Burgers vector was perpendicular to the plane of the foil. Loops with this Burgers vector would be out of contrast in all the reflections used. It is

possible to estimate the number of missing a[001] loops in this condition by assuming all three types of a<100> loops are equally populated. The actual total number of a<100> loops is then extrapolated to be 50% more than the total identified a<100> loops. The possible existence of these missing loops was not included in the results of chapter 4.4 in order to make comparison to parallel thin-foil work easier. In the thin-foil work, the number of missing loops is hard to be extrapolated. This was because the preferential loss of loops to the surface could result in an unbalanced loop variants proportion.

In the in-situ thin-foil experiments, the loss of glissile a/2<111> loops to the surface has been observed. The loss of loops was not observed in the bulk-irradiated specimens under the microscope; however, it is possible that some loops could have been lost during electro-polishing. The possibility of a/2<111> loops lost to surface during electro-polishing could not be quantified.

Chapter 5: Radiation damage in Fe-Cr Alloys

Fe-Cr alloys with Cr concentrations of 8% and 11% were irradiated with the Fe specimens.

5.1. Damage characterisation in Fe-8Cr: overview.

A series of micrographs of Fe-8Cr specimens irradiated from 300^{o}C to 500^{o}C is shown in **Fig.5.1.0.1** and **Fig.5.1.0.2**. The damage structures in specimens irradiated at 300^{o}C were similar to those found in Fe under the same condition. Compared with pure Fe, Fe-8Cr irradiated at 400^{o}C had smaller numbers of loops but of similar sizes. At 500^{o}C, damage in Fe-8Cr consisted of a high density of much smaller loops than was found in Fe specimens. In the one case where it was possible to determine the nature of loops, loops of type a/2<111> were found to be interstitial. The nature determination was attempted in other cases but it was not successful due to experimental difficulties (e.g. non-conventional specimen preparation). No voids were found in any Fe-8Cr specimen. Quantitative analyses of loops sizes and densities are shown next.

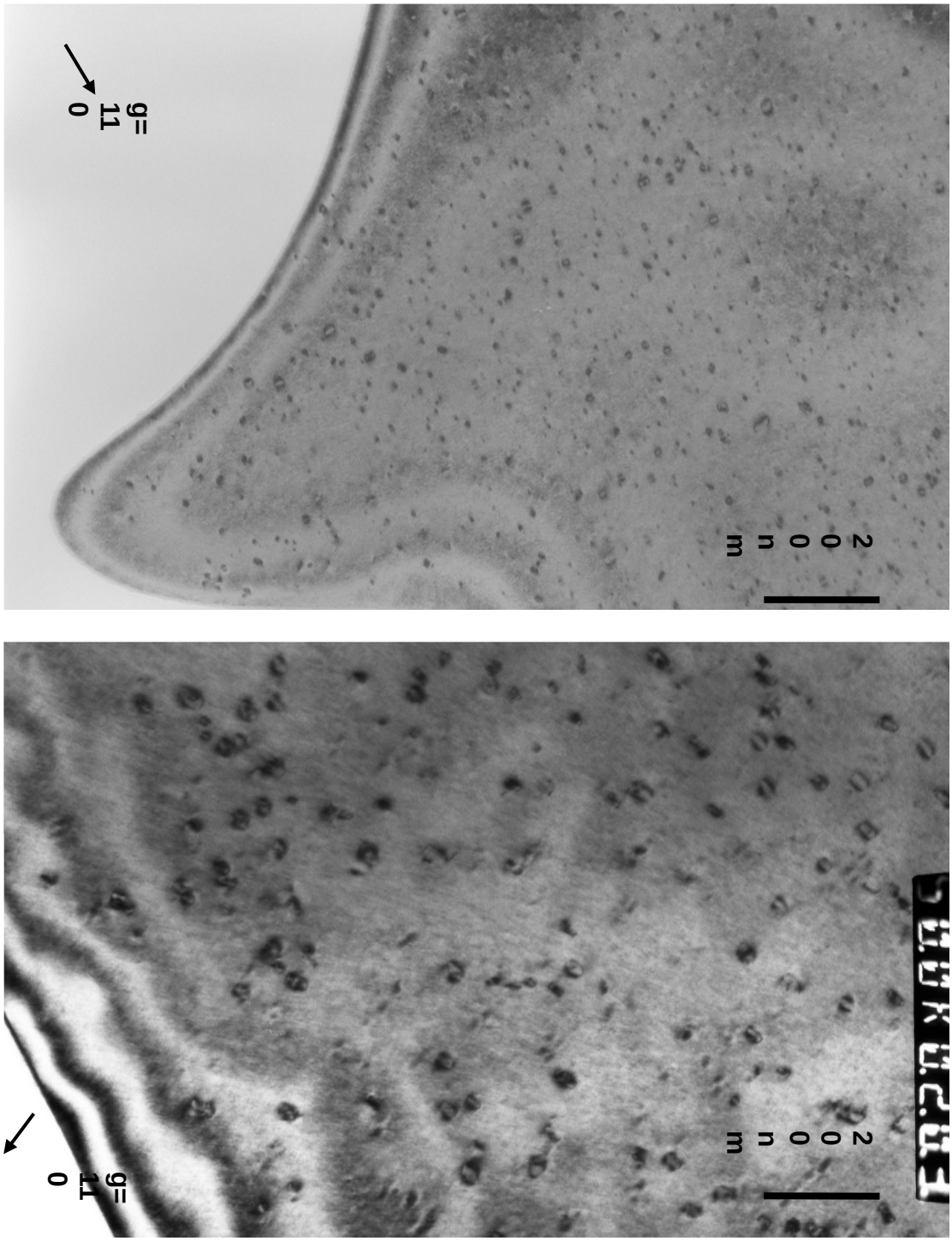

Fig.5.1.0.1 Micrographs of Fe-8Cr showing (upper): specimen irradiated at 300°C to 2.5dpa; (lower): specimen irradiated at 500°C to 2.5dpa. Both pictures were taken near an [001] zone axis with g=110.

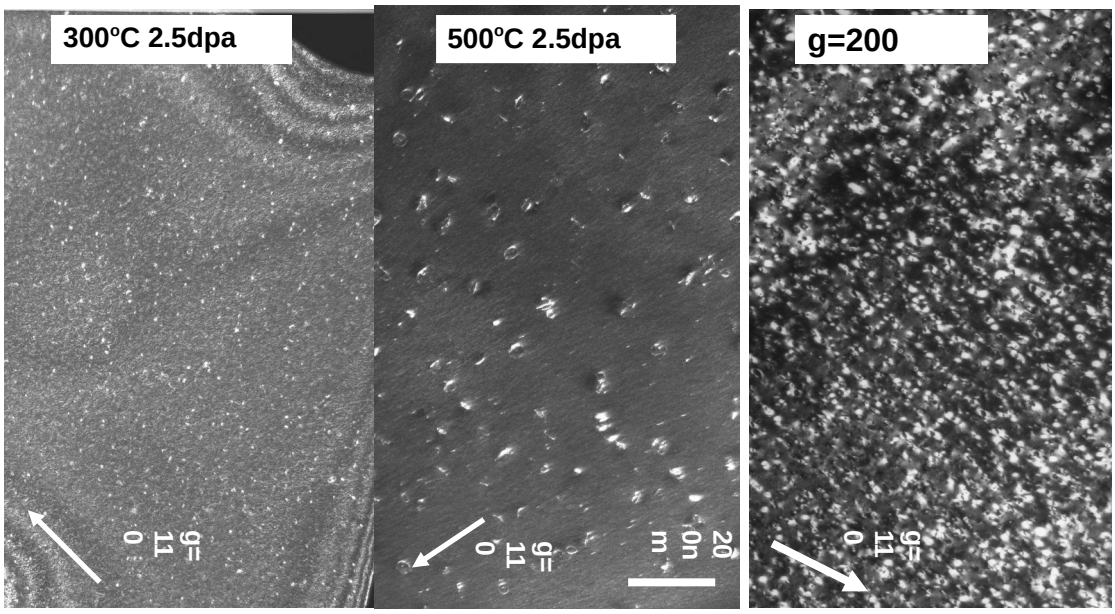

Fig.5.1.0.2 Micrographs showing damage structures at different irradiation conditions.

5.1.1 Loop Size Distributions

The sizes of the dislocation loops in the Fe-8Cr specimens were measured using the same method as in pure Fe (Chapter 4.1). **Fig.5.1.1.1** shows loop image size distributions at 500°C at different irradiation doses. It may be seen that an increase in dose from 2.5 to 7 dpa had little effect on the spread of the distributions. This was very different to what was found in Fe at 500°C where the distributions broadened by about 60%. The loop image size distributions at temperatures of 300°C and 500°C at the same dose (2.5dpa) are plotted in **Fig.5.1.1.2**. The increase in temperature caused a shift to larger sizes in the distributions, similar to what was found in pure Fe.

The average loop sizes under different irradiation conditions are plotted in **Fig.5.1.1.3**. At different irradiation temperatures, the average loop sizes increased from 10.9 ± 1.3 nm at 300°C to 30.9 ± 3.4 nm at 500°C. At an irradiation temperature of 500°C, the average loop size actually decreased from 30.9 ± 3.4 nm at 2.5dpa to 27.0 ± 2.8 nm at 7dpa. However, the reduction lies within the margin of the errors.

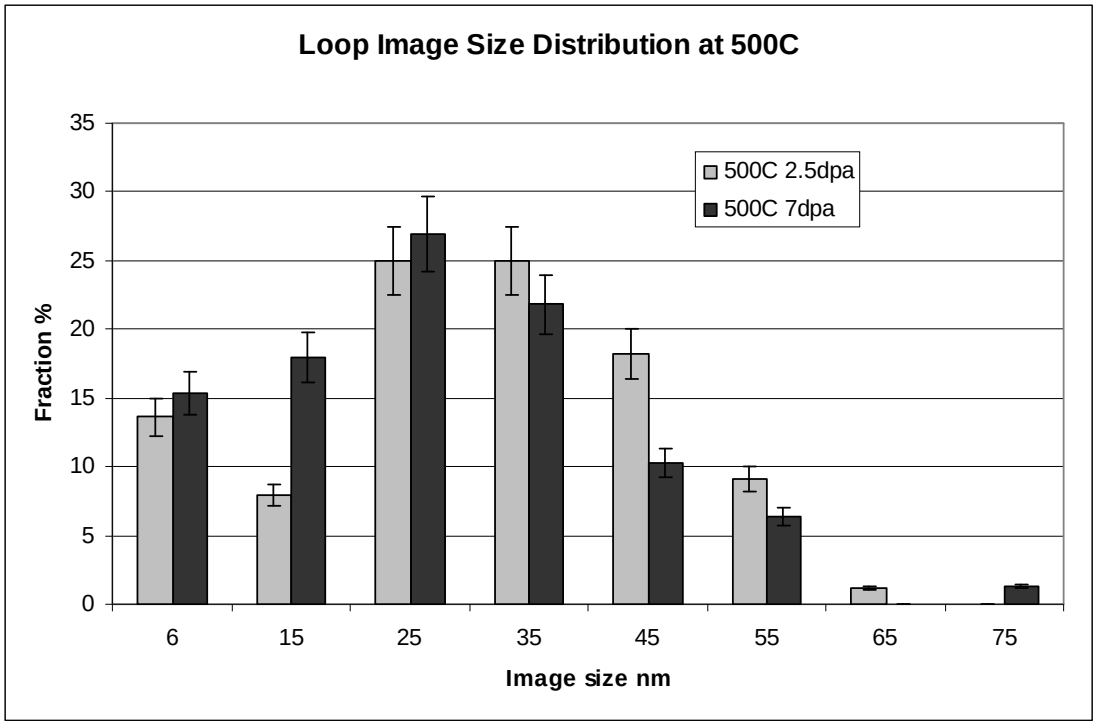

Fig.5.1.1.1 Loop image size distribution in an Fe-8Cr specimen irradiated at 500°C.

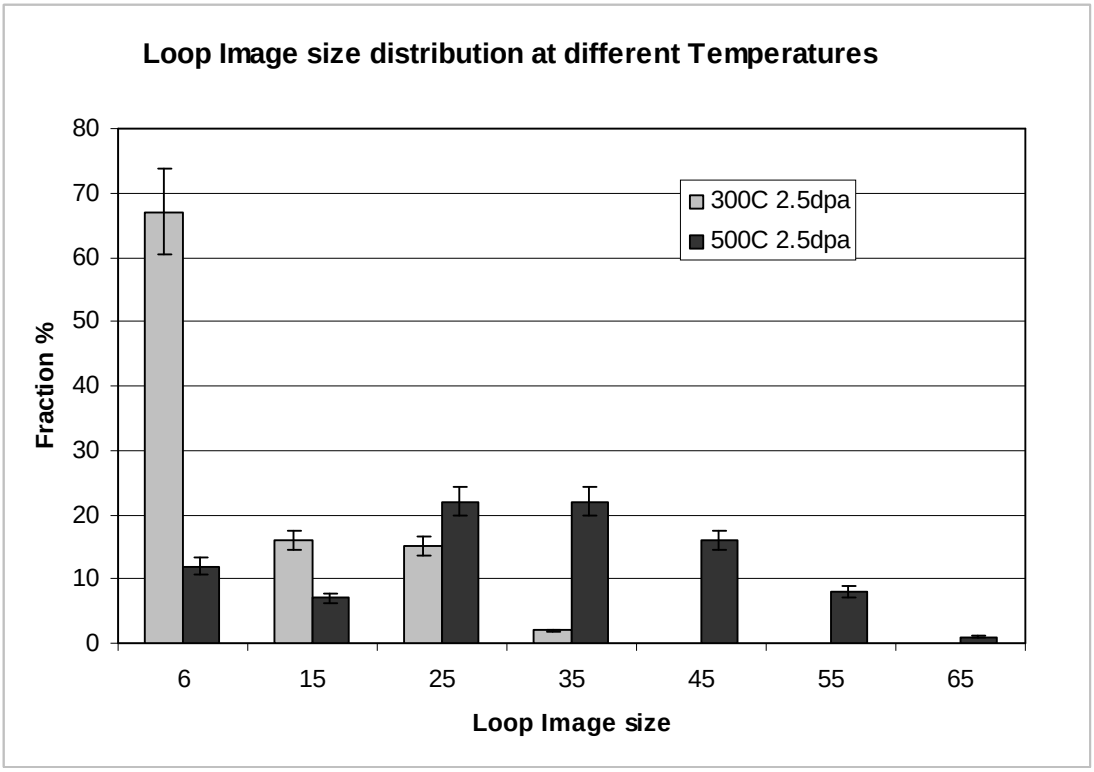

Fig.5.1.1.2 Loop image size distribution in Fe-8Cr specimens irradiated at different temperatures.

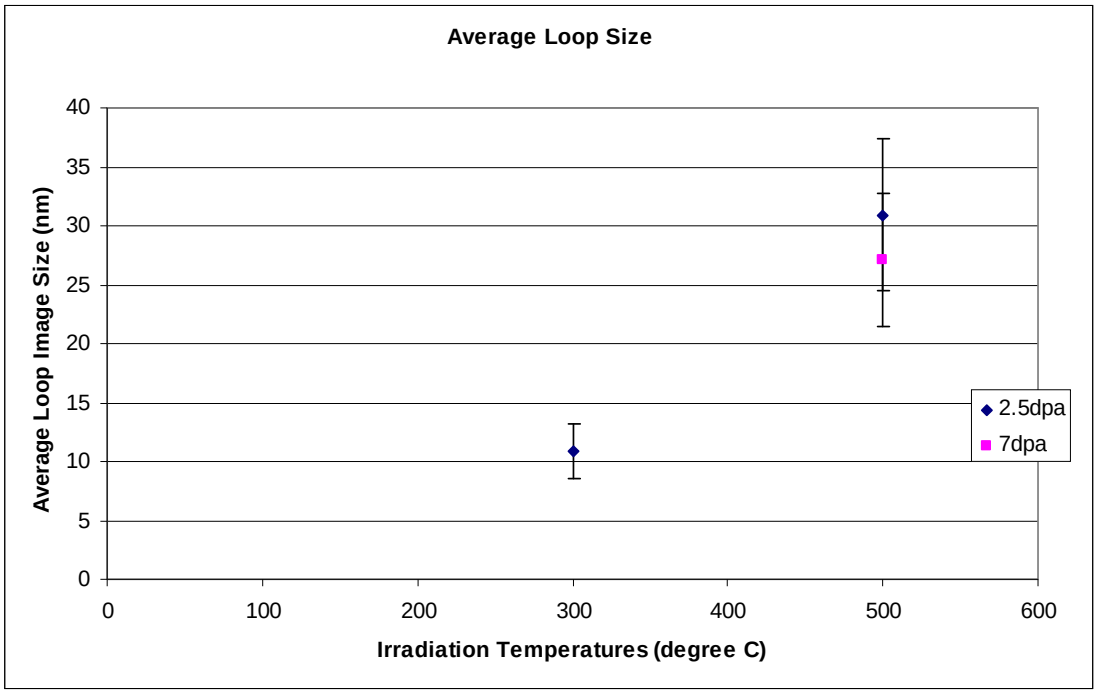

Fig.5.1.1.3 Average loop sizes in Fe-8Cr at different conditions.

5.1.2 Loop Number Densities

The dislocation loop number densities in Fe-8Cr were obtained using the method described for pure Fe (Chapter 4.1). The foil thicknesses were not accurately measured in Fe-8Cr specimens. Estimations of the foil thickness were made using thickness fringes [102] and the errors in the densities results include such uncertainties.

The number density measurements are shown in **Fig.5.1.2**.

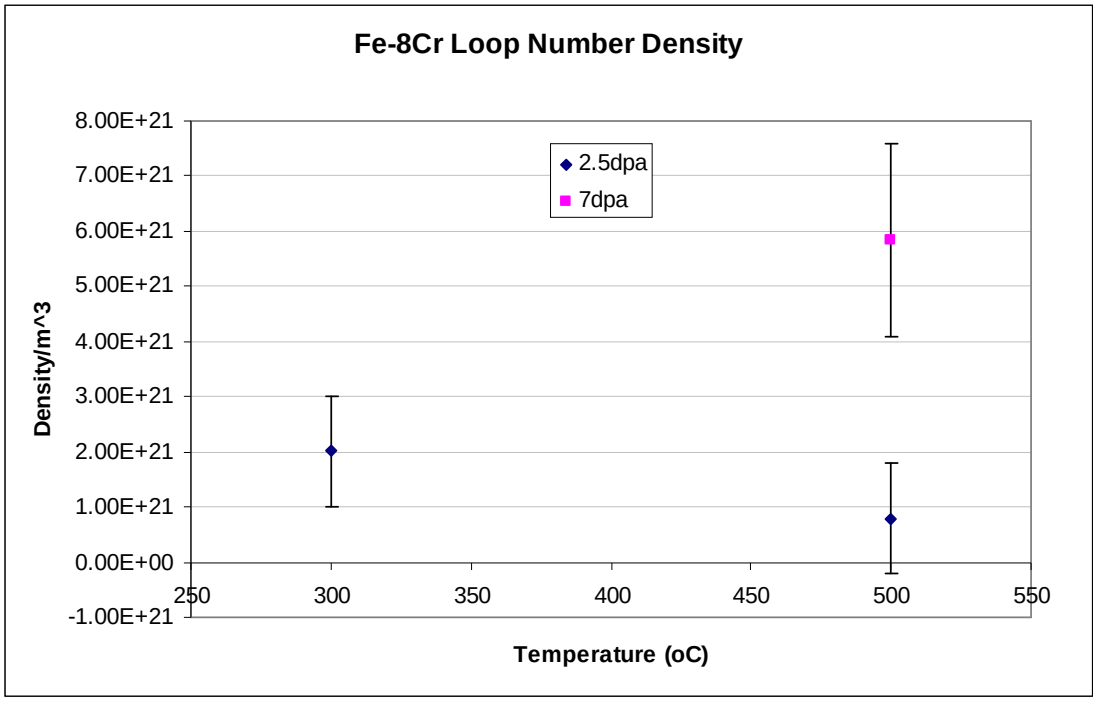

Fig.5.1.2 Loop number densities in Fe-8Cr.

5.1.3. Burgers vector determination

The Burgers vectors of dislocation loops in Fe-8Cr were characterised using the **g.b** contrast method described in chapter 3.3.

5.1.3.1. Burgers vector characterisation on 300°C/2.5dpa specimens

The **g.b** analysis of a specimen irradiated in this condition is shown as an example in the experimental methods chapter 3.3. **Fig.5.1.3.1** shows a more complete collection of micrographs, with both +**g** and -**g** micrographs. The micrographs were taken close to an [001] foil orientation. The four different reflections near this orientation allow loops of type a/2<111> and a<100> to be distinguished. Among the 200 loops which were analysed it was found that 54 ± 4% had a<100> Burgers vectors.

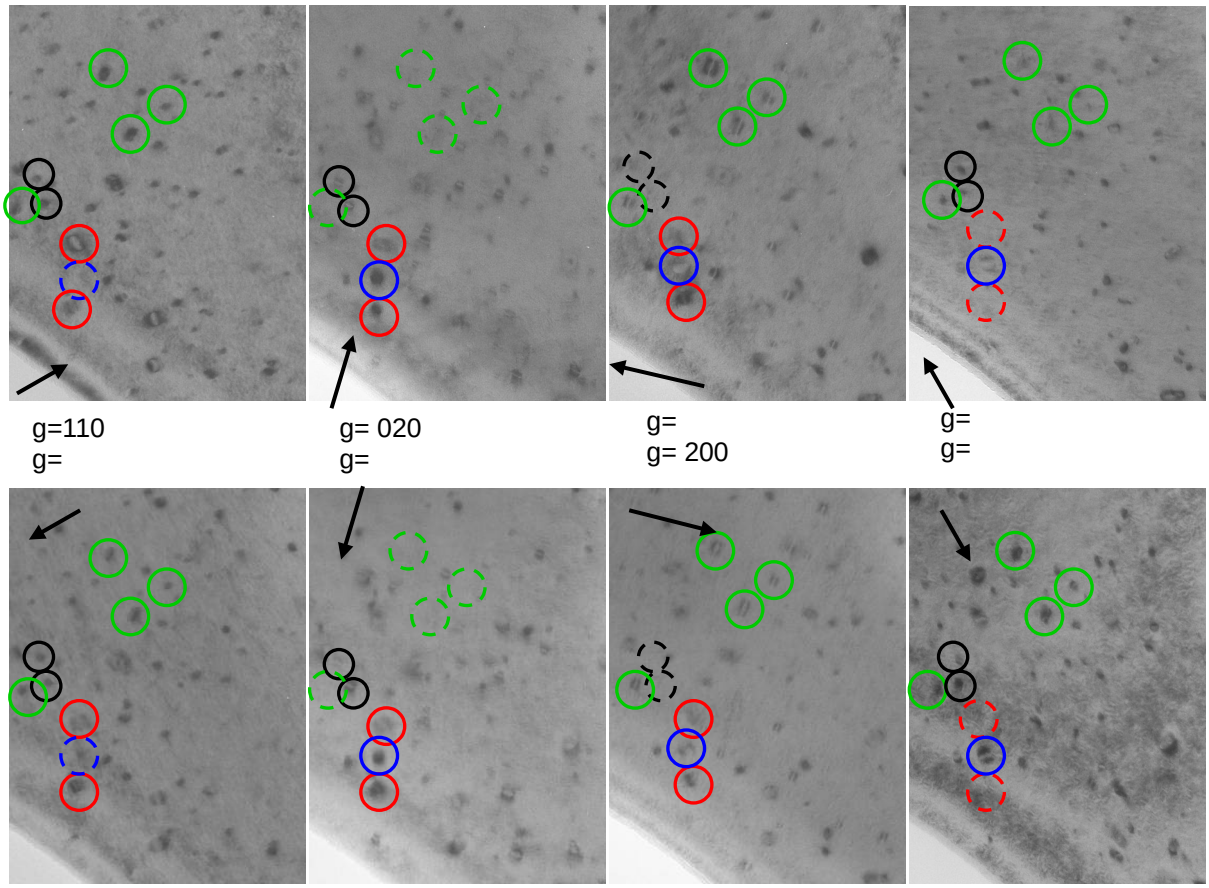

Fig.5.1.3.1 Burgers vector analysis of Fe-8Cr irradiated at 300°C to dose of 2.5dpa. Red circles correspond loops with b= a/2[111] or a/2[$1\,1\,\bar{1}$]; blue circles have b= a/2[$\bar{1}\,11$] or a/2[$1\,\bar{1}\,1$]; green circles have b=a[100] and black circles have b=a[010].

5.1.3.2. Burgers vector characterisation on 500°C/7dpa specimens

Fig.5.3.1.2 shows micrographs of a specimen irradiated at 500°C to a dose of 7dpa. The micrographs were taken near an [001] zone axis. Due to the quality of the specimen, it was possible to obtain only two reflections, **g** = 020 and **g** = 200. About 80 loops were analysed using these two reflections. Most of the loop population examined had Burgers vectors of type **b** = a/2<111>, e.g.

loops marked with red circles. Only about 10% of the loops had **b** = a<100> (e.g. loops marked with blue circles had **b** = a[010]). It was also found that the loops with a<100> Burgers vectors were on average smaller in size than a/2<111> loops.

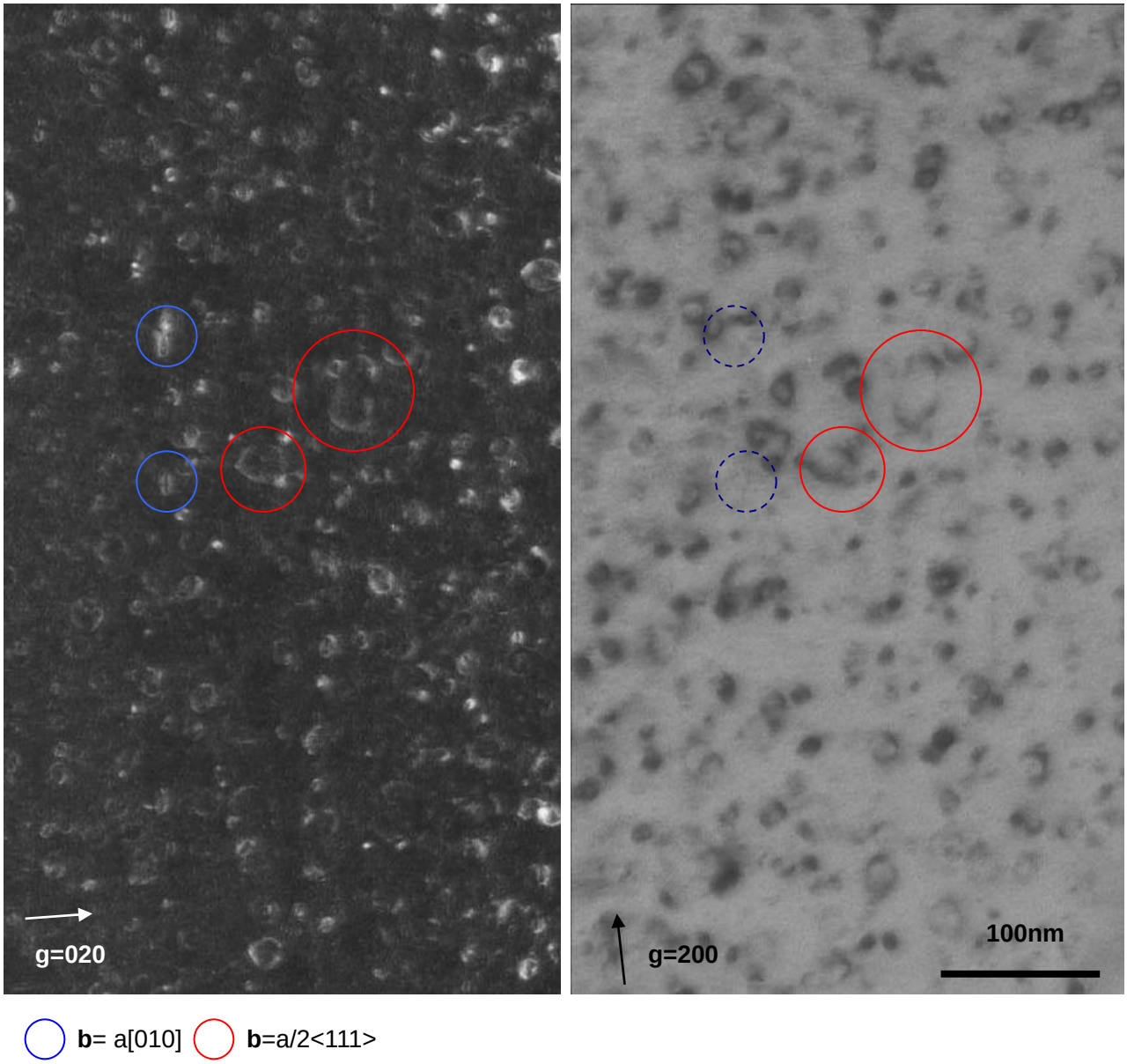

Fig.5.3.1.2 Burgers vector analysis of Fe-8Cr specimen irradiated at 500°C to 7dpa.

5.1.4. Loop Nature determination

The nature (i.e. interstitial/vacancy) of the loops in Fe-8Cr irradiated at 300°C was studied using the inside-outside technique. The detailed method of this inside-outside experiment has been explained in the experimental methods chapter (Chapter 3.3). As seen in **Fig.5.1.4**, the circled a/2<111> loop showed inside-outside contrast when imaged in **g**= ± [$\bar{1}10$]. The analysis shows that this loop has interstitial character.

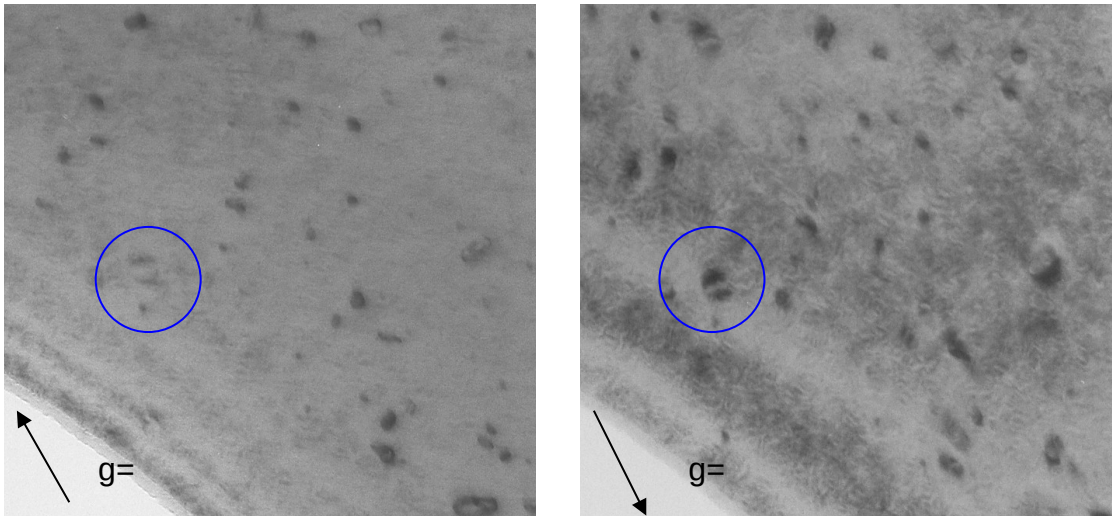

Fig.5.1.4 Micrographs showing a ½<111> loop showing inside-outside contrast near an [001] zone axis.

5.1.5 Interstitial point defect densities

Previous sections provided information on the Burgers vectors and interstitial nature of the loops. By estimating the number of interstitials in dislocation loops (for details of the estimation refer to chapter 4.1.5), the interstitial point defect densities (defined as the densities of interstitials contained in visible loops) were calculated and are plotted in **Fig.5.1.5**.

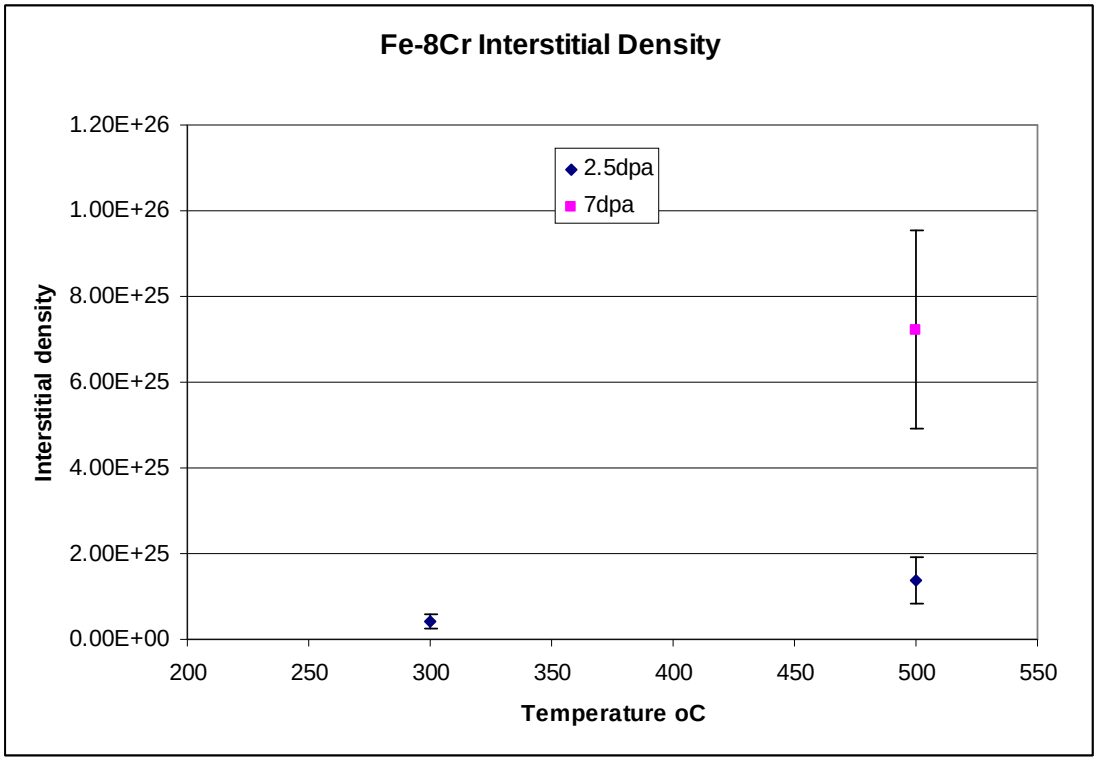

Fig.5.1.5 Interstitial densities in Fe-8Cr at different irradiation conditions.

5.2. Damage Characterisation in Fe-11Cr: overview

The damage structures in Fe-11Cr specimens were qualitatively similar to those found in Fe-8Cr. **Fig.5.2** shows a series of micrographs illustrating the damage structures under different irradiation conditions. Specimens irradiated at 500^{o}C to a dose of 2.5dpa had a similar low damage density to that found in Fe-8Cr at the same condition. Loop nature determination was carried out in a specimen irradiated at 300^{o}C and interstitial a<100> loops were found. No voids were found in any Fe-11Cr specimens.

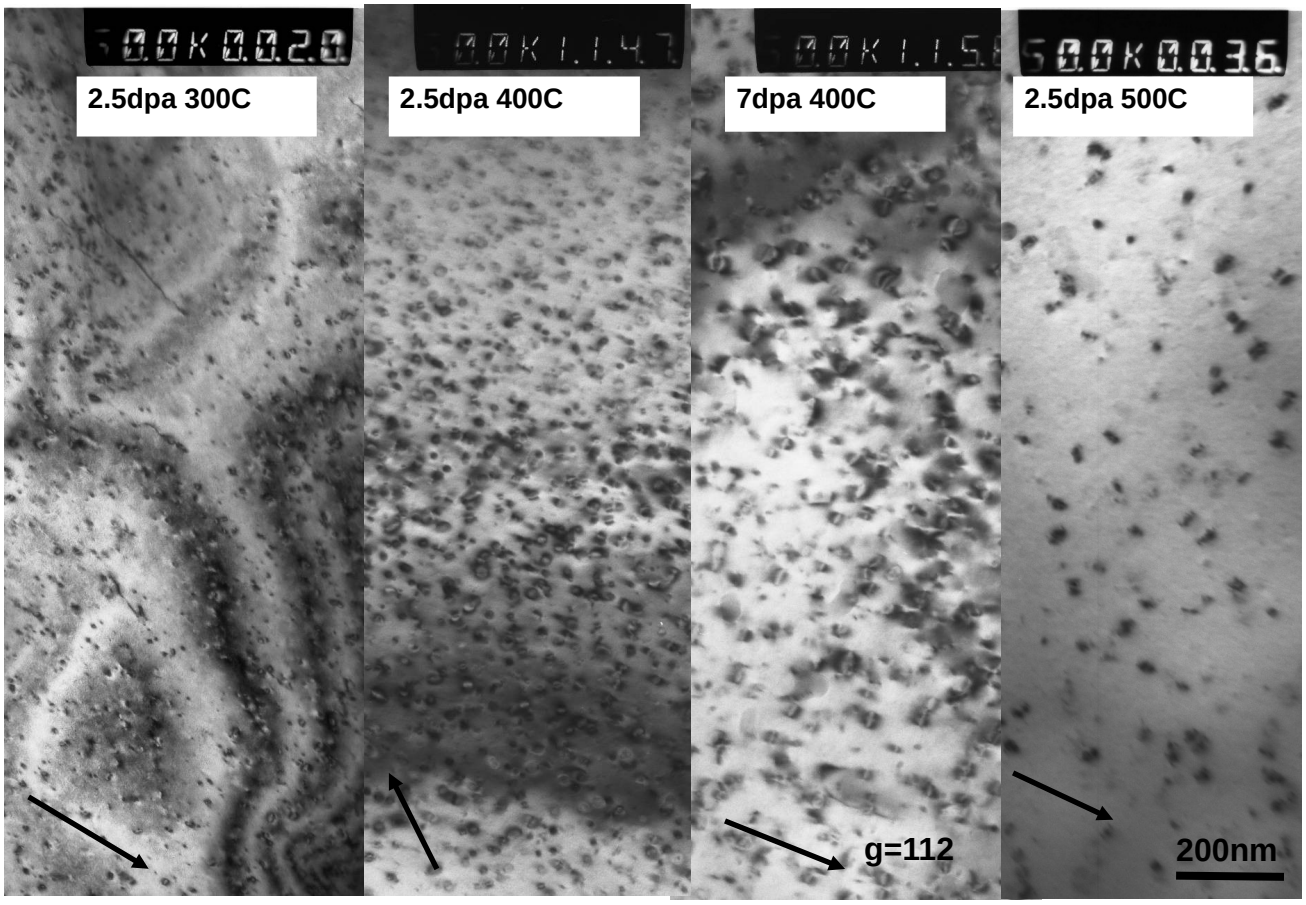

Fig.5.2 Micrographs showing damage structure in Fe-11Cr at different irradiation conditions.

5.2.1 Loop Size Distributions

The loop size distributions at 400°C at doses of 2.5dpa to 7dpa are shown in **Fig.5.2.1.1**. The average loop size increased from 19.7 ± 2.3nm to 32.7 ± 2.4 nm as the dose increased.

A comparison of loop image size distributions in specimens irradiated to the same dose (2.5dpa) is illustrated in **Fig.5.2.1.2**. The average loop size increased from 11.4 ± 1.4 nm at 300°C to 19.7 ± 2.3nm at 400°C to 38.5 ± 3.5nm at 500°C.

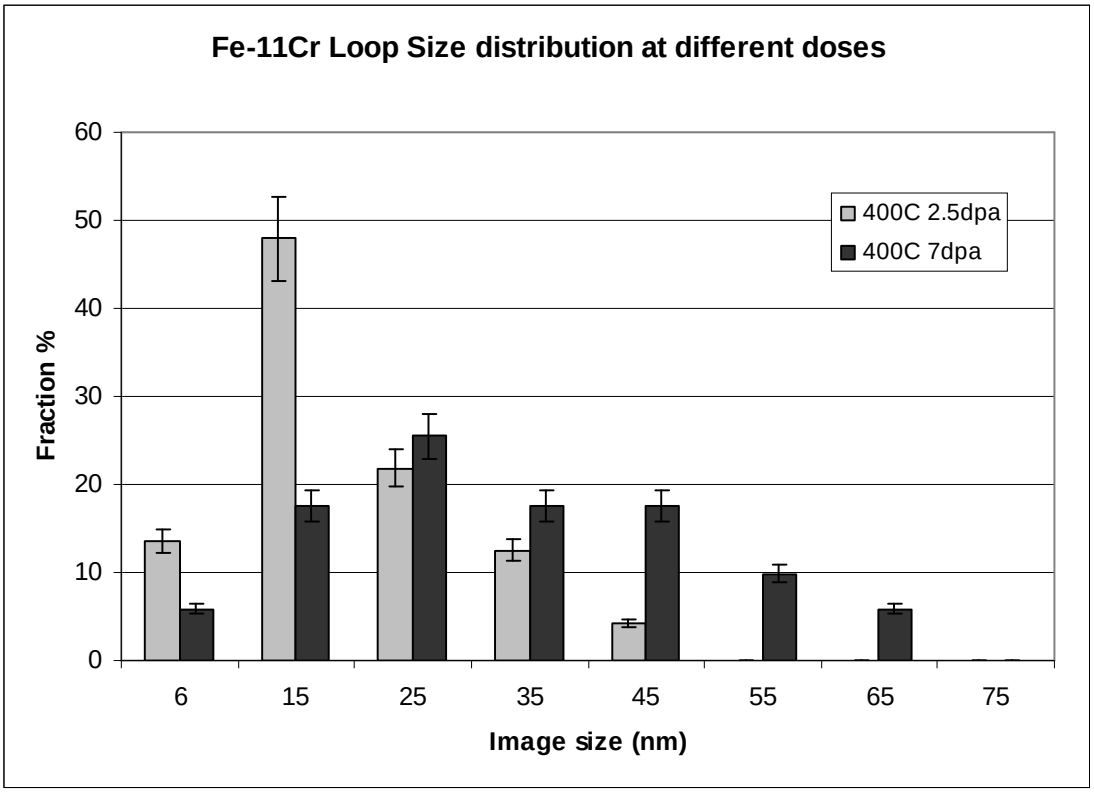

Fig.5.2.1.1 Loop image size distributions in Fe-11Cr specimens irradiated at 400°C.

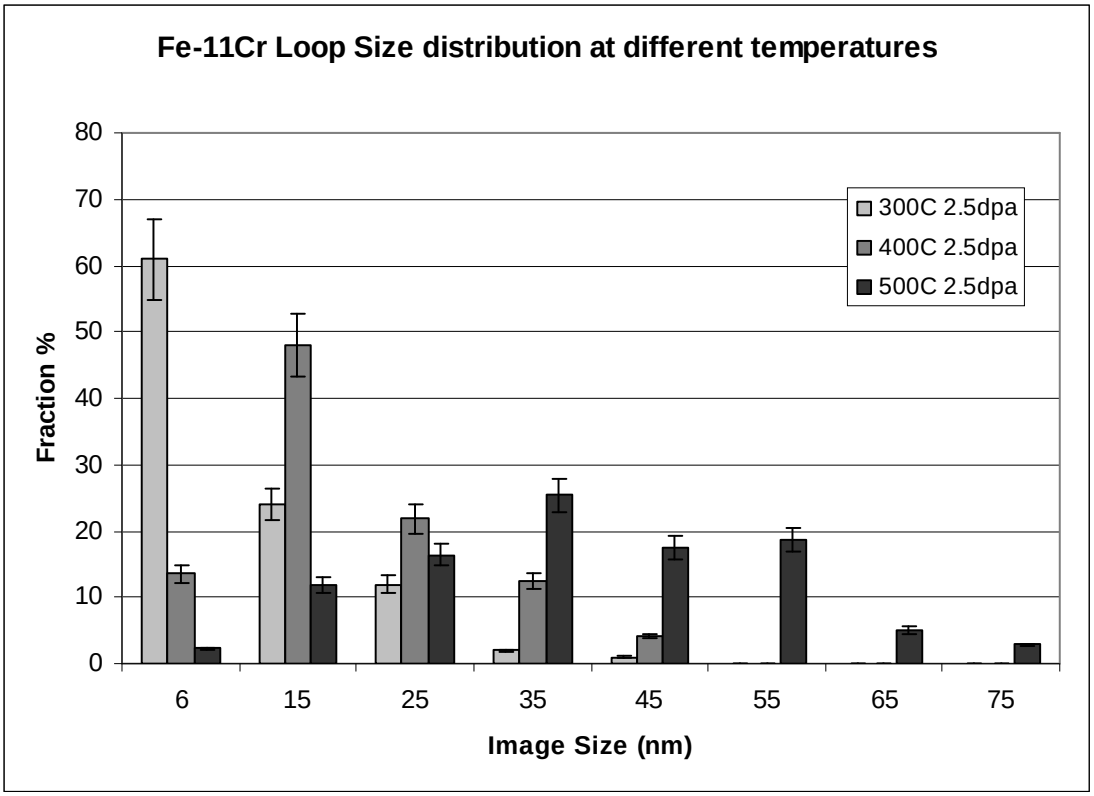

Fig.5.2.1.2 Loop image size distribution in Fe-11Cr specimens irradiated at different temperatures.

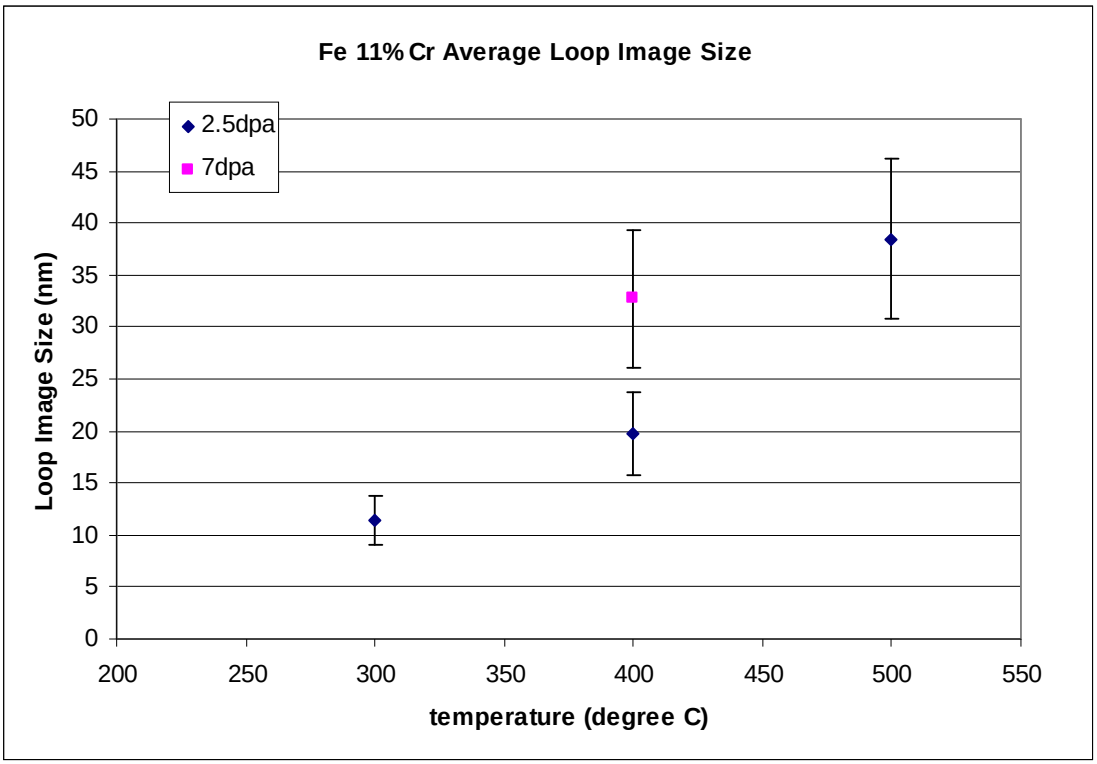

Fig.5.2.1.3 Average loop sizes in Fe-11Cr specimens irradiated at different conditions.

5.2.2. Loop number densities

The number densities of the dislocation loops in Fe-11Cr were measured using the same method as previously (refer to chapter 4.3). Results are shown in **Fig.5.2.2**.

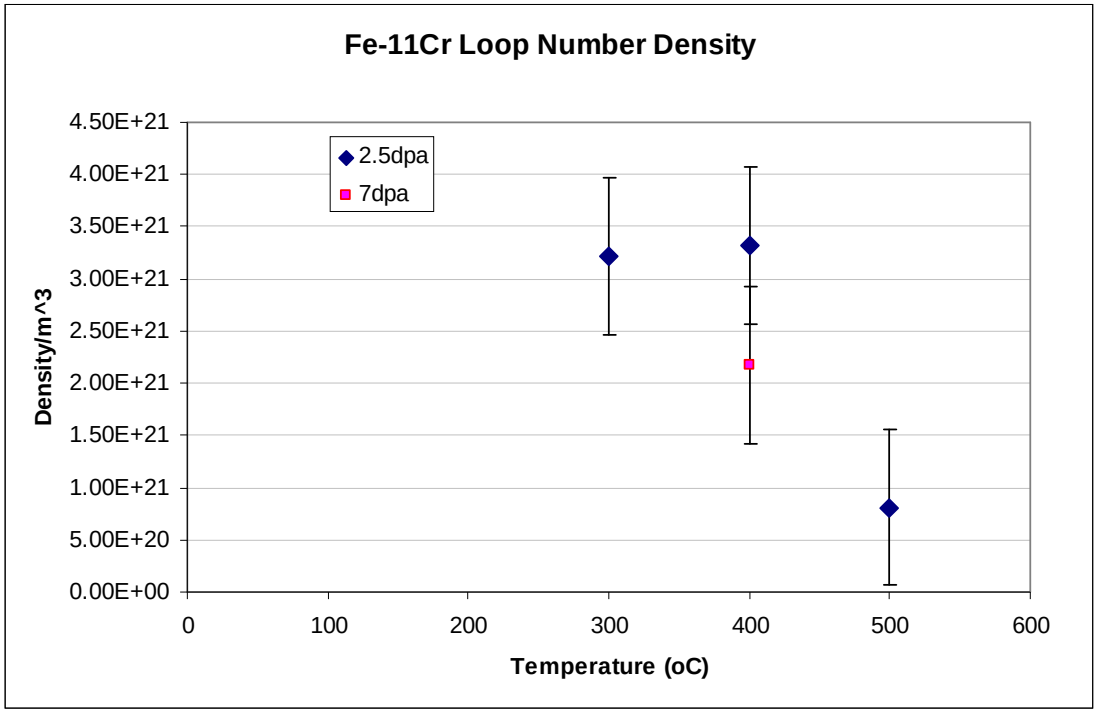

Fig.5.2.2 Loop number density measurements in Fe-11Cr.

5.2.3. Burgers vector characterisation

5.2.3.1 Burgers vector characterisation on 300°C/2.5dpa specimens

Fig.5.2.3.1 shows the **g.b** analysis carried out in Fe-11Cr irradiated at 300°C. The foil orientation was near the [113] zone axis and three diffraction

conditions were achieved with **g** = [$\bar{1}10$], [$\bar{1}\bar{2}1$] and [$\bar{2}\bar{1}1$]. The **g.b** table for this experiment is shown in **Fig.5.2.3.1**. As shown in the **g.b** table, because two sets of results (i.e. a/2[111] and [001]) go out of contrast only in the first micrograph, only part of the Burgers vector types could be determined under this condition. The red circles mark loops with either a[100] or a[010] type Burgers vector, and the a/2[$\bar{1}11$] and a/2[$1\bar{1}1$] loops are marked with blue and green circles respectively. Among the 100 resolvable loops, it was found that 63 ± 6% had a<100> type Burgers vectors.

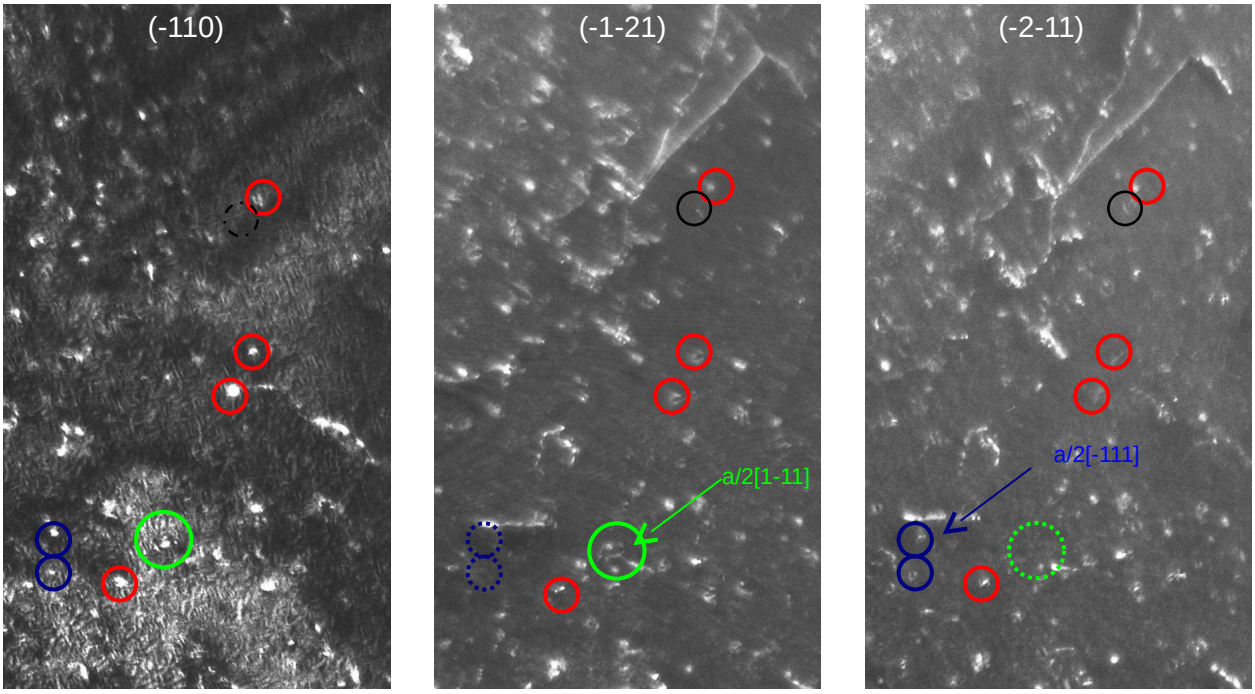

g\b	a/2[111]	a/2[$\bar{1}11$]	a/2[$1\bar{1}1$]	a/2[$11\bar{1}$]	a[100]	a[010]	a[001]
$\bar{1}10$	**0**	**1**	**1**	**0**	**1**	**1**	**0**
$\bar{1}\bar{2}1$	**1**	**1**	**0**	**2**	**2**	**1**	**1**
$\bar{2}\bar{1}1$	**1**	**0**	**1**	**2**	**1**	**2**	**1**

Fig.5.2.3.1 Contrast experiment for Burgers vector determination of Fe-11Cr near z=[113]. Specimen was irradiated at 300°C.

5.2.3.2 Burgers vector characterisation on 500°C/2.5dpa specimens

Fig.5.2.3.2 shows a **g.b** experiment carried out near the [011] zone axis. In this experiment, the number of diffraction conditions is 'incomplete', because as shown in the **g.b** table (**Fig.5.2.3.2**), loops with Burgers vectors a[100] and a/2[111] both go out of contrast only in the $0\,1\,\bar{1}$ reflection. This means that these two types of loops cannot be distinguished just by looking for contrast extinctions across the 3 micrographs. However, by comparing the contrast of the images with TEM loop image simulations [55], |**g.b**| = 1 contrast could be distinguished from| **g.b** | = 2 and therefore a full Burgers vector analysis was achieved. About 100 loops were analysed and it was found that 69 ± 7% had a<100> Burgers vectors.

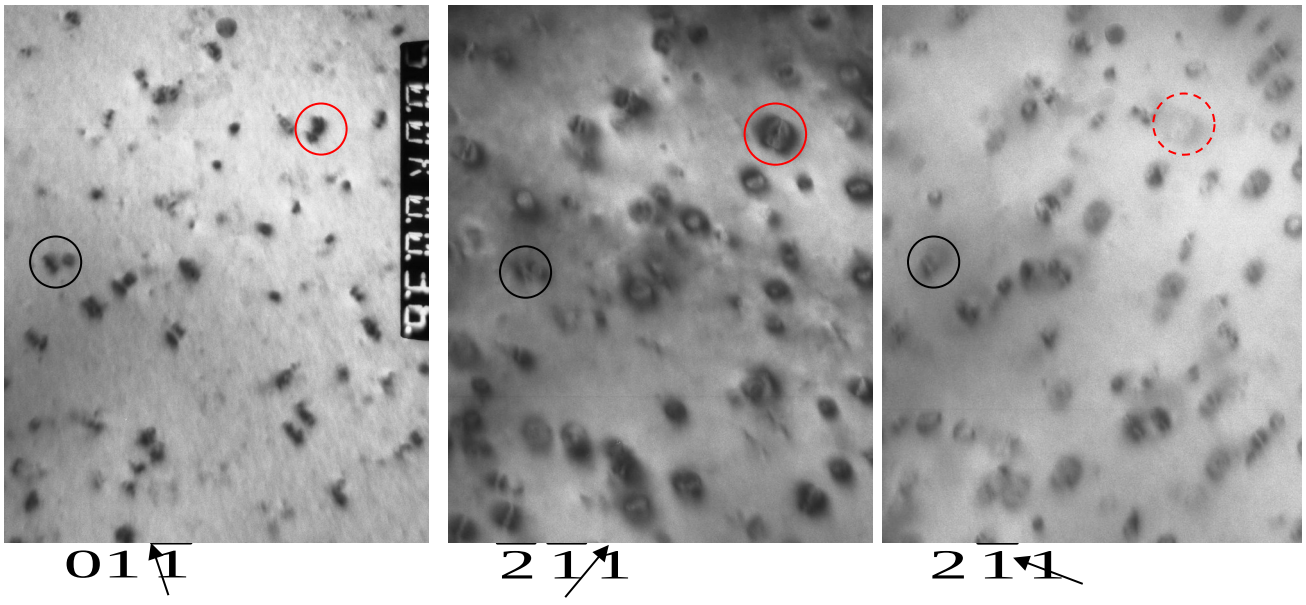

g\b	a[100]	a[010]	a[001]	a/2[111]	a/2[$\bar{1}\,1\,1$]	a/2[$1\,\bar{1}\,1$]	a/2[$1\,1\,\bar{1}$]
$0\,1\,\bar{1}$	**0**	**1**	**1**	**0**	**0**	**1**	**1**
$2\,\bar{1}\,1$	**2**	**1**	**1**	**1**	**1**	**2**	**0**
$\bar{2}\,\bar{1}\,1$	**2**	**1**	**1**	**1**	**1**	**0**	**2**

Fig.5.2.3.2 Micrographs showing contrast experiment on Fe-11Cr irradiated at 500°C. The loop with

black circle marks b=a<100> type; the loop with red circle marks b=a/2[$1\,1\,\bar{1}$].

5.2.4. Loop nature determination

The nature of some of the loops in Fe-11Cr was determined using the inside-outside technique described in chapter 3.4. The burgers vector of loops marked with white circles in **Fig.5.2.4** were determined by **g.b** experiment (see Chapter 5.2.3.1) to be **b** = a[100]. These loops exhibit outside contrast with **g** = $2\,1\,\bar{1}$ and **g** = $1\,2\,\bar{1}$, and inside contrast with **g**= $\bar{2}\,\bar{1}\,1$ and **g** = $\bar{1}\,\bar{2}\,1$. Assuming these loops are close to edge, the inside-outside contrast behaviours of both ±**g** pair show a consistent interstitial character of the loop.

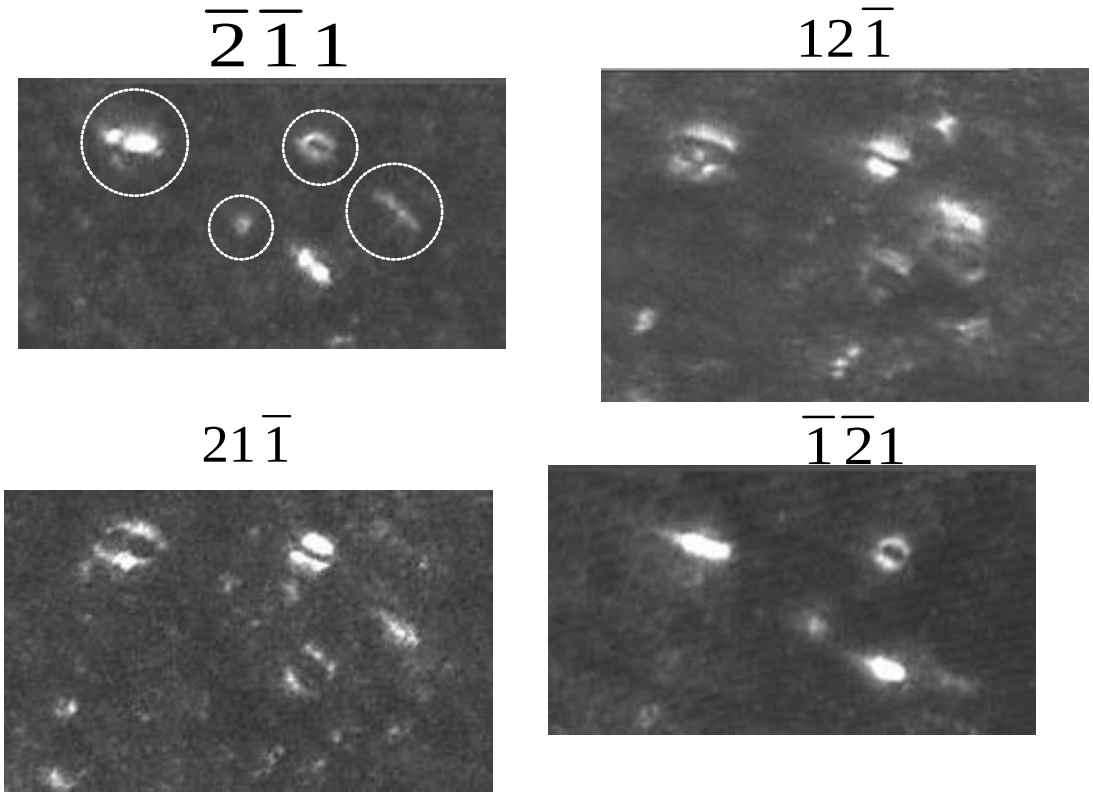

Fig.5.2.4 Micrographs showing inside-outside contrast of loops with b=a[100] (circled loops) near [113] zone axis in Fe-11Cr irradiated at 300°C.

5.2.5 Interstitial point defect densities

Based on the Burgers vector and nature determinations and the assumptions discussed in chapter 4.2.5, the number densities of interstitials were estimated. These are plotted for different irradiation conditions in **Fig.5.2.5**.

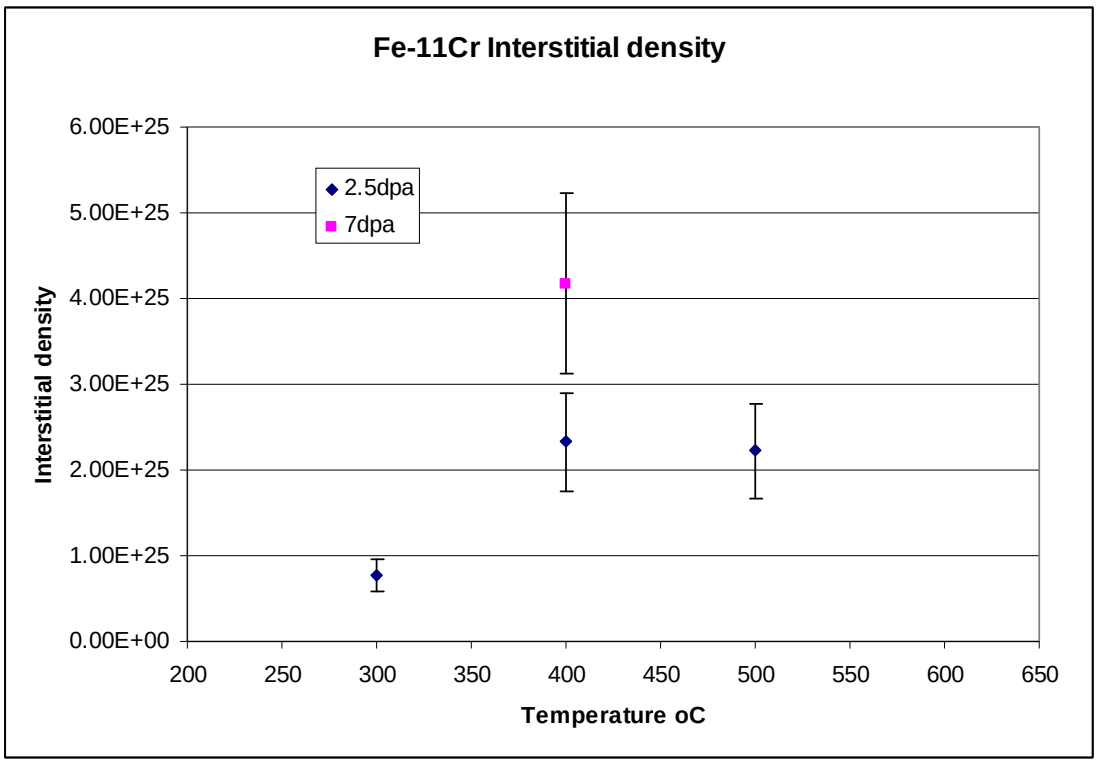

Fig.5.2.5 Interstitial densities in Fe-11Cr specimens at different irradiation conditions.

Chapter 6: Discussion

In this chapter the experimental results of this work are discussed in context with parallel in-situ experiments, and with results from the literature.

The experimental results in bulk-irradiation experiments have been described in detail in chapters 4 and 5. Some details of the recent parallel thin-foil work carried out by the Oxford Group will be described in this chapter in order for comparison to be made. Both methods have their advantages and limitations. The in-situ experiments suffer from surface artefacts due to irradiation being carried out in thin-foils. The bulk irradiation experiment requires a separately prepared specimen for each irradiation condition, and therefore introduces reproducibility issues from specimen polishing. Note that the thin-foil experiments were mostly carried out on UHP Fe, containing ~1ppm C, <5ppm N, and <10ppm Si. The bulk experiments used less pure materials (details in chapter 2.2).

6.1. Production of near surface loops

The production of radiation damage has been studied extensively in many materials using thin-foil irradiations, where specimens can be looked at in the TEM as the dose progresses. It is not possible to follow the initial production of dislocation loops in bulk irradiation experiments. However this section is included in this thesis because the damage production mechanism has been studied in parallel in-situ thin foil experiments by Yao et al [60], Hernandez-

Mayoral et al [63], and Jenkins et al [70]. Even though these thin-foil experiments use much lower energy ions (150keV compared with 2MeV in the bulk experiment), the loop production mechanism in thin-foils may be a good representation of the bulk, because higher energy ions (>1MeV) initially lose most of their energy through electronic excitation but cause displacement damage (via displacement cascades) when their energy falls below about 200keV.

As described in chapter 1.4.1, Robertson et al. [67] showed that collapse of individual, isolated displacement cascades to vacancy loops does not occur in Fe under self-ion irradiation. Visible loops were only seen at high doses when cascade overlap happens. This was believed to be due to the presence of invisible sub-microscopic vacancy clusters which only aggregated to visible loops at overlap doses. Molecular dynamics (MD) simulations show that sub-microscopic clusters of both interstitial and vacancies are produced within individual cascades in Fe [104, 105]. This finding is consistent with the results of Robertson et al. Robertson considered that mobile interstitials would be quickly lost to the foil surfaces, but that the concentration of less mobile vacancy clusters would increase to the point that collapse could be triggered.

Hernandez-Mayoral et al. [63] have also carried out ex-situ thin-foil experiments, using the ion-irradiation facility at Saclay. Their irradiations were made with 150KeV Fe^{2+} ions to a maximum dose of $2x10^{19}$ ions m^{-2} (~13dpa). Fe specimens of different purities (with C content varying from <5ppm to

100ppm) were examined at 300°C and RT. Consistent with previous experiments, no damage was observed below 0.1dpa in UHP-Fe.

Recent in-situ thin-foil experiments, carried out on the Argonne facility by Yao et al. [60] have found similar damage development in Fe and Fe-Cr alloys, in that loops were seen only at overlap doses. In their pure Fe experiments, small visible loops (2-4nm) only started to appear at threshold doses of $2x10^{16}$ ions m^{-2}. The threshold dose for visible damage was somewhat lower in Fe-Cr alloys (i.e. Fe-5Cr, Fe-8Cr, and Fe-11Cr) but was still well into the overlap regime (see **Fig.6.1.1**). It was found that the loop size distribution in Fe-11Cr did not change with dose at doses below $2x10^{18}$ m^{-2}. This suggests that loops were produced in some sort of cascade event and did not grow after their formation.

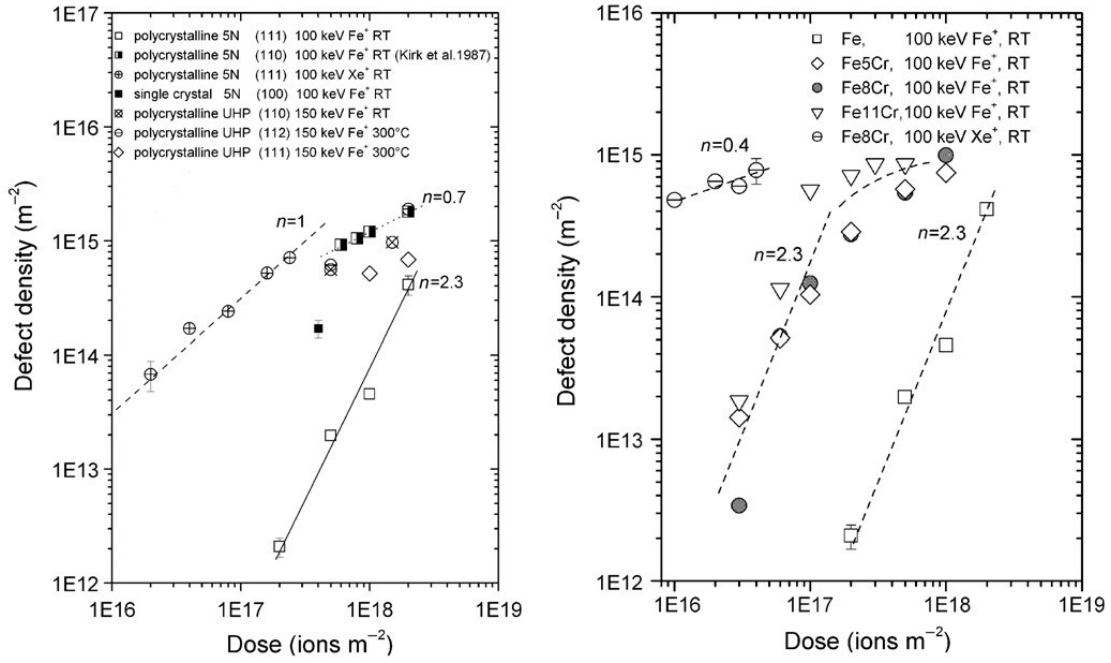

Fig.6.1.1: Defect areal densities versus dose for (left) pure Fe. (right) Fe and Fe-Cr alloys irradiated with 100keV [60].

The nature of the loops in these experiments is difficult to establish, due to their small sizes. Yao et al. [60] attempted to determine the nature of some near-surface loops by separate ex –situ experiments using 30keV Ga^+ ions at room temperature (see **Fig. 6.1.2**). Some loops in thin areas of foil were found to be vacancy by first-layer black-white contrast analysis.

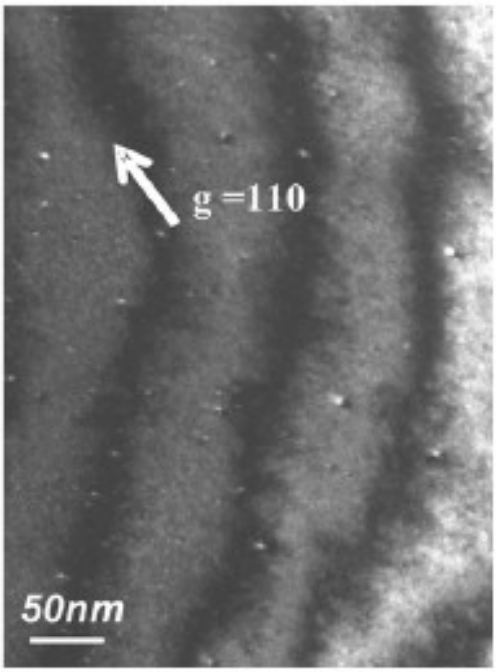

Fig.6.1.2: Two-beam dark field g=110 micrographs of single-crystal (111) Fe-11Cr irradiated in the FIB with 30keV Ga^+ ions to a dose of 1 x 10^{18} ions m^{-2}. The black-white contrast is consistent with first-layer vacancy loops [60].

It was also found from analyses of successive video frames that the loops appeared over a rather long period of up to 1/5 second, again suggesting loop formation by the aggregation of invisible sub-microscopic clusters by a diffusion mechanism. However, subsequent observations by the same authors of loop coalescence showed that some of the small loops in thicker areas of foil must have interstitial character [60, 63]. It was found in thin-foil experiments, at higher doses, that specimens contained large loops, up to hundreds of nanometres in size. These large loops could be shown directly by

inside-outside contrast to be of interstitial nature. Since they had formed by the coalescence of smaller, mobile loops, the small loops must therefore also be of interstitial nature. The mechanism by which such small interstitial loops form is unclear. Interstitial clustering within single cascades has not been observed experimentally in pure Fe. Molecular dynamics (MD) studies [104, 105] have shown that interstitial clustering could occur spontaneously in cascades without the need for long-range diffusion; however, such interstitial clusters are sub-microscopic in size and highly mobile in one dimension. It is possible that visible interstitial loops form by aggregation of sub-microscopic interstitial clusters in a similar way as the vacancy loops; however the high mobility of the interstitial clusters suggests that this mechanism is less likely to happen.

Loss of loops was frequently seen in all the in-situ experiments, both during and after the ion irradiation. Loops were seen to be very mobile, hopping from one position to another, both under ion irradiation and under electron irradiation alone. It was observed that both the loop loss and loop hopping were reduced in Fe-Cr alloys compared to pure Fe. This suggests that Cr has the effect of pinning loops and reducing their mobilities.

6.2. Damage evolution in thin-foils

RT to 300ºC

Hernandez-Mayoral et al. carried out in-situ thin-foil experiments to a maximum irradiation dose of $2x10^{19}$ ions m^{-2} (~13dpa) [63]. Damage development at 300ºC and RT showed strong similarities, although the features developed earlier and on a coarser scale at 300ºC than at RT. As observed in video sequences (available online [63]), at doses ≤ $5 x10^{17}$ ions m^{-2}, loops showed very high mobility and interacted elastically, sometimes showing correlated motion, but no coalescence was observed. At doses above about 10^{18} ions m^{-2}, neighbouring loops started to form strings. Contrast experiments showed that these strings consisted of several small loops with the same a/2<111> Burgers vectors. The strings of loops were unstable at first, but become more stable as irradiation proceeded. At doses above about $5x10^{18}$ ions m^{-2}, strings of loops started to coalesce and formed resolvable loops of size greater than 10nm (**Fig.6.2.1**). Loops continued to grow by mechanisms which probably involved both glide and climb. Climb occurred both by absorption of single point defects or sub-microscopic clusters, or by absorption of resolvable loops. Loop shrinkage was also observed, with the possible explanation that vacancy clusters were being absorbed. It was found that all larger loops were of interstitial nature and had Burgers vectors **b**=a/2<111>. They were not of pure edge type but had large shear components. As irradiation continued to even higher doses (10^{19} ions m^{-2}), very large finger-shaped loops (with sizes up to hundreds of nm) were produced by coalescence of large interstitial loops which spatially overlapped.

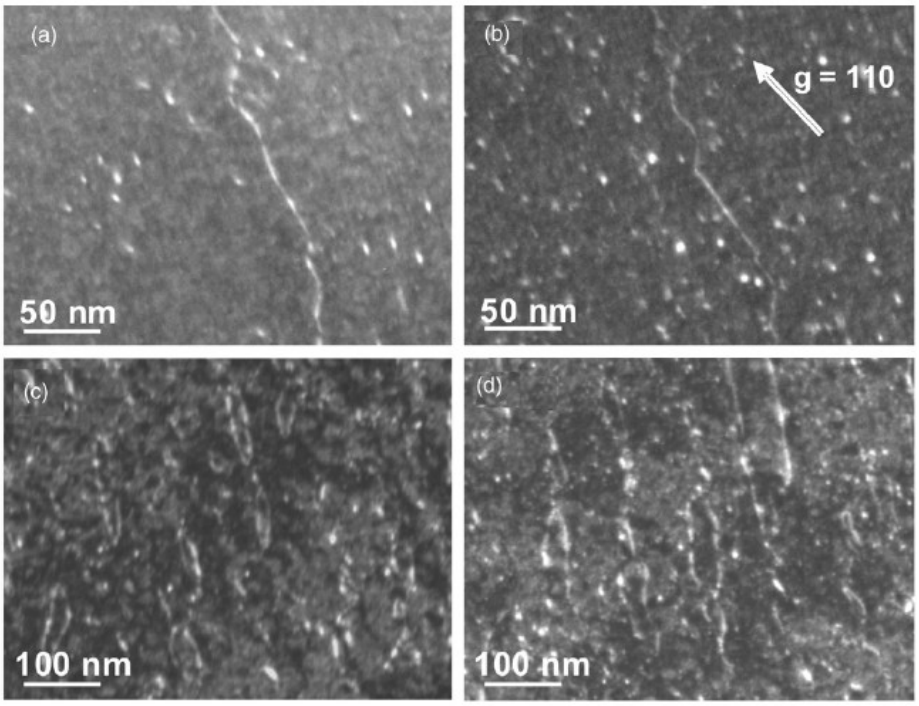

Fig.6.2.1 Development of damage structures in UHP Fe irradiated with 150keV Fe^{+} ions at 300°C: (a) 10^{18} ionsm^{-2} (0.6dpa); (b) 2x10^{18} ionsm^{-2} (1.3dpa); (c) 10^{19} ionsm^{-2} (6.5dpa); (d) 1.6x10^{19} ionsm^{-2} (10.4dpa) [63].

400°C ~ 465°C

Z. Yao et al. [71] carried out further thin-foil irradiations at 400°C, 450°C and 465°C. At 400°C, the damage structures at lower doses were similar to what was observed at 300°C. As irradiation progressed, loops appeared to be very mobile and coalesced in a similar manner to form chains of loops with **b** = a/2<111>. Overall the damage structure was on a larger scale compared to lower irradiation temperatures. At the final dose of 2x10^{18} ions m^{-2}, both a/2<111> and a<100> interstitial loops were observed. The a<100> loops were much smaller in size, but were present in larger numbers (**Fig.6.2.2**). Most of the point defects were still contained in a/2<111> loops at this temperature.

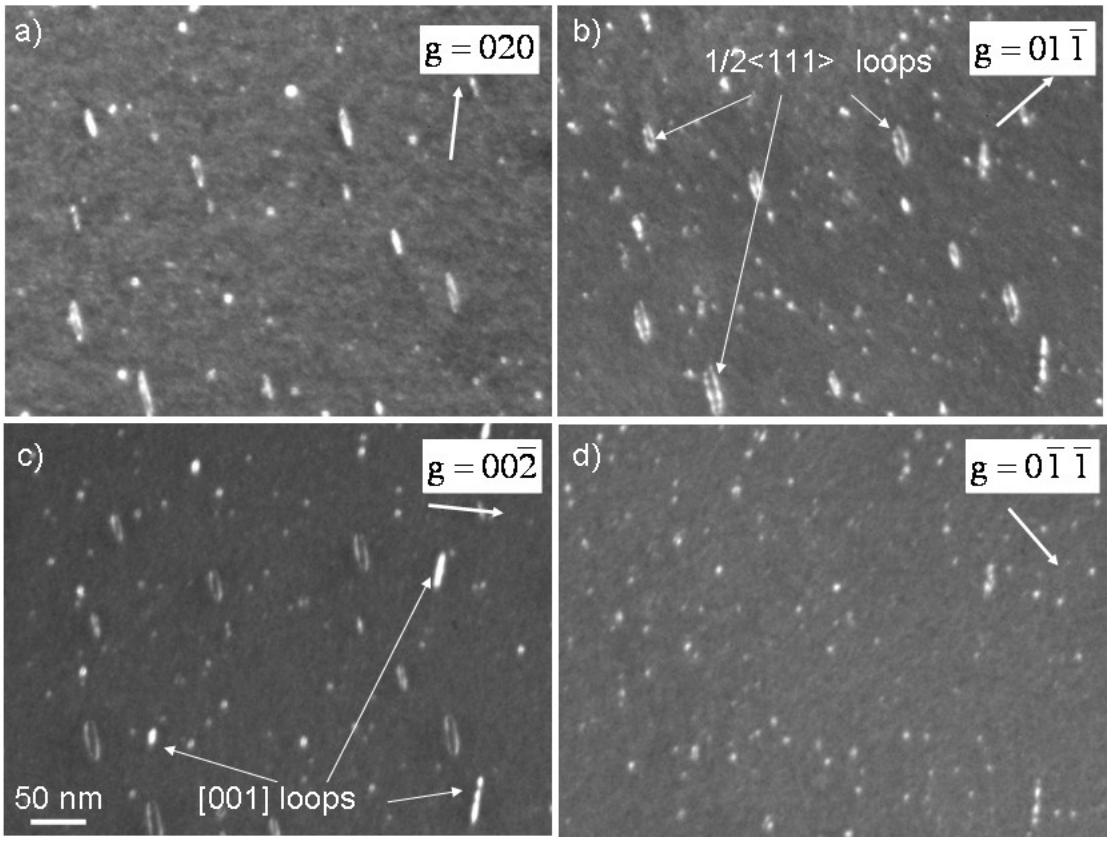

Fig.6.2.2 Contrast experiment of UHP Fe irradiated at 400°C to a dose of 2x10^{18}ions m^{-2} (~1.3 dpa) [71].

At 450°C, even though a/2<111> loops were still observed to form long chains; most areas of the specimen were dominated by a<100> loops of pure edge character and rectilinear shape (**Fig.6.2.3**). Most of the interstitials were contained in these a<100> loops. At irradiation temperatures above 450°C, mobile a/2<111> loops were seen to be subsumed by a<100> loops. Large a/2<111> were not formed at this temperature. Instead regular arrays of large a<100> loops were seen.

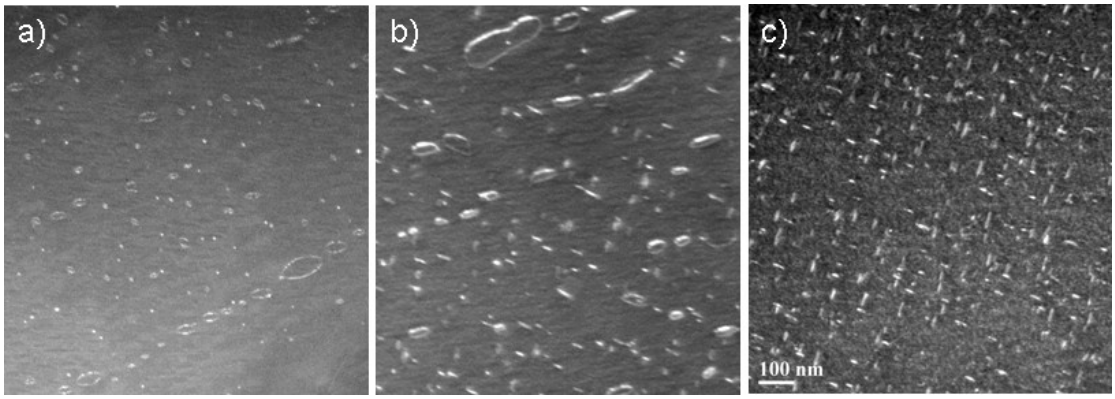

Fig.6.2.3. Loops in UHP Fe at 450°C at a dose of $3x10^{18}$ ions m^{-2}: (a) long lines of large *a*/2<111> loops in a grain oriented about 20° from [111]; (b) large loops of both types in an adjacent grain oriented close to [001], with a a<100> loops in a preponderance; (c) edge-on a<100> loops in the same grain [71].

500°C

In thin-foil experiments at 500°C, Jenkins et al. [70] found that the damage in UHP Fe consisted of **b** =a<100> prismatic edge loops, formed by nucleation and growth involving climb and coalescence. The damage microstructure followed the trend found between 400°C~465°C. At a dose of 10^{19} ions m^{-2} (6.5dpa) loops reached sizes of several hundred nanometres and formed regular arrays as shown in **Fig.6.2.4.** The nature of such large loops was determined to be interstitial using inside-outside techniques. Very similar damage evolution was observed in Fe-8Cr at 500°C, but on a finer scale.

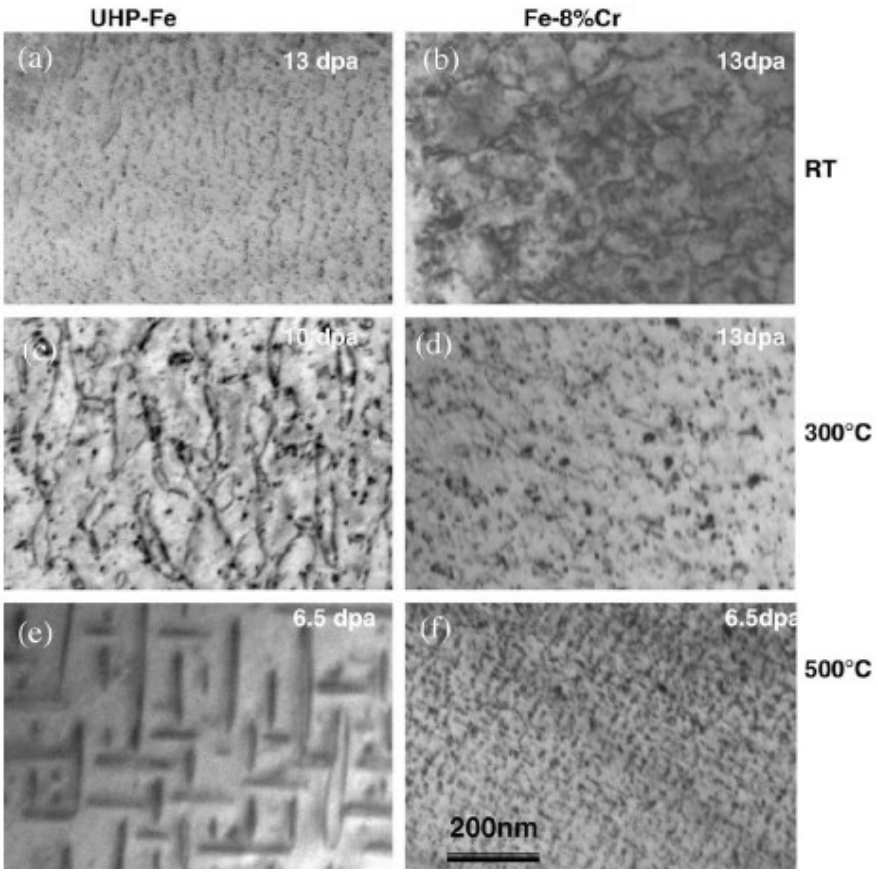

Fig.6.2.4 Comparison of high dose damage structures in UHP Fe and Fe-8Cr at different irradiation temperatures [70].

6.3. Damage evolution in bulk

The damage structures observed in bulk and thin-foil experiments share many similarities. The similarities in loop sizes and number densities at lower doses and temperatures suggest that the loops probably developed similarly at an early stage of the irradiation. In both cases loops seemed to develop earlier at higher temperatures. Both the thin-foil and bulk experiments in pure Fe show a consistent transition in loop Burgers vectors from 300^{o}C to 500^{o}C, with a/2<111> loops dominating at lower temperatures, and a<100> loops dominating at higher temperatures. Some of structures seen in thin-foil experiments are likely to be artefacts caused by surface effects in the thin-foil specimens. These include features such as large 'finger-shaped' loops (refer to **Fig.6.2.1**) which are not seen in the bulk. In Fe, the loop strings were only observed in thin-foil experiments. It is also important to note that the thin-foil experiments were carried out using UHP Fe (with the exception of RT experiments), and therefore loop mobilities are expected to be higher in these materials. We now compare damage evolution in pure Fe at different temperatures in more detail.

300^{o}C

In the bulk experiments in Fe at 300^{o}C, specimens showed very similar structures to the thin-foils at a dose level of about 2.5 dpa. Visible loops had an average size of 6.4 ± 1.3 nm, which is similar to the average size of 5.34 ± 0.09 nm found in the in-situ experiments at 1.3dpa. The Burgers vector analysis in the bulk showed that 92% of the resolvable loops had **b**

=a/2<111> and the 8% a<100> loops were generally smaller in size. This is also similar to what was found in the thin-foils. However, there was no evidence of any string structures or ‘finger-shaped’ loops in the bulk at this temperature. As described in the previous section, in the thin-foils small loops started to interact elastically to form string structures at a dose of about 0.6dpa.The absence of the loop string structures in the bulk could have a number of causes. First, the loop mobility is likely to be lower in the less pure specimens used in bulk experiments. In string formation loops move towards each other over long distances under the influence of long-range elastic forces, but this may be prevented if loops are pinned by impurities. Second, preferential loss of loops in thin-foils might be an important factor for string structures to form. Loops within strings locally all have the same Burgers vectors, probably as a result of the preferential loss of loops with other Burgers vectors. However in bulk experiment all variants of a/2<111> type loops were distributed randomly in the matrix. As noted above, the ‘finger-shaped’ loops observed at higher doses in the thin-foil experiments are likely to be an artefact due to surface effects. This is suggested by the fact that ‘fingers’ tended to point towards the hole of the specimen, suggesting that local stresses in the foil play an important role in the formation of such loops. The absence of ‘finger-shaped’ loops in the bulk is consistent with this picture.

400^{o}C

The bulk specimens also showed similar damage structures to the thin-foils at 400^{o}C. It was found in bulk specimens that the loop size increased from 21.8 ± 2.7 nm to 29.4 ± 2.6 nm as the dose increased from 2.5dpa to 7dpa. The

loop number densities at both dose levels were quite similar at 2.7 ± 0.8 and 2.2 ± 0.7 ($x10^{21}$ m^{-3}) respectively. These trends in the loop sizes and number densities were similar to those found in the thin-foil experiments, where size increased with both dose and temperature. The **g.b** analysis in bulk specimens showed that 75% of the loops had **b**= a/2<111>, and a<100> loops were smaller, which was also consistent with trends seen in thin-foil irradiations.

500ºC

The damage structures found in the bulk at this temperature also share some similarity to the thin-foil. At both 2.5dpa and 7dpa, large numbers of loops appeared to have edge a<100> character. The **g.b** analysis carried out on the 7dpa specimen found that over 90% of the loops had a<100> Burgers vectors. However, the loops did not form regular arrays as in the thin-foil. In addition, the sizes of the loops were much smaller in bulk than in thin-foil (about half the size at a dose of around 2.5dpa and one third the size at 7dpa), possibly as a result of the difference in specimen purities. At a higher dose of 7dpa, instead of forming regular array structures, some loops were seen to associate with each other to form more complex structures. This could also be due to impurities in the Fe specimens used in the bulk experiment [106]. It was also observed only in the bulk that networks of line dislocations with **b**=a/2<111> appeared throughout the specimen.

600°C

Bulk irradiation experiments were also carried out at 600°C. The features seen in the pure Fe specimen under this condition appeared to be very similar to the case of the bulk-irradiated specimens at 500°C (7dpa), where large complex loops and line dislocations were observed. There was an increase in loop size and a drop in loop number density compared to 500°C.

To summarise, despite the differences in microstructures, both thin-foil and bulk experiments in pure Fe showed a similar transition in Burgers vector from 300°C to 500°C: from domination of a/2<111> loops at 300°C to domination of a<100> loops at 500°C. The observation of a/2<111> dislocation networks and large 'loop shape' line dislocations at 500°C in the bulk specimens suggests that a possible explanation is that the a/2<111> loops have grown to larger size and have formed dislocation networks, leaving solely a<100> dislocation loops in the matrix. This is consistent with the observation that in bulk experiments, a/2<111> loops have larger mean sizes than a<100> loops at both 300°C and 400°C. However, line dislocations were not seen widely in specimens irradiated at 500°C to a lower dose (2.5dpa), although the absence of a **g.b** experiment at this condition makes it impossible to say whether a<100> loops dominate the microstructure. In thin foils, a/2<111> dislocation networks were not observed.

A second possible explanation for the transition in microstructures is suggested by recent theoretical calculations by Dudarev et al. [72, 73]. These

calculations showed that in α–Fe, due to spin fluctuations, an elastic instability is developed near the α–γ phase transition temperature (T_c = 912°C), resulting in a dramatic reduction of the shear stiffness constant C'. This reduction in C' has a strong effect on the anisotropic elastic self-energies of dislocations and relative stabilities of a<100> and a/2<111> prismatic edge loops. This theory predicts that a<100> loops will become relatively more stable in pure Fe with increasing temperature, which is consistent with the experimental observations in both thin-foils and bulk.

In the thin-foil in-situ work, the small visible a/2<111> loops were seen to be quickly subsumed by sessile a<100>loops and no large a/2<111> loops formed at temperatures higher than 465°C. However, it is not unlikely that mobile a/2<111> loops could develop very differently in thin-foils and bulk as the surface acts as efficient sinks for these defects.

The transition of damage structure from a/2<111> to a<100> loops is believed to have a profound effect on the radiation response of the material. For example, as discussed in chapter 1, Gelles [20] has suggested the presence predominantly of a<100> loops has the effect of suppressing void swelling in Fe-3Cr. Little et al. [9, 11] have argued that the evolution of the damage structure and the associated swelling resistance of ferritic alloys is due to the relative rates of nucleation and growth of the two interstitial loop types.

Nature determination of large loops was carried out in some bulk experiments, and as was also the case in thin foil experiments, all the large loops analysed

were found to be interstitial. Bulk specimens also contained small loops (~2nm) but the nature of these could not be established. As discussed above, there was some evidence in the thin-foils that small near-surface 1st layer loops had a vacancy nature [60]. However, in the in-situ work small a/2<111> loops were seen to coalesce into large interstitial loops at 300^{o}C and small mobile a/2<111> loops were seen to be subsumed into large interstitial a<100> loops at higher temperature (>450^{o}C) [71]. Both observations suggest that large numbers of small loops were of interstitial nature. Very small voids were observed only in Fe-8Cr in the in-situ experiments[63]. In the bulk experiments, voids were not found in any specimens. This suggests that in most cases, vacancies exist in the form of either small loops, or very small sub-microscopic voids under the resolution limit (~2nm) of TEM. In accordance to this, recent Positron Annihilation Spectroscopy (PAS) studies show evidence of vacancy clusters in Fe under both ion and proton irradiation [47, 49].

6.4. Effect of Cr on damage microstructures

6.4.1 Effect on Burgers Vectors

It is well known that the Cr content of ferritic steels strongly affects several aspects of their radiation response; however, the effects of Cr are not yet well understood on a mechanistic level. Kohyama et al. [7] found that both the DBTT and ΔDBTT were lowest for alloys containing about 9%Cr [7, 10, 11].

Gelles et al. [20] found that the void swelling was minimised for low chromium contents (i.e in the 3%Cr range), and the peak swelling of 0.7% was found in Fe-9%Cr.It was also observed that a reduction of chromium to the Fe-3Cr range resulted predominantly in a<100> dislocation structures, while increases above Fe-12Cr produced predominantly a/2<111> dislocation structures. Parollo et al. [74] also found that dislocation loops with **b** =a<100> were predominant in alloys with lower Cr content (Fe, Fe-2%Cr and Fe-6%Cr). In Fe-Cr alloys containing more than 6% Cr, both a<100> and a/2<111> loops were found.

The Burgers vectors found in this work show a dependence on both temperature and alloy composition (**Table.6.4.1**):

300°C	**400°C**	**500°C**	
Fe	92% ½<111>	75% ½<111>	95% <100>
Fe-8Cr	46% ½<111>		90% ½<111>
Fe-11Cr	37% ½<111>		31% ½<111>

Table.6.4.1 Summary of Burgers vector characterisation of bulk irradiated Fe and Fe-Cr alloys

At 300°C, our Burgers vector results are rather opposite to those reported by Gelles et al.: the higher Cr alloys (i.e. 11%Cr, 8%Cr) have more a<100> dislocation loops, whereas pure Fe produced predominantly a/2<111> loops. However, at an irradiation temperature of 500°C, it was found that a<100> loops predominated in pure Fe and a/2<111> loops predominated in Fe-8Cr.

This finding is very similar to that seen in recent neutron irradiation experiments [77]. It was unexpected however that the proportion of a/2<111> loops dropped to 31% when the Cr content was increased from 8% to 11%. It is still unclear why this is the case.

The results from both bulk and thin-foil self-ion irradiations show consistently that the Burgers vectors of loops in pure Fe have a clear temperature dependence. As described in the previous section, in pure Fe there is a transition of loop Burgers from predominantly a/2<111> type to a<100> type between 300^{o}C and 500^{o}C. In the case of Fe-Cr alloys however the situation is less clear. Alloys with 11% Cr show little temperature dependence from 300^{o}C to 500^{o}C, and alloys with 8% Cr show an increase in a/2<111> loops at high temperature. These results are rather inconsistent with the thin-foil work, where Fe-8%Cr specimens showed the same Burgers vector transition as pure Fe. The cause of this inconsistency is still unclear and more experiments are needed in order to understand it better.

6.4.2. Effect on Loop sizes

Matijasevic et al. (2007) [77] have studied Fe-Cr alloys and steels under neutron irradiation in the Belgian Reactor 2 (BR2) (295~300^{o}C). It was found at rather low dose levels (<1dpa), that both the average and maximum loop sizes decreased with increasing Cr concentration. Jenkins et al. have also found in thin-foil experiments, that the damage structure in Fe-Cr alloys is at a finer scale than in pure Fe.

In this work, the *average* image sizes of loops, under the same irradiation condition, was found to be similar in pure Fe and Fe-Cr alloys containing 8% and 11% Cr. However, there was a clear drop in the *maximum* loop sizes in Fe-Cr at higher doses (7dpa) at both 400°C and 500°C. This observation is consistent to what was found in the thin-foil experiments.

Average size (nm)

300°C 2.5dpa	**400°C 2.5dpa**	**400°C 7dpa**	**500°C 2.5dpa**	**500°C 7dpa**	**600°C 7dpa**	
Fe	6.4±1.4	21.8±2.7	29.4±2.6	25.4±2.3	35.4±1.8	37.8±2.5
Fe-8Cr	10.9±2.3			30.9±3.4	27.0±2.8	
Fe-11Cr	11.4±1.4	19.7±2.3	32.7±2.4	38.5±3.5		

Maximum size (nm)	**300°C 2.5dpa**	**400°C 2.5dpa**	**400°C 7dpa**	**500°C 2.5dpa**	**500°C 7dpa**	**600°C 7dpa**
Fe	35	45	105	65	105	105
Fe-8Cr	35			65	75	
Fe-11Cr	45	45	65	75		

Table.6.4.2 Summary of (a) average loop size and (b) maximum loop size of bulk irradiated Fe and Fe-Cr.

6.4.3 Effect on defect densities

The interstitial point defect densities (defined as the densities of interstitials contained in visible loops, and obtained by combining measurements of both loop sizes and number densities) which were reported in chapters 4 and 5, are re-plotted here as a function of the Cr concentration in **Fig.6.4.3**. Note a rather large systematic error is present due to the lack of accurate foil thickness measurements.

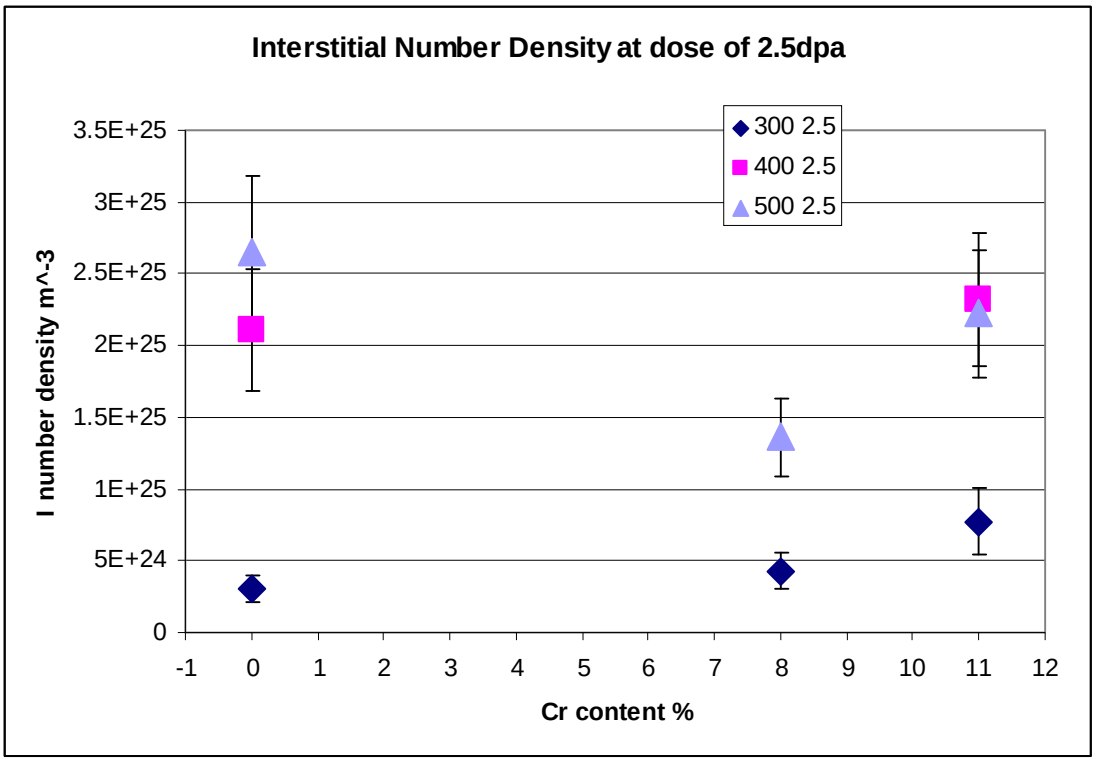

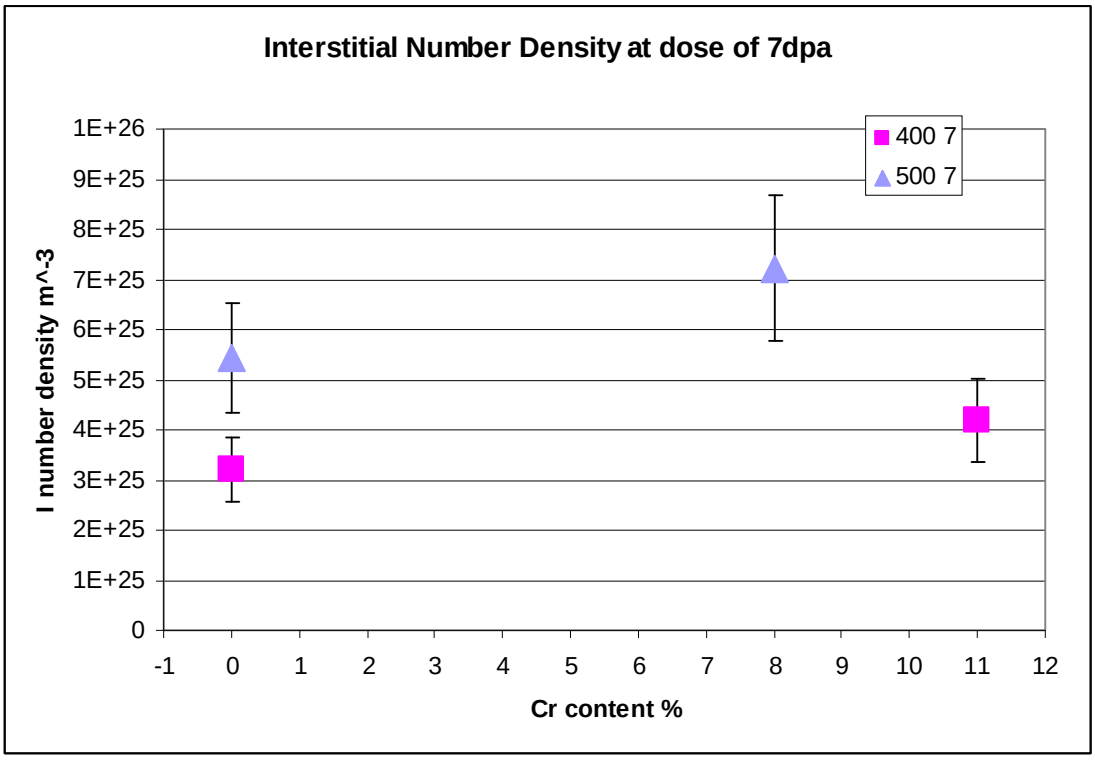

Fig.6.4.3 Interstitial densities as a function of Cr content.

The graphs show no obvious systematic change in interstitial densities with Cr content. This suggests that Cr has little effect on the recombination of point defects. This is in accordance with thin-foil work by Yao et al. [60], in which it was found that the numbers of loops produced in Fe-Cr alloys and pure Fe were similar at 300^{o}C. These authors observed that more loops were lost to surface during irradiation of pure Fe than in Fe-Cr alloys, resulting in a lesser number of retained loops in pure Fe at a given dose. However, when loop loss during irradiation was taken into account it was argued that the total number of loops produced was similar. Because the effect of loop loss is minimised in the bulk experiments, one would expect similar number of loops to be produced.

There is an increase in interstitial density from 300^{o}C to higher temperatures. Considering that loop sizes are much smaller at 300^{o}C, this increase is probably an artefact due to the experimental difficulty in estimating the number of interstitials contained in small loops.

Chapter 7: Conclusions and further work

The work carried out in this thesis was part of a large multi-scale modelling project, aimed at achieving a fundamental understanding of fast neutron radiation damage in ferritic materials and materials for fusion reactor in general. The objective of this thesis was to study the radiation damage produced in model materials of Fe and Fe-Cr alloys using diffraction contrast electron microscopy. The model alloys used are the basis of low-activation ferritic steels which are one of the most promising candidate materials for structural applications in future fusion reactors. Self-ion irradiations were used to simulate the primary knock-on damage produced by the fast-neutron irradiation. It was intended to combine the results of this thesis into parallel dislocation dynamics modelling project in the group. This was however not carried out due to the slow development of the modelling project. The results obtained from this work are summarised in the following sections.

This work was also intended to develop a specimen preparation route and characterisation methods for analysing heavy-ion radiation damage in bulk specimens. This was done successfully, and was described in chapter 2.4.2 [98]. These experimental techniques can now be applied in experiments carried out in new ion-irradiation facilities, in particular the Joint Accelerators for Nano-Science and Nuclear Simulation (JANNUS) facility in Saclay, France, which is just coming on line. This new facility allows ion irradiations to be performed under more controlled conditions, and with double or triple

beams including helium ions and protons, which better mimics the fusion reactor environment, see chapter 7.3.

7.1 Summary of Results

The irradiations were carried out in the Surrey Ion Beam centre. Specimens were irradiated with 2MeV and 0.5MeV Fe^{+} ions at temperatures from 300^{o}C to 600^{o}C. The maximum dose achieved was $3x10^{19}$ ions m^{-2} which is about 7dpa. The main feature seen in all specimens was a moderately high density of resolvable dislocation loops. The number densities, sizes and Burgers vectors of loops were characterised and results were compared between specimens under different irradiations conditions.

The characterisation of radiation damage in **pure Fe** specimens was described in chapter 4, and the results can be summarised as follows:

- The average image sizes of resolvable dislocation loops increased with both temperature and dose (refer to **Fig.4.2.5**, **Fig.5.1.1.3** and **Fig.5.2.1.3**). A dose increment from 2.5 to 7dpa had a strong effect on the maximum loop sizes, whereas a temperature increment had little effect.

- There was a small effect of dose on the number densities of loops. There was a clear drop in number densities from 300^{o}C to 400^{o}C. However there was no obvious change in number densities at higher temperatures.

- The Burgers vector analyses showed that the proportion of a/2<111> loops changed from 92% at 300ºC to 75% at 400ºC and 5% at 500ºC. More complex structures developed at higher dose (7dpa) at 500ºC. a<100> loops were seen to associate to each other to form nested loops and networks of large line dislocations with **b**= a/2<111> developed.

- No nature analyses were carried out on pure Fe specimens. However results from both bulk Fe-Cr alloys and thin-foil Fe show that large loops have interstitial nature, suggesting that large dislocation loops in bulk Fe specimens are also interstitial. No voids were found in any specimens

Characterisation of **Fe-8Cr and Fe-11Cr** was described in chapter 5 of this thesis. The results can be summarised as follows:

- In both Fe-8Cr and Fe-11Cr alloys, the average loop image sizes increased with both temperature and dose. The trend was very similar to that found in pure Fe experiments.

- A Burgers vector analysis in Fe-8Cr showed that the proportion of a/2<111> type loops increased from 46% at 300ºC to 90% at 500ºC.

- The proportion of a/2<111> loops in Fe-11Cr was found to be 37% at 300^{o}C and 31% at 500^{o}C.

- Nature analyses using inside-outside technique was carried out on a/2<111> loops in Fe-8Cr and a<100> loops in Fe-11Cr, and all loops analysed had interstitial nature. The nature of small loops could not be established. No voids were found in any specimens.

7.2. Conclusions

This work is the first to achieve a systematic characterisation of self-ion irradiation damage in bulk Fe and Fe-Cr at different temperatures and doses. The results of this thesis provide useful data on the formation and evolution of cascade damage in Fe and Fe-Cr. This is valuable in validating and feeding into theoretical multi-scale modelling programmes which are being used as a primary tool to study and predict the evolution of microstructure in fast neutron irradiations.

The following conclusions were reached:

- A systematic Burgers vector characterisation of dislocation loops in self-ion irradiated bulk Fe and Fe-Cr were carried out as a function of temperature and doses. In which both a/2<111> and a<100>

dislocation loops are present in all specimens, but their relative numbers differ from irradiation conditions and materials.

- The Burgers vector trend found in bulk pure Fe experiments is that a/2<111> loops dominated at 300^{o}C and a<100> loops dominated at 500^{o}C. This is consistent to what was found in parallel thin-foil experiments.
- The transition of damage structure from a/2<111> to a<100> loops is believed to have a profound effect on the radiation response of the material such as void swelling.
- Some plausible explanations of this Burgers vector transition are given in the discussion chapter. These include recent theoretical calculations on the relative stabilities of a/2<111> and a<100> loops as a function of temperature.
- The reason why a similar clear transition is not seen in Fe-Cr alloys is unclear.
- The results of bulk experiments show that some of the loop characters found in high dose thin-foil experiments (such as the ‘finger-shaped’ loops) are likely artefacts due to surface effects.
- Cr has little effect on recombination and point defect survival.
- Large dislocation loops (typically >10nm) are determined to be interstitials using inside-outside method. It is believed that vacancies exist either as small loops or sub-microscopic voids in all specimens (which are impossible to characterise using TEM).

7.3. Further work

A moderately complete characterisation of the radiation damage in bulk pure Fe specimen has been established in this thesis. The results in pure Fe are generally in good agreement with parallel thin-foil in-situ experiments and are also in accordance to some recent theoretical work. It would be very useful to feed these results into future dislocation dynamics models to study the effect of cascade damage on radiation induced embrittlements in ferritic materials.

In Fe-Cr, some conclusions were established but the experiments are less complete and there are some inconsistencies between the bulk and thin-foil work, and with the literature. Efforts were made to look at multiple specimens of the same type, to ensure that the results were not experimental artefact. However, more complete experiments in Fe-Cr alloys are needed to establish a better trend in the radiation damage dependences on temperature and Cr content.

The work from this thesis has pioneered the specimen preparation and characterisation techniques for studying bulk heavy-ion irradiation damage. The Surrey Ion Beam Facility has several limitations for this type of work, which it was not possible to overcome because at the time no better irradiation facility was available. First, the dose rate is not constant and cannot be controlled accurately. Second, it is possible only to carry out single beam implantation, with mono-energetic ions. This introduces several limitations: 1) in order to achieve a more uniform damage profile, one has to carry out multiple-energy irradiations sequentially and this could potentially alter the

damage structure; 2) no simultaneous He, H and self-ion irradiation could be carried out to simulate the production of transmutation gases by highly-energetic neutrons. The JANNUS facility in France has been designed especially for irradiation damage studies, and addresses these limitations. JANNUS was approved for construction and completed during the course of this work. It employs an energy degrader to flatten the damage profile. It is also capable of simultaneous dual-beam and triple-beam irradiations (although to date no triple-beam irradiations have been performed). One of the intentions of this work was to develop the experimental methodology for the experiments of JANNUS, and this has proven successful. More advanced work is now being carried out with JANNUS to look at the effect of He and H on radiation damage and preliminary results on dual-beam irradiations have been reported very recently [107].

This research can also be extended to look at damage development in more complex and realistic materials such as Ferritic/Martensitic steels (e.g. Eurofer 97). Analytical microscopy, especially chemical mapping by EELS, will become increasingly useful in characterising these specimens. It would be very useful to build correlations with other techniques such as Positron Annihilation Spectroscopy (PAS) and atom probe tomography.